IntechOpen

Magnetic Bearings
Theory and Applications

Edited by Bostjan Polajzer

Magnetic Bearings, Theory and Applications

edited by
Boštjan Polajžer

Magnetic Bearings, Theory and Applications
http://dx.doi.org/10.5772/245
Edited by Bostjan Polajzer

Notice

Statements and opinions expressed in the chapters are these of the individual contributors and not necessarily those of the editors or publisher. No responsibility is accepted for the accuracy of information contained in the published chapters. The publisher assumes no responsibility for any damage or injury to persons or property arising out of the use of any materials, instructions, methods or ideas contained in the book.

First published in Croatia, 2010 by INTECH d.o.o.
eBook (PDF) Published by IN TECH d.o.o.
Place and year of publication of eBook (PDF): Rijeka, 2019.
IntechOpen is the global imprint of IN TECH d.o.o.
Printed in Croatia

Legal deposit, Croatia: National and University Library in Zagreb

Additional hard and PDF copies can be obtained from orders@intechopen.com

Magnetic Bearings, Theory and Applications
Edited by Bostjan Polajzer

p. cm.

ISBN 978-953-307-148-0

eBook (PDF) ISBN 978-953-51-5925-4

Contents

Preface

The term magnetic bearing refers to devices that provide stable suspension of a rotor. Because of the contact-less motion of the rotor, magnetic bearings offer many advantages for various applications. Commercial applications include compressors, centrifuges, high-speed turbines, energy-storage flywheels, high-precision machine tools, etc.

Magnetic bearings are a typical mechatronic product. Thus, a great deal of knowledge is necessary for its design, construction and operation. This book is a collection of writings on magnetic bearings, presented in fragments and divided into six chapters.

First two chapters discuss the so called "classical" magnetic bearing systems, which are composed of two radial active magnetic bearings, one axial bearing, and an independent driving motor. In Chapter 1, different control design approaches are applied to an experimental magnetic bearing system MBC500. The proposed interpolation design approach and fuzzy logic design are compared with the classical control design. Chapter 2 deals with non-linearities of magnetic bearing radial force characteristic. The optimisation of the bearing geometry is proposed, where the aim is to find such design, where a radial force characteristic is linear, as much as possible, over the entire operating range.

The following chapters present special magnetic suspension systems. Chapter 3 discusses magnetic suspension for vibration insulation systems, where a novel zero-power control is proposed. Self-bearing motors are discussed in Chapter 4. A structure of axial-gap self-bearing motor is studied, whereas a vector control is discussed in details. Chapter 5 presents different structures of passive permanent magnet bearings. Analytical formulations are given for each case of axial, radial or perpendicular polarisation of permanent magnets. In Chapter 6, an experimental rotor model is presented with two gradient static field shafts and a high-temperature superconducting bulk.

Hopefully, this book will provide not only an introduction but also a number of key aspects of magnetic bearings theory and applications. Last but not least, the presented content is free, which is of great importance, especially for young researchers and engineers in the field.

Editor

Boštjan Polajžer
University of Maribor, Faculty of Electrical Engineering and Computer Science
Slovenia

1

Design and implementation of conventional and advanced controllers for magnetic bearing system stabilization

Juan Shi and Wee Sit Lee
School of Engineering and Science, Victoria University
Australia

1. Introduction

Active magnetic bearings (AMBs) employ electromagnets to support machine components. The magnetic forces are generated by feedback controllers to suspend the machine components within the magnetic field and to control the system dynamics during machine operation. AMBs have many advantages over mechanical and hydrostatic bearings. These include zero frictional wear and efficient operation at extremely high speed. They are also ideal for clean environments because no lubrication is required. Hence, as a result of minimal mechanical wears and losses, system maintenance costs of AMBs are low. AMBs are used in a number of applications such as energy storage flywheels, high-speed turbines and compressors, pumps and jet engines (Williams et al., 1990), (Lee et al., 2006). AMBs are inherently unstable and it is necessary to use feedback control system for stabilization (Williams et al., 1990), (Bleuler et al., 1994). This can be achieved by sensing the position of the rotor and using feedback controllers to control the currents of the electromagnets.

This chapter will present our experience in different design approaches of stabilizing magnetic bearing systems. By using these approaches, feedback controllers will be designed and implemented for an experimental magnetic bearing system - the MBC500 magnetic bearing system (Magnetic Moments, 1995).

As most of the design methods to be presented are model based, a plant model is required. Since the magnetic bearing system is open-loop unstable, a closed-loop system identification procedure is required to identify its model. For this purpose, we adopted a two step closed-loop system identification procedure in the frequency domain. After various model structures were attempted, an 8^{th}-order model of the MBC500 magnetic bearing system was identified by applying the System ID toolbox of MatLab to the collected frequency response data. In the following, this 8^{th}-order unstable model will be treated as the full-order model of the open-loop plant.

In the first approach, a model based conventional controller is designed on the basis of a reduced 2^{nd}-order unstable model of the MBC500 magnetic bearing system. In this

approach, notch filters are necessary to cancel the resonant modes of the active magnetic bearing system (Shi & Revell, 2002).

In the second approach, a model based controller is designed via interpolation of units on the complex s-plane. This is an analytical design method. Among various approaches for feedback control design, analytical design methods offer advantages over trial and error design techniques. These include the *conditions for the existence of a solution* and *the algorithms that are guaranteed to find the solutions, when these exist (*Dorato, 1999). A limitation of the analytical methods is, however, that they tend to generate more complex controllers. One of the analytical feedback controller design methods is the *interpolation approach* we employed, where units in the algebra of bounded-input bounded-output (BIBO) stable proper rational functions are used to interpolate specified values at some given points in the complex s-domain (Dorato, 1999), (Dorato,1989). When applying this approach to stabilize the MBC500 magnetic bearing system, the controller is designed on the basis of the reduced 2nd-order unstable model. Since there are resonant modes that can threaten the stability of the closed loop system, notch filters are employed to help secure stability (Shi and Lee, 2009).

The third approach in this chapter involves the design of a Fuzzy Logic Controller (FLC). The FLC uses error and rate of change of error in the position of the rotor as inputs and produces output voltages to control the currents of the amplifiers that driving the magnetic bearing system. This approach does not require any analytical model of the MBC500 magnetic bearing system. This can greatly simplify the controller design process. Furthermore, it will be demonstrated that the FLC can stabilize the magnetic bearing system without the use of any notch filter (Shi et al., 2008) (Shi & Lee, 2009). Instead of applying the output of a FLC directly to the input of a magnetic bearing system (like what we have done here), the output of a FLC can also be used to tune the gains of controllers. For example, Habib and Inayat-Hussain (2003) reported a dual active magnetic bearing system in which the output of a FLC was used to tune the gains of a linear PD controller.

The performance of each of the controllers described above will be tested first via simulation. They will be compared critically in terms closed-loop step responses (steady-state error, peak overshoot, and settling time), disturbance rejection, and the size of control signal. The controllers designed will then be coded in C and implemented in real time on a Digital Signal Processor (DSP) card. The implementation results will also be compared with the simulation results.

2. Description of the MBC500 Magnetic Bearing System

The MBC500 magnetic bearing system consists of two active radial magnetic bearings which support a rotor. It is mounted on top of an anodized aluminium case as shown in Figure 1 (Magnetic Moments, 1995). The rotor shaft is actively positioned in the radial directions at the shaft ends (four degrees of freedom). It is passively centred in the axial direction and can freely rotate about its axial axis. The system employs four linear current-amplifier pairs (one pair for each radial bearing axis) and four internal analogue lead compensators to independently control the radial bearing axes. In this chapter, we shall present design examples where all the four on-board analogue controllers will be replaced by digital controllers designed through different approaches.

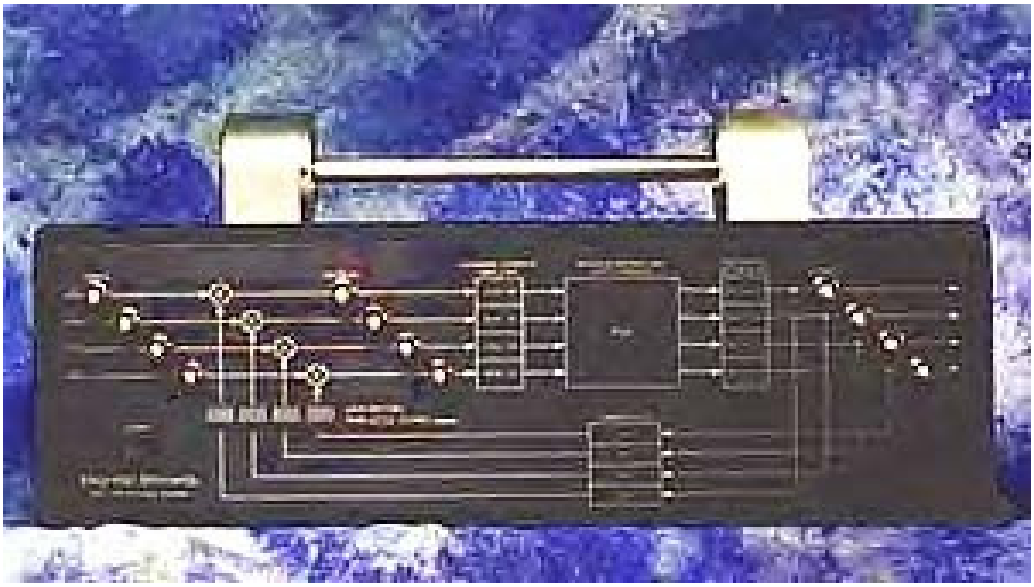

Fig. 1. MBC500 magnetic bearing research experiment (Source: Magnetic Moments, 1995)

A diagram which defines the system coordinates is shown in Figure 2. The system has four degrees of freedom, with two degrees of freedom at each end. These degrees of freedom are all translational in nature and are perpendicular to the z-axis. They are in the horizontal direction (x_1 and x_2) and in the vertical direction (y_1 and y_2) (Magnetic Moments, 1995).

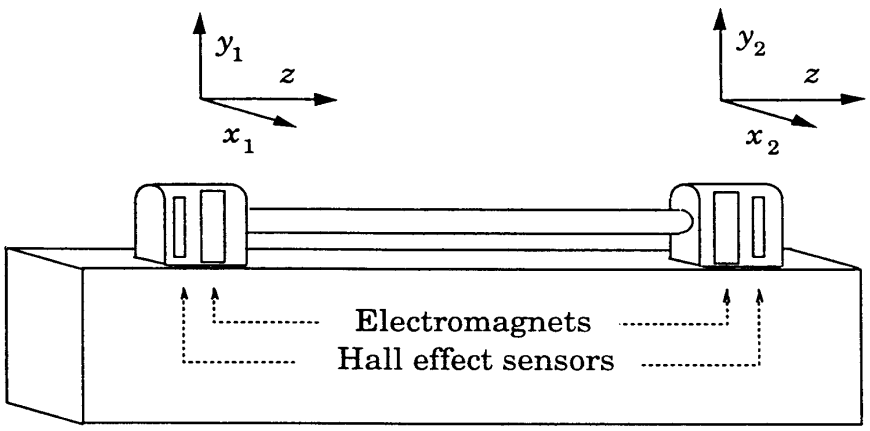

Fig. 2. MBC500 system configurations (Morse, 1996)

3. System Identification

3.1 System Identification and reduced order model

Since the magnetic bearing system is open-loop unstable, a closed-loop system identification procedure was required to identify its model. For this purpose, we adopted a two-step closed-loop system identification procedure (Morse 1996), (Van den Hof & Schrama 1993). The procedure employs frequency response data. The details of the frequency response experiment and the system identification procedure were described in (Shi & Revell, 2002).

Various model structures were attempted before an 8th-order final model was found. The transfer function of the 8th-order model is shown as follows:

$$P(s) = \frac{-104.21(s-2854)(s^2+9785s+3.274\times10^7)(s^2-379.15s+2.048\times10^7)(s^2-564.5s+1.645\times10^8)}{(s+511)(s-292.7)(s^2+32.97s+2.344\times10^7)(s^2+6197s+4.02\times10^7)(s^2+23.77s+1.66\times10^8)} \quad (1)$$

Note that the pole at s=292.7 of the above transfer function indicates the instability of the open-loop MBC500 magnetic bearing system. Furthermore, it should be noted that when the model is employed for model-based controller design, closed-loop performance limitations will also be imposed by the right-half plane zero at s=2854 (Freudenberg & Looze, 1985).
It can be seen from equation (1) that the MBC500 magnetic bearing model includes two resonant modes. They are located at approximately 780 Hz and 2055 Hz. Each of these two modes causes an increase in magnitude and a large change in phase in the frequency response. These characteristics of the resonant modes can threaten the stability of the closed-loop system. Consequently, two notch filters are designed to eliminate these unwanted resonances. Since the notch filters must cancel out the resonant modes, the resonant frequencies of the experimental model must be obtained accurately. Two elliptic notch filters have been designed to notch out the resonant modes. As a result, controllers can be designed on the basis of a reduced order unstable system model where the resonant modes are absent. This reduced order model of the plant can be obtained by eliminating the resonant modes and preserving the DC gain of the 8th-order magnetic bearing system model. The resulting reduced order model has a transfer function of

$$P(s) = \frac{-75.86(s-2854)}{(s+511)(s-292.7)} \quad (2)$$

4. Conventional Controller Design

A single-loop unity-feedback control system shown in Figure 3 is considered in the controller design in this chapter. In this Figure, P(s) is the transfer function of the magnetic bearing system and C(s) is the transfer function of the controller.

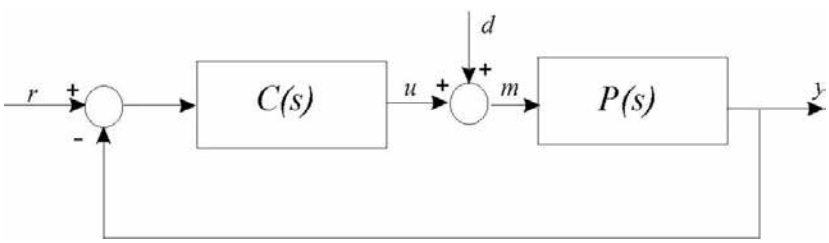

Fig. 3. A single-loop unity-feedback control system

On the basis of the reduced order model described by equation (2), a conventional lead compensator was designed by using root locus method (Shi & Revell, 2002). Although the lead compensator has been designed to stabilize the MBC500 magnetic bearing system, its frequency response has a magnitude which remains large in the high frequency region. This will affect the stability robustness of the closed-loop system. Thus an additional high frequency pole at 7000 Hz (or 43982 rad/s) was incorporated to reduce the gain at high frequency. As a result, the final controller employed in (Shi & Revell, 2002) was a second order controller (lead with low pass filter with cut off frequency of 7000 Hz) and the transfer function of the controller is as follows:

$$C_{lead}(s) = \frac{4.23(s+1067.3)}{(s+3202)}\frac{43982}{(s+43982)} \tag{3}$$

Figure 4 illustrates the root locus of the magnetic bearing system represented by the reduced order model shown in equation (2) with the designed lead compensator shown in equation (3). The closed-loop poles are at -4.43×10^4, -2.73×10^3, and $-167\pm392j$ respectively. Figure 5 shows the Bode plot of the closed-loop system with and without the added low pass filter. It can be seen from the Bode plot that the added low pass filter improves the system robustness by reducing system sensitivity to uncertain high frequency dynamics.

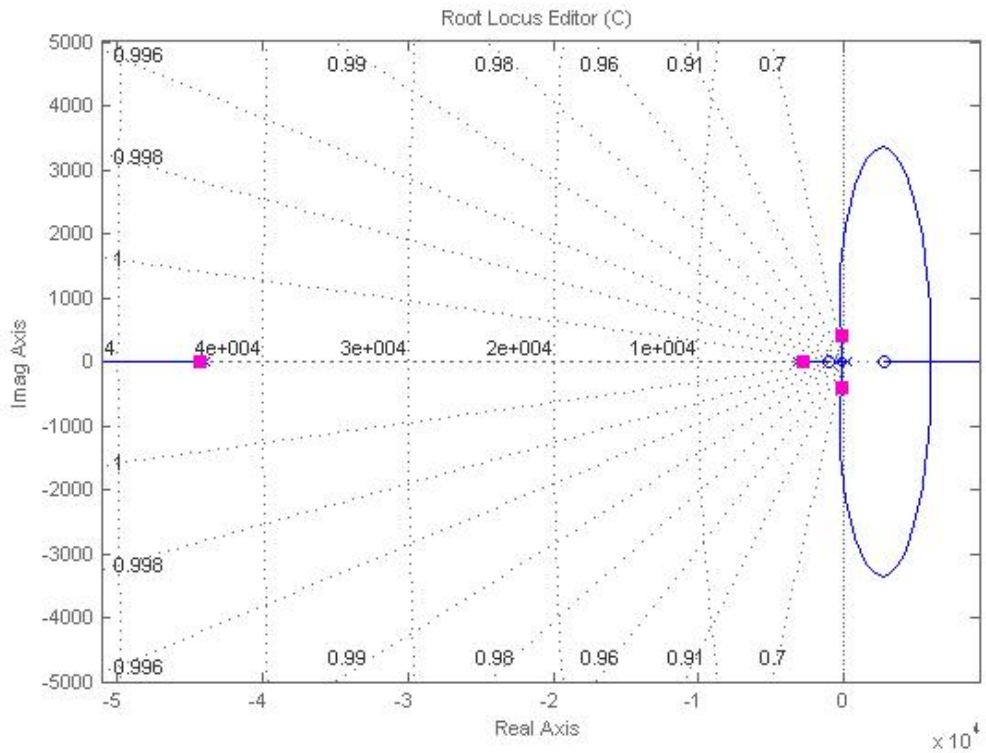

Fig. 4. Root locus of the magnetic bearing system (a reduced 2nd-order model is used here) with the designed lead compensator

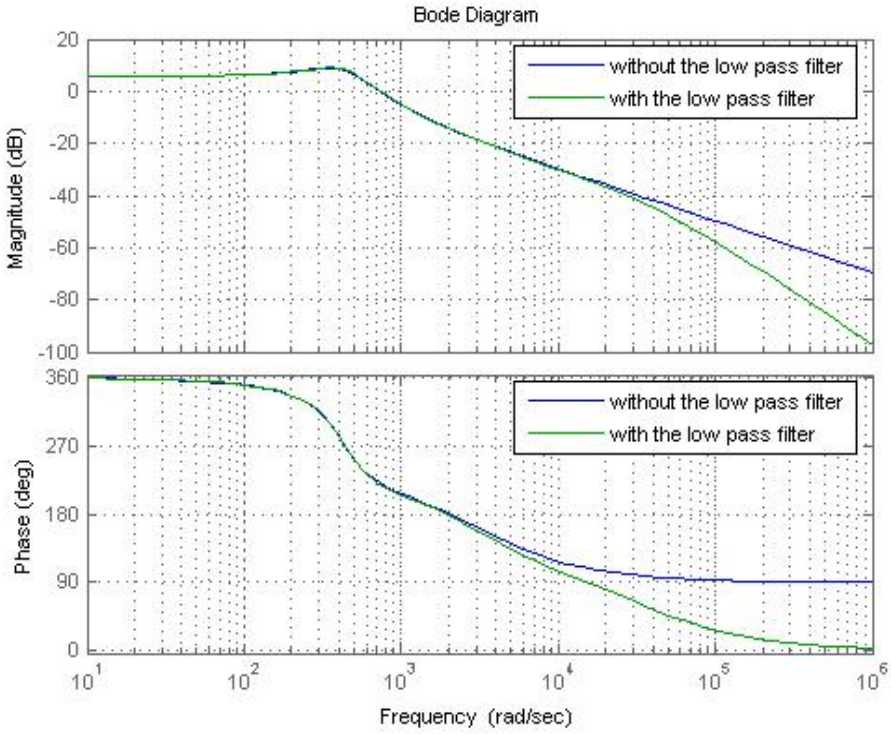

Fig. 5. Bode plot of the magnetic bearing system (a reduced 2nd-order model is used here) with the designed lead compensator

5. Controller Design via Interpolation Approach

5.1 Controller Design via Interpolation Approach

A single-loop unity-feedback control system shown in Figure 3 is considered in the controller design via the interpolation approach described in (Dorato, 1999). It was shown in (Dorato, 1999) that any rational transfer function,

$$P(s) = \frac{n_p(s)}{d_p(s)} \tag{4}$$

where $n_p(s)$ and $d_p(s)$ are arbitrary polynomials, can always be written as a ratio of two coprime *stable* proper transfer functions,

$$P(s) = \frac{N_p(s)}{D_p(s)} \tag{5}$$

where

$$N_p(s) = \frac{n_p(s)}{h(s)} \tag{6}$$

and

$$D_p(s) = \frac{d_p(s)}{h(s)} \tag{7}$$

with $h(s)$ a Hurwitz polynomial of appropriate degree. Let $U(s)$ be a *unit* in the algebra of BIBO stable proper transfer functions, then following (Dorato, 1999) a stable stabilizing controller can be calculated as:

$$C(s) = \frac{U(s) - D_p(s)}{N_p(s)} \tag{8}$$

when P(s) satisfies the parity-interlacing property (p.i.p.) condition (Youla, 1974) and U(s) satisfies certain interpolation conditions. Specifically, let b_i denotes the zeros of the plant in the RHP, the closed-loop system will be internally stable, and the controller will be stable, if and only if $U(s)$ interpolates to $U(b_i) = D_p(b_i)$ (Dorato, 1999).

5.2 Controller Design for the Magnetic Bearing System

Firstly we note that the reduced order model of the plant described by equation (2) has a zero at s =2854 and a zero at s =∞. Since the pole at s = 292.7 is not between these two zeros, the *parity-interlacing property* (p.i.p.) condition (Youla, 1974) is satisfied and a stable stabilizing controller is known to exist.

In the following, we assume that the design must satisfy the following specifications:

- The sensitivity function is to have all its poles at s =-511,
- A steady-state error magnitude (subjected to a unit step input) of e_{ss} = 0.1.

Since the closed-loop transfer functions are:

$$\frac{E(s)}{R(s)} = \frac{1}{1 + C(s)P(s)} = \frac{D_p(s)}{U(s)} \tag{9}$$

$$\frac{Y(s)}{D(s)} = \frac{P(s)}{1 + C(s)P(s)} = \frac{N_p(s)}{U(s)} \tag{10}$$

$$\frac{M(s)}{R(s)} = \frac{C(s)}{1 + C(s)P(s)} = \frac{D_p(s)C(s)}{U(s)} \tag{11}$$

By choosing $h(s) = (s + 511)^2$, the requirement of the closed-loop poles specification will be satisfied. As a result,

$$N_p(s) = \frac{-75.86(s - 2854)}{(s + 511)^2} \tag{12}$$

and

$$D_p(s) = \frac{(s - 292.7)}{(s + 511)^2} \tag{13}$$

The interpolation conditions are:

$U(2854) = D_p(2854) = 0.7612$, and $U(\infty) = D_p(\infty) = 1$.

Let the steady-state error magnitude be $e_{ss} = 0.1$, then:

$$e_{ss} = \left|\frac{D_p(0)}{U(0)}\right| \tag{14}$$

Let the interpolating unit $U(s)$ take of the following form:

$$U(s) = \frac{h(s)}{s^2 + as + b} \tag{15}$$

with $a > 0$ and $b > 0$, then after some simple calculations, the controller is found to be:

$$C(s) = \frac{6.8046(s + 511)(s + 99.59)}{(s + 2322)(s + 19.73)} \tag{16}$$

Controllers with other values of steady-state error magnitude can also be found by following similar procedures. For example, the following controllers $C_1(s)$ and $C_2(s)$ were computed on the basis of error magnitude $e_{ss} = 0.01$ and $e_{ss} = 1$, respectively.

$$C_1(s) = \frac{6.9978(s + 511)(s + 88.92)}{(s + 2355)(s + 1.946)} \tag{17}$$

$$C_2(s) = \frac{4.914(s + 511)(s + 250.7)}{(s + 1967)(s + 231.8)} \tag{18}$$

It can be seen that each of these controllers is of second order and is in the form of a lead-lag compensator.

6. Fuzzy logic controller design

A fuzzy logic controller (FLC) consists of four elements. These are a fuzzification interface, a rule base, an inference mechanism, and a defuzzification interface (Passino & Yurkovich, 1998). A FLC has to be designed for each of the four channels of the MBC500 magnetic system. The design of the FLC for channel x_2 is described in detail in this section. The design of the remaining FLCs will follow the same procedure. The FLC designed for the MBC500 magnetic bearing system in this section has two inputs and one output. The "Error" and "Rate of Change of Error" variables derived from the output from the MBC500 on-board hall-effect sensor will be used as the inputs. A voltage for controlling the current amplifiers on the MBC500 magnetic bearing system will be produced as the output. The shaft's schematic (top view) showing the electromagnets and the Hall-effect sensors is provided in Figure 6.

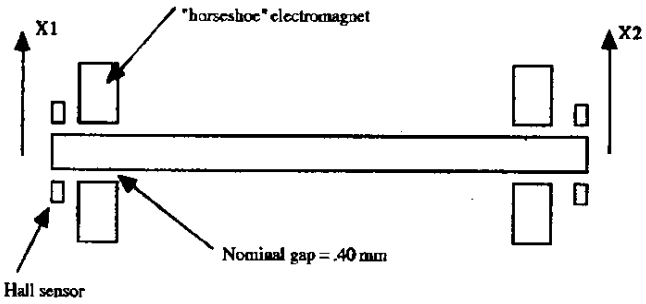

Fig. 6. Shaft schematic showing electromagnets and Hall-effect sensors (Magnetic Moments, 1995)

Figure 7 shows the single channel block diagram of the magnetic bearing system with the proposed FLC. A PD-Like FLC was designed to improve system damping as closed-loop stability is the major concern of the magnetic bearing system. As the MBC500 is a small magnetic bearing system, it has extremely fast dynamic responses which include the vibrations at *770 Hz* and *2050 Hz*. Therefore, a sampling frequency of *20kHz* (or a sample period of 50 microseconds) was deemed necessary.

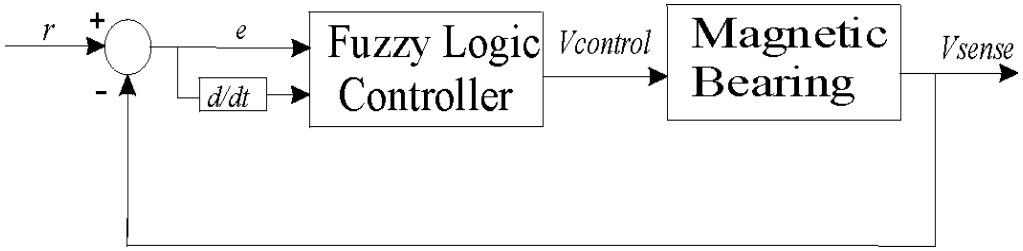

Fig. 7. FLC for MBC500 magnetic bearing system

Figure 8 illustrates the horizontal orientation (top view) of the MBC500 magnetic bearing shaft with the corresponding centre reference line, and its output and input at the right hand side (that is, channel 2).

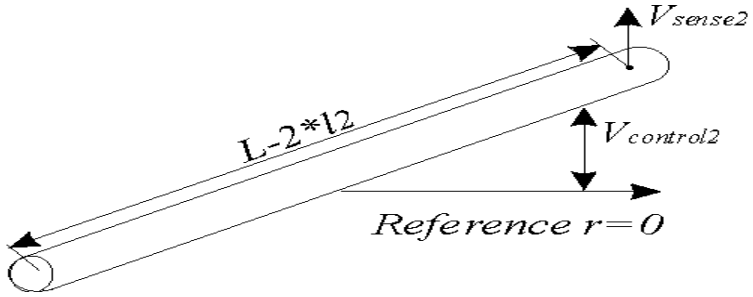

Fig. 8. MBC500 magnetic bearing control at the right hand side for channel x_2

The displacement output x_2 is sensed by the Hall-effect sensor as the voltage V_{sense2}. Hence the error signal is defined for channel x_2 as:

$$e(t) = r(t) - V_{sense2}(t)$$

For the magnetic bearing stabilization problem, the reference input is *r(t) = 0*. As a result,

$$e(t) = -V_{sense2}(t)$$

and

$$\frac{d}{dt}e(t) = -\frac{d}{dt}V_{sense2}(t)$$

The linguistic variables which describe the FLC inputs and outputs are:

"Error" denotes *e(t)*
"Rate of change of error" denotes $\frac{d}{dt}e(t)$
"Control voltage" denotes $V_{control2}$

The above linguistic variables "error", "rate of change of error," and "control voltage" will take on the following linguistic values:

"NB" = Negative Big
"NS" = Negative Small
"ZO" = Zero
"PS" = Positive Small
"PB" = Positive Big

Drawing on the design concept of the FLC for an inverted pendulum on a cart described in (Passino & Yurkovich, 1998) the following statements can be developed to illustrate the linguistic quantification of the different conditions of the magnetic bearing:

- The statement "error is PB" represents the situation where the magnetic bearing shaft is significantly below the reference line.
- The statement "error is NS" represents the situation where the magnetic bearing shaft is just slightly above the reference line. However, it is neither too close to the centre reference position to be quantified as "ZO" nor it is too far away to be quantified as "NB".
- The statement "error is ZO" represents the situation where the magnetic bearing shaft is sufficiently close to the centre reference position. As a linguistic quantification is not precise, any value of the error around e(t) = 0 will be accepted as "ZO" as long as this can be considered as a better quantification than "PS" or "NS".
- The statement "error is PB and rate of change of error is PS" represents the situation where the magnetic bearing shaft is significantly below the centre reference line and, since $\frac{d}{dt}V_{sense2} < 0$, the magnetic bearing shaft is moving slowly away from the centre position.

- The statement "error is NS and rate of change of error is PS" represents the situation where the magnetic bearing shaft is slightly above the centre reference line and, since $\frac{d}{dt}V_{sense2} < 0$, the magnetic bearing shaft is moving slowly towards the centre position.

We shall use the above linguistic quantification to specify a set of rules or a rule-base. The following three situations will demonstrate how the rule-base is developed.

1. If error is NB and rate of change of error is NB Then force is NB.

Figure 9 shows that the magnetic bearing shaft at the right end is significantly above the centre reference line and is moving away from it quickly. Therefore, it is clear that a strong negative force should be applied so that the shaft will move to the centre reference position.

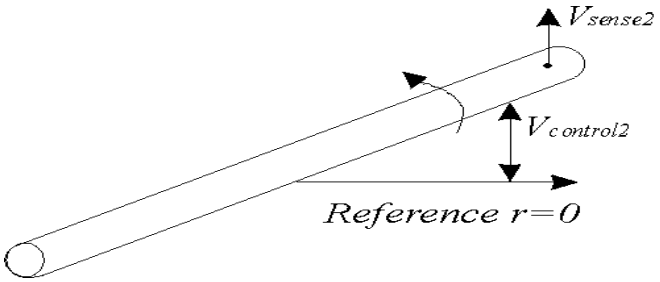

Fig. 9. Magnetic bearing shaft at the right end with a positive displacement

2. If error is ZO and rate of change of error is PS Then force is PS.

Figure 10 shows that the bearing shaft at the right end has a displacement of nearly zero from the centre reference position (a linguistic quantification of zero does not imply that e(t)=0 exactly) and is moving away (downwards) from the centre reference line. Therefore, a small positive force should be applied to counteract the movement so that it will move towards the centre reference position.

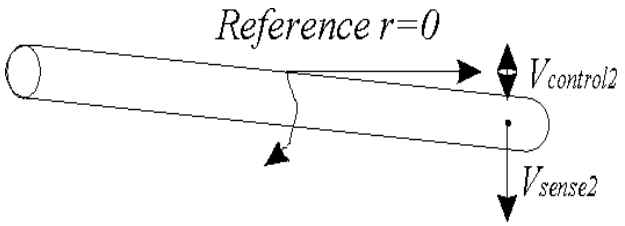

Fig. 10. Magnetic bearing shaft at the right end with zero displacement

3. If error is PB and rate of change of error is NS Then force is PS.

Figure 11 shows that the bearing shaft at the right end is far below the centre reference line and is moving towards the centre reference position. Therefore, a small positive force should be applied to assist the movement. However, it should not be too large a force since the bearing shaft at the right end is already moving in the correct direction.

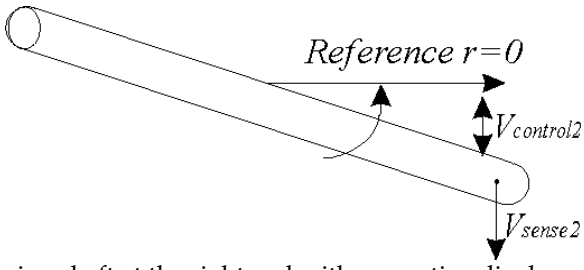

Fig. 11. Magnetic bearing shaft at the right end with a negative displacement

Following a similar analysis, the rules of the FLC for controlling the magnetic bearing shaft can be developed. For the FLC with two inputs and five linguistic values for each input, there are 5^2=25 possible rules with all combination for the inputs. A set of possible linguistic output values are NB, NS, ZO, PS and PB. The tabular representation of the FLC rule base (with 25 rules) of the magnetic bearing fuzzy control system is shown in Table 1.

"control voltage" V		"rate of change of error" $\dot{e}$				
		NB	NS	ZO	PS	PB
"error" e	NB	NB	NB	NB	NS	ZO
	NS	NB	NB	NS	ZO	PS
	ZO	NB	NS	ZO	PS	PM
	PS	NS	ZO	PS	PB	PB
	PB	ZO	PS	PB	PB	PB

Table 1. Rule table with 25 rules

The membership functions to be employed are of the triangular type where, for any given input, there are only two membership functions premises to be calculated. This is in contrast to Gaussian membership functions where each requires more than two premise outputs and can generate a large amount of calculations per final output. The triangular membership functions used is shown in Figure 12:

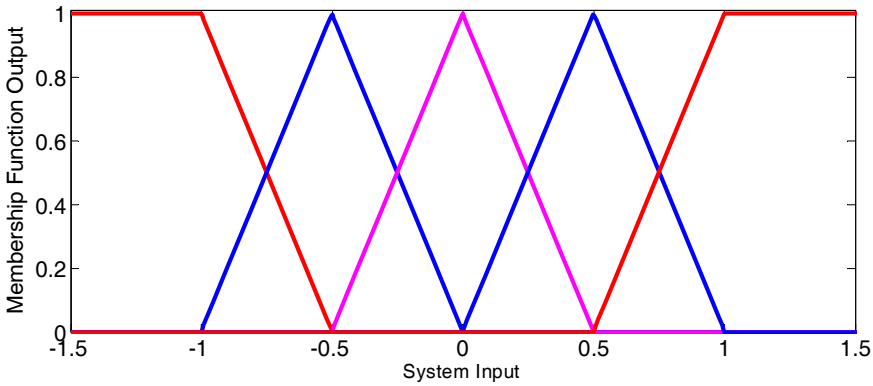

Fig. 12. Triangular Membership Function

The membership functions shown in Figure 12 represent the linguistic values NB, NS, ZO, PS, PB (from left to right).

The inference method used for the designed FLC is Takagi-Sugeno Method (Passino & Yurkovich, 1998) and the centre average method is used in the defuzzification process (Passino & Yurkovich, 1998).

7. Simulation Results

By using the designed conventional controller $C_{lead}(s)$, the controllers $C(s)$, $C_1(s)$, *and* $C_2(s)$ designed via the analytical interpolation method, and the FLC designed in Section 6, the closed-loop responses to a unit-step reference (applied at $t = 0$) and a unit-step disturbance (applied at $t = 0.05$ seconds) and the corresponding control signals are shown in Figure 13 and Figure 14, respectively. In all of the simulations, the full 8th-order plant model described by equation (1) was employed.

It is important to note that the DC gain designed into each of $C(s)$ and $C_1(s)$ via interpolation has forced the steady-state error to be the small value specified. It is also important to note that while the closed-loop unit step responses with $C_{lead}(s)$ and $C_2(s)$ have comparable steady-state errors (approximately -1), the closed-loop unit-step response with $C_2(s)$ has a much better transient responses than that with $C_{lead}(s)$. (Similar comment also applies to their disturbance rejection behaviours). Furthermore, it is apparent that trade-off between steady-state error and transient response can be easily achieved with controllers designed via the interpolation approach presented in Section 5.

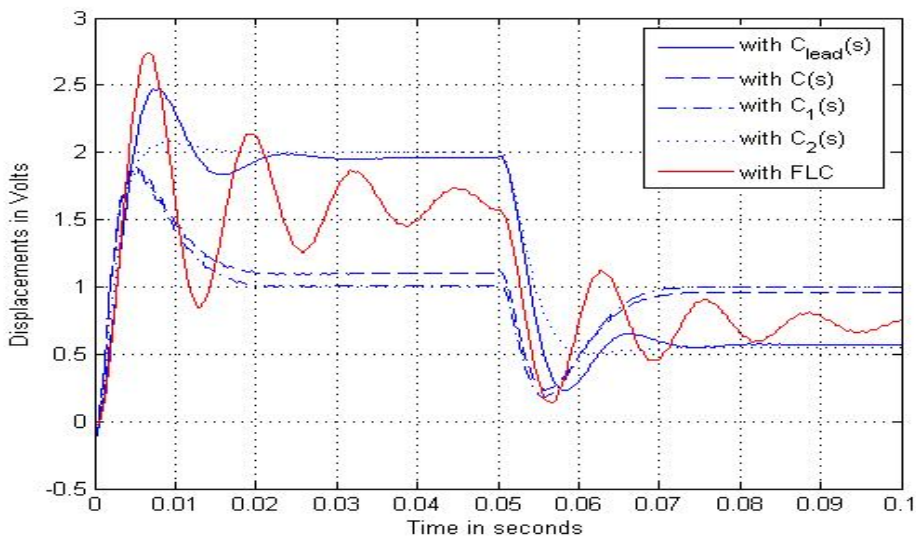

Fig. 13. Closed-loop responses of the MBC500 magnetic bearing system to step reference and step disturbance with controllers $C_{lead}(s)$, $C(s)$, $C_1(s)$, *and* $C_2(s)$, and the designed FLC.

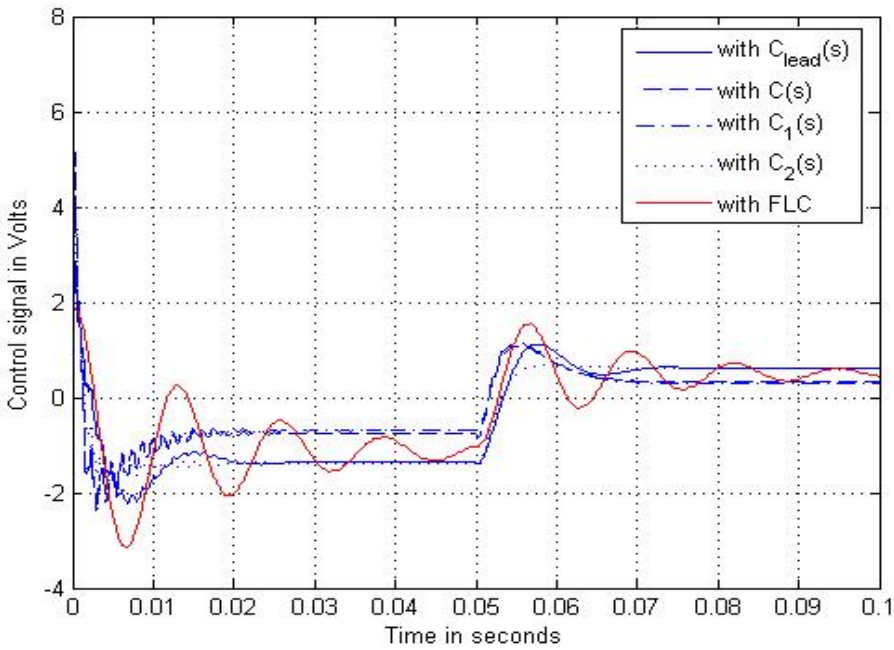

Fig. 14. Closed-loop responses of the MBC500 magnetic bearing system to step reference and step disturbance with controllers $C_{lead}(s)$, $C(s)$, $C_1(s)$, *and* $C_2(s)$, and the designed FLC.

It can also be observed that the closed-loop unit step responses obtained with the designed FLC exhibits more oscillations. However, it must be pointed out that two elliptic notch filters to notch out the resonant modes of the MBC500 magnetic bearing system located at approximately 770 Hz and 2050 Hz were employed with both the conventional controller and the controllers designed via analytical interpolation approach to ensure system stability. For the designed FLC, system stability is achieved without the need of using the two notch filters.

From Figures 13 and 14 it can be seen that the system is stable and reasonably well compensated by all the controllers designed. These controllers are now ready to be coded in C language and implemented in real-time.

8. Implementation of the designed Controllers

In order to implement the designed notch filters and controllers, a dSPACE DS1102 processor board, MatLab, Simulink and dSPACE Control Desk are used. The controllers $C_{lead}(s)$ and $C_2(s)$ are represented as a block diagram via a Simulink file, which allows it to be connected to the ADC and the DAC of the DS1102 processor board. The DS1102 DSP board can then execute the designed controllers (discretized via the bilinear-transformation method) through MatLab's Real-Time Workshop.

In this magnetic bearing system, for the model based controllers the notch filters act to provide damping to the rotor resonances near 770 Hz and 2050 Hz. The sampling frequency was originally chosen to be 25 kHz to avoid aliasing of frequencies within the normal operating frequency range (Shi & Revell, 2002). The maximum possible sampling frequency with the FLC was 20 kHz (Shi & Lee, 2008) due to the longer C code implementation requirement of the FLC. In order to have a fair comparison of the system responses, the sampling frequencies of the model based controllers and the FLC were both set at 20kHz.

In the following, we shall present and compare the experimental results. Preliminary observation has revealed that the performance of the controller $C_2(s)$ designed via analytical interpolation approach is most similar to $C_{lead}(s)$ and the FLC. As a result, the performance of $C_2(s)$ will be investigated in detail in the implementation. We shall first compare the results for the model based controllers and the FLC under steady-state conditions. We shall then compare the disturbance rejection results of the closed-loop system employing each of these controllers.

8.1 Comparison of Steady-state Responses

Figure 15 shows the steady-state responses of the magnetic bearing system when it is under the control of the model based controllers and the FLC, respectively.

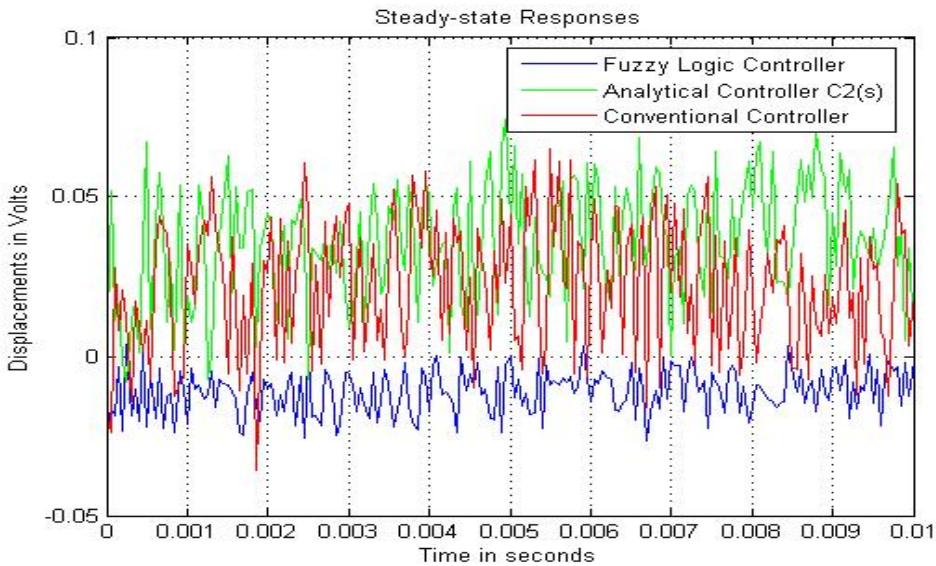

Fig. 15. Steady-state responses with the model based controllers and FLC

It can be seen in Figure 15 that the displacement sensor outputs were noisy when the magnetic bearing system is controlled by either the model based controller or the FLC. However, the response with the FLC has a smaller steady-state error (i.e. closer to zero). Investigation via analysis and simulation has revealed that the source of the noise in the outputs was measurement noise.

8.2 Comparison of Step and Disturbance Rejection Responses

Figure 16 and Figure 17 show the displacement sensor output and the controller output, respectively, when a step disturbance of 0.05V is applied to the channel 1 input of the magnetic bearing system when it is controlled with the model based conventional controller $C_{lead}(s)$. Note that the displacement sensor output is multiplied by a factor of 10 when it is transmitted through the DAC.

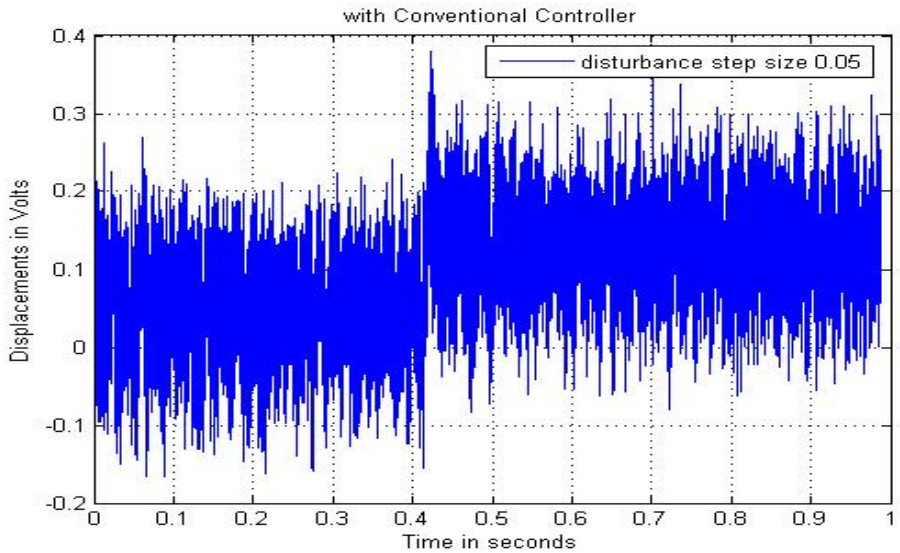

Fig. 16. Displacement output of the MBC500 magnetic bearing system with the model based controller $C_{lead}(s)$.

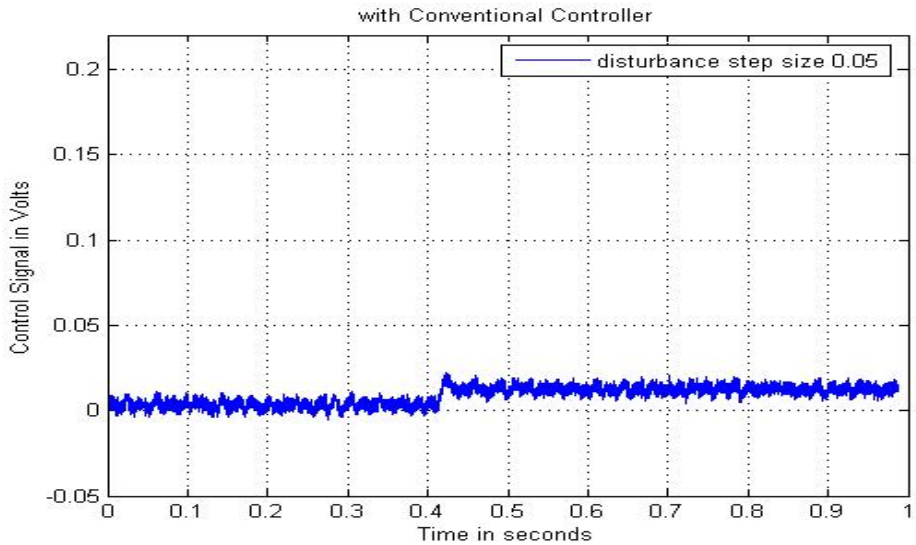

Fig. 17. Control signal of the MBC500 magnetic bearing system with the model based controller $C_{lead}(s)$.

Figure 18 and Figure 19 show the displacement sensor output and the controller output, respectively, when a step change in disturbance of *0.1V* is applied to the channel 1 input of the magnetic bearing system when it is controlled with the model based controller.

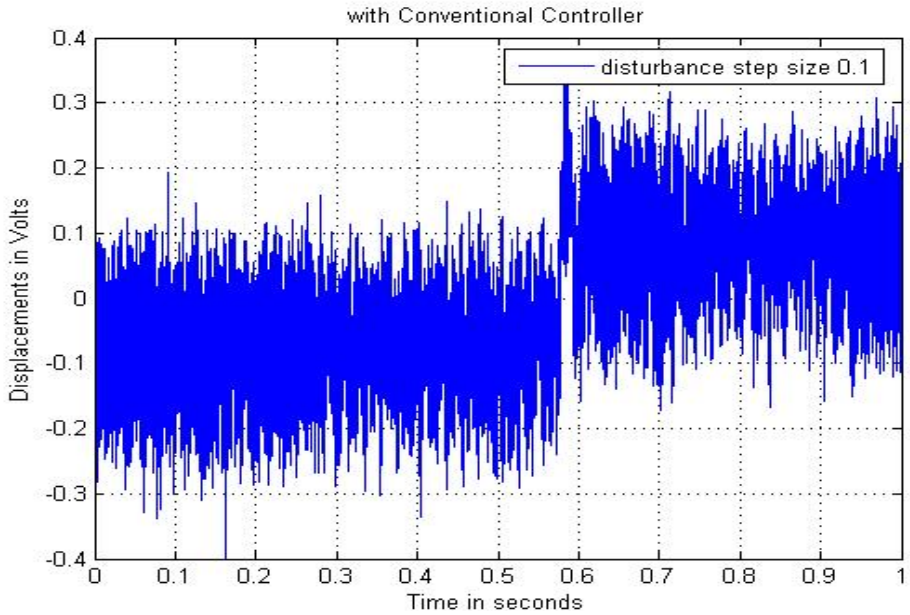

Fig. 18. Step response of the MBC500 magnetic bearing system with the model based controller $C_{lead}(s)$.

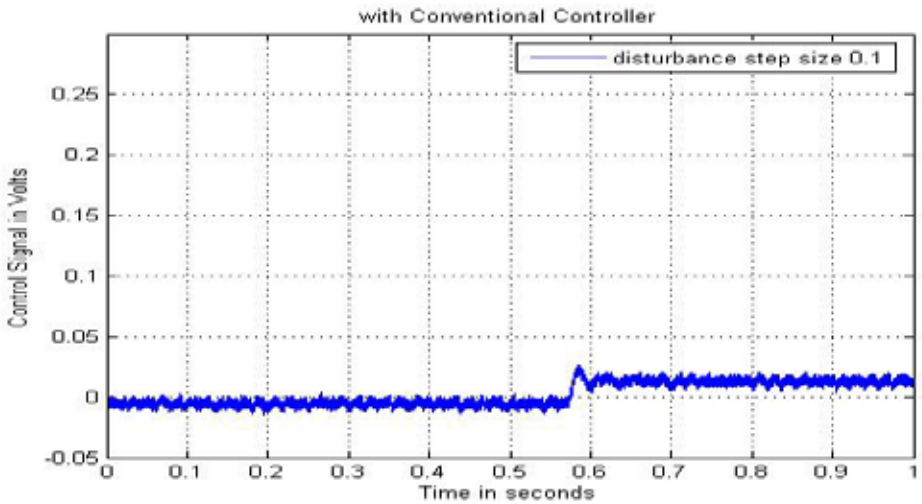

Fig. 19. Control signal of the MBC500 magnetic bearing system with the model based controller $C_{lead}(s)$.

Figure 20 and Figure 21 show the displacement sensor output and the controller output, respectively, when a step change in disturbance of *0.5V* is applied to the channel *1* input of the magnetic bearing system when it is controlled with the conventional controller $C_{lead}(s)$.

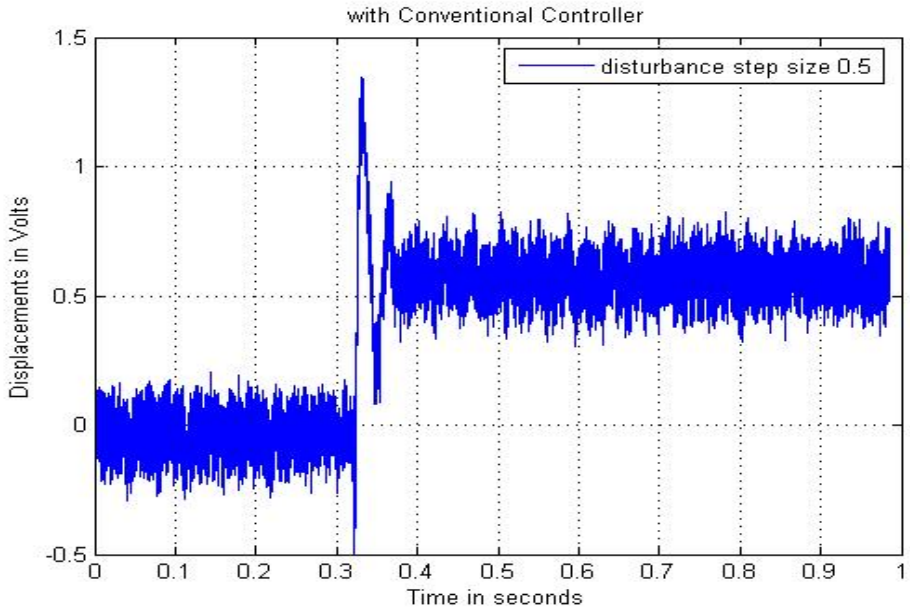

Fig. 20. Step response of the MBC500 magnetic bearing system with the model based controller $C_{lead}(s)$.

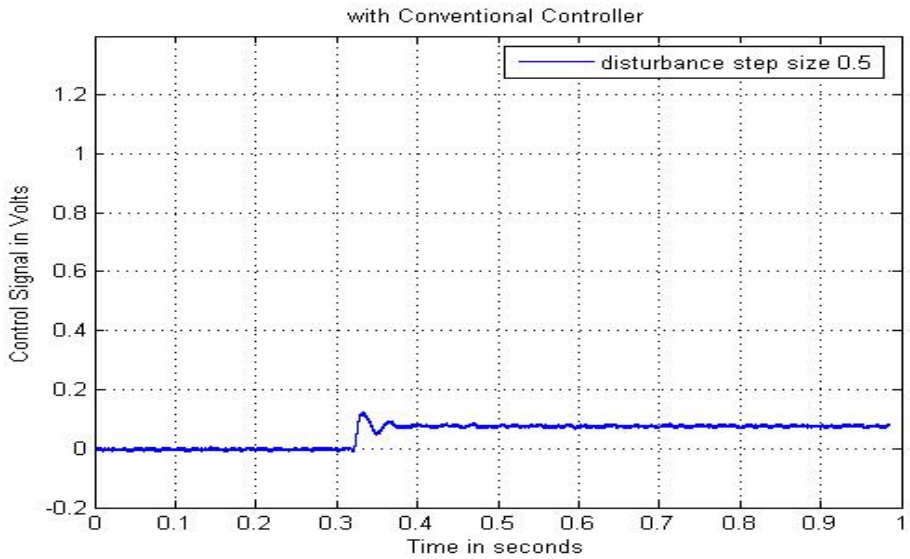

Fig. 21. Control signal of the MBC500 magnetic bearing system with the model based controller $C_{lead}(s)$.

It can be seen from the above figures that the magnetic bearing system remain stable under the control of the model based conventional controller when a step change in disturbance of is applied to its channel *1* input. Similar results were also obtained from other channels.

Figure 22 and Figure 23 show the displacement sensor output and the controller output, respectively, when a step change in disturbance of *0.05V* is applied to the channel *1* input of the magnetic bearing system when it is controlled with the analytical controller $C_2(s)$.

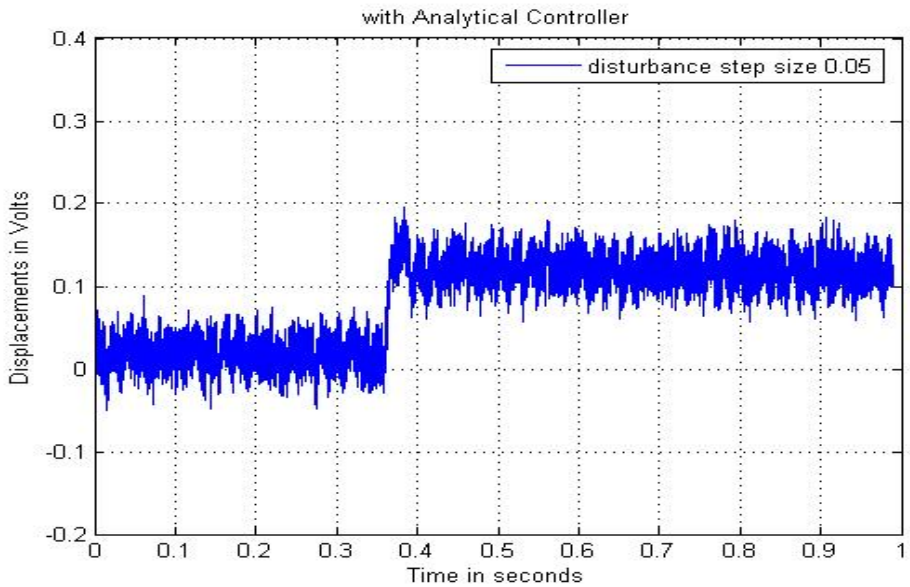

Fig. 22. Displacement output of the MBC500 magnetic bearing system with the analytical controller $C_2(s)$.

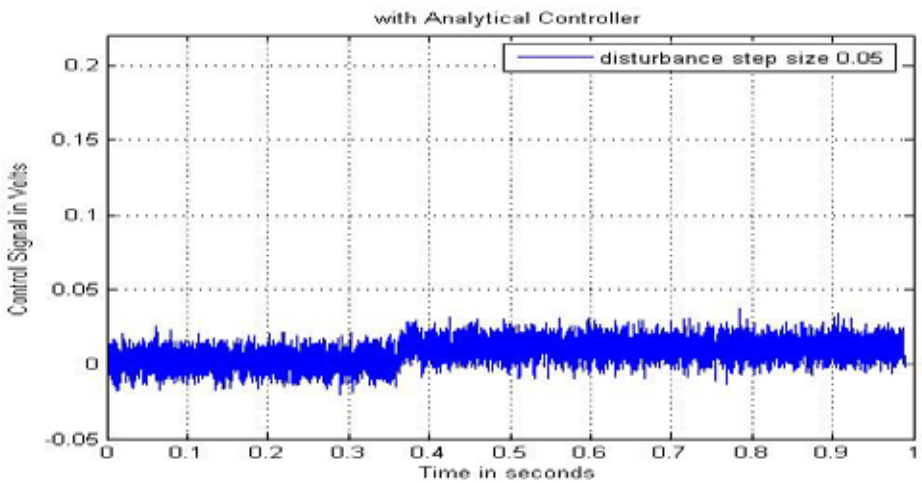

Fig. 23. Control signal of the MBC500 magnetic bearing system with the analytical controller $C_2(s)$.

Figure 24 and Figure 25 show the displacement sensor output and the controller output, respectively, when a step change in disturbance of *0.1V* is applied to the channel *1* input of the magnetic bearing system when it is controlled with the analytical controller $C_2(s)$.

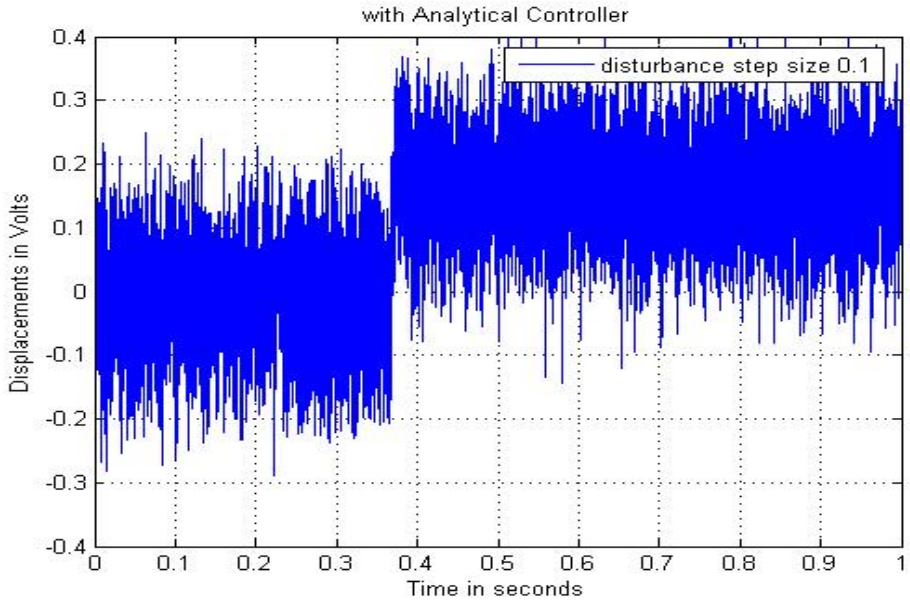

Fig. 24. Displacement output of the MBC500 magnetic bearing system with the analytical controller $C_2(s)$.

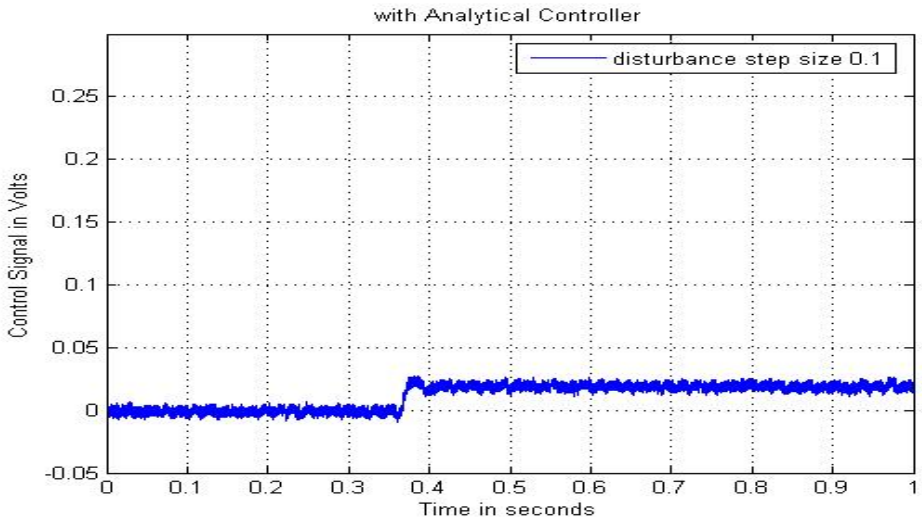

Fig. 25. Control signal of the MBC500 magnetic bearing system with the analytical controller $C_2(s)$.

Figure 26 and Figure 27 show the displacement sensor output and the controller output, respectively, when a step change in disturbance of *0.5V* is applied to the channel *1* input of the magnetic bearing system when it is controlled with the analytical controller $C_2(s)$.

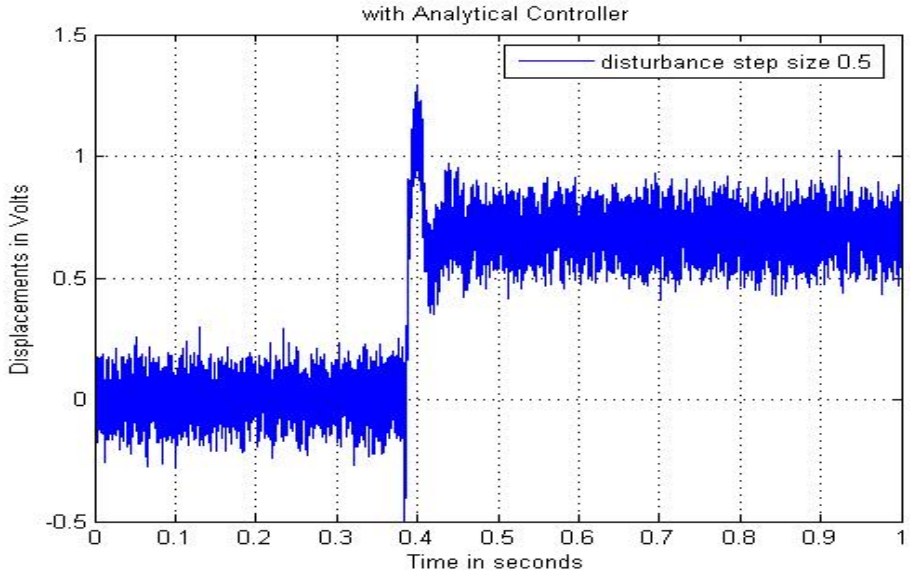

Fig. 26. Displacement output of the MBC500 magnetic bearing system with the analytical controller $C_2(s)$.

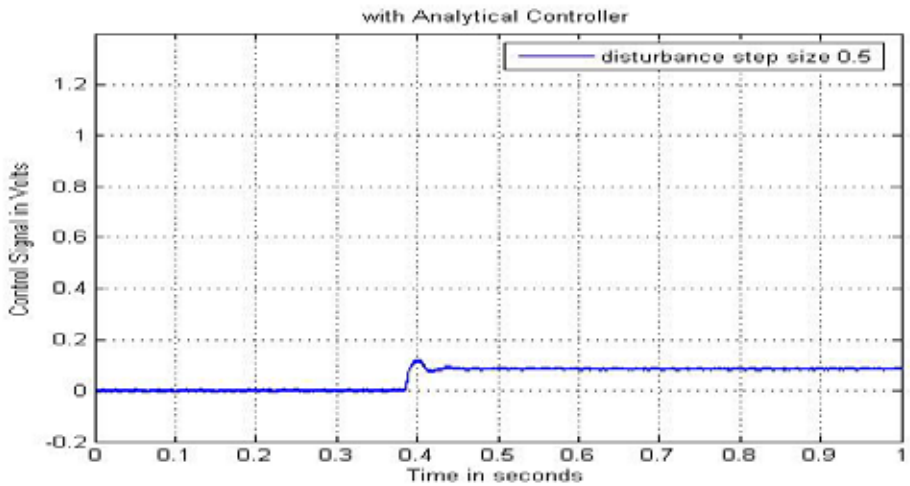

Fig. 27. Control signal of the MBC500 magnetic bearing system with the analytical controller $C_2(s)$.

Figure 28 and Figure 29 show the displacement sensor output voltage and the controller output voltage, respectively, when a step of *0.05V* is applied to channel *1* of the magnetic bearing system, when it is controlled with the FLC.

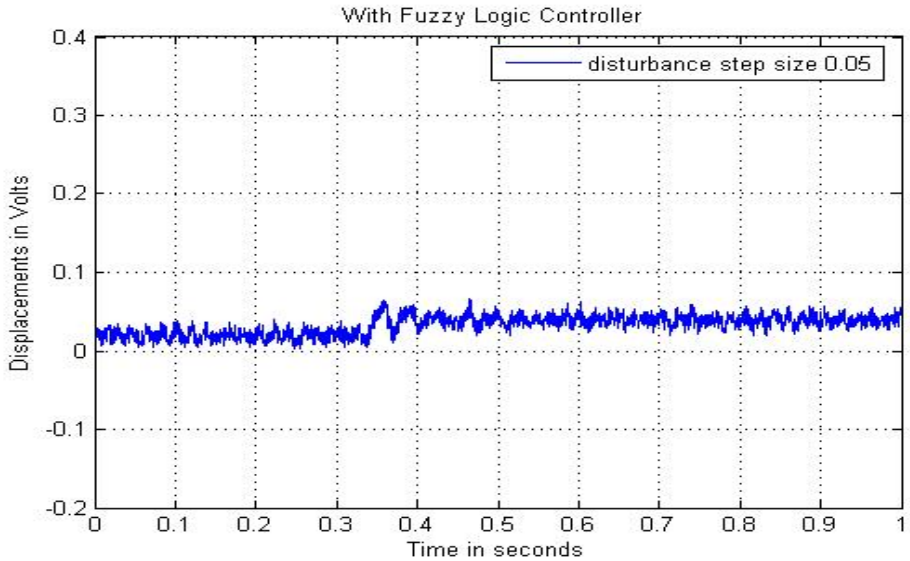

Fig. 28. Step response of the MBC500 magnetic bearing system with the FLC.

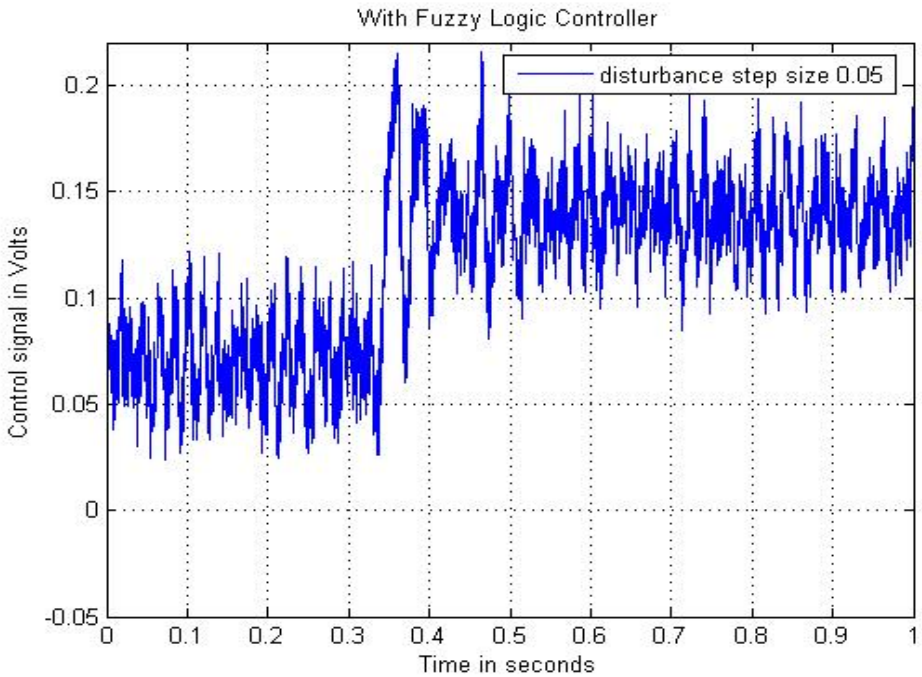

Fig. 29. Control signal of the MBC500 magnetic bearing system with the FLC.

Figure 30 and Figure 31 show the displacement sensor output voltage and the controller output voltage, respectively, when a step of *0.1V* is applied to channel *1* of the magnetic bearing system, when it is controlled with the FLC.

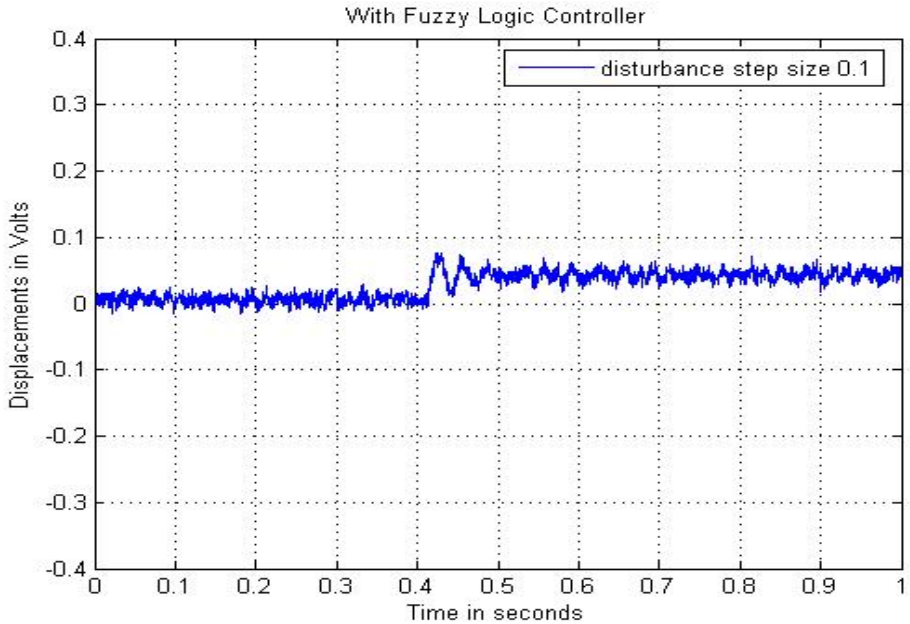

Fig. 30. Step response of the MBC500 magnetic bearing system with the FLC.

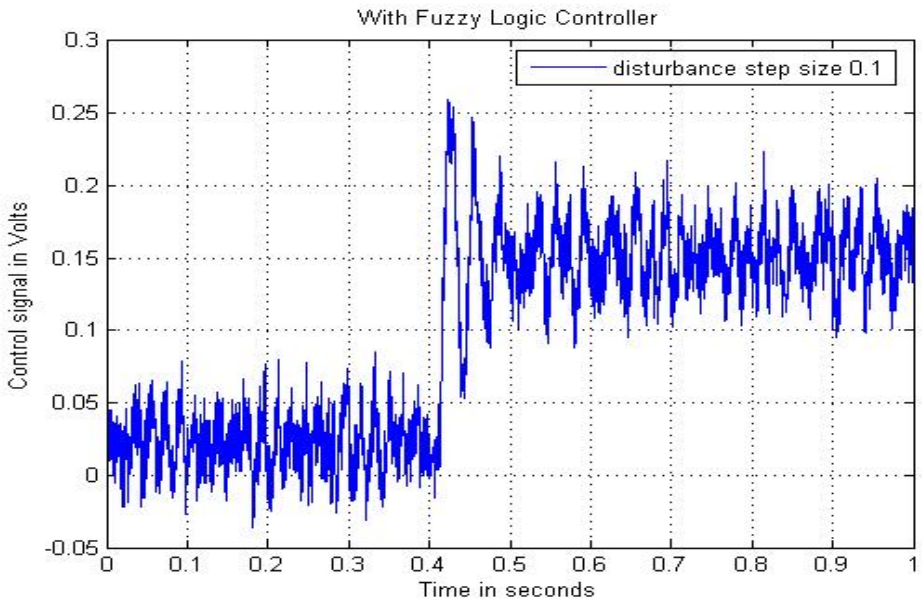

Fig. 31. Control signal of the MBC500 magnetic bearing system with the FLC.

Figure 32 and Figure 33 show the displacement sensor output and the controller output, respectively, when a step change in disturbance of *0.5V* is applied to the channel *1* input of the magnetic bearing system when it is controlled with the FLC.

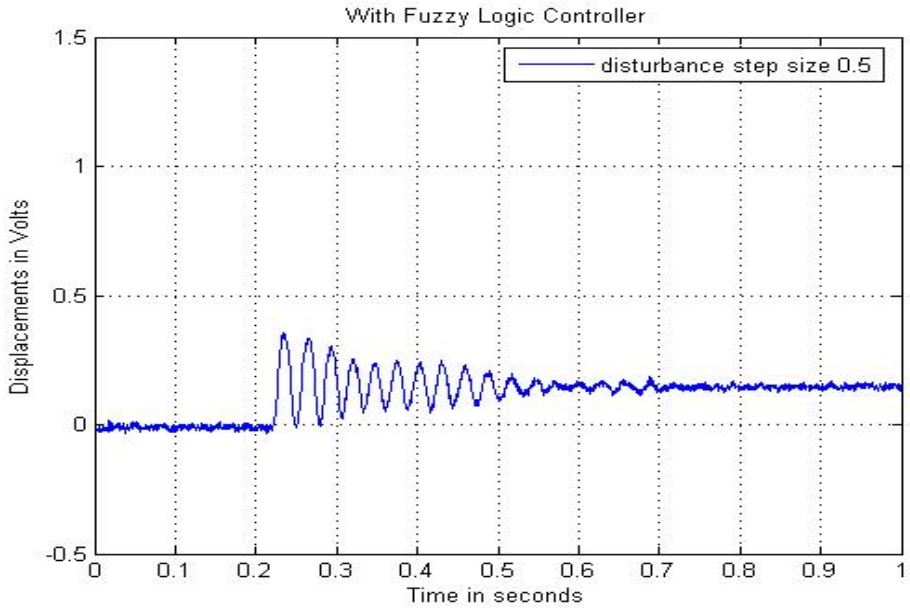

Fig. 32. Step response of the MBC500 magnetic bearing system with the FLC.

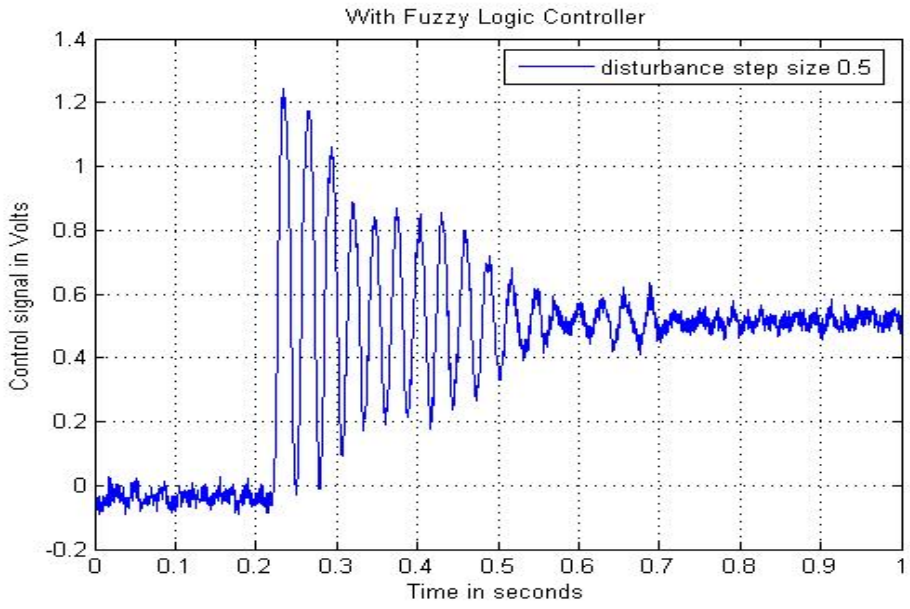

Fig. 33. Control signal of the MBC500 magnetic bearing system with the FLC.

The FLC was tested extensively to ensure that it can operate in a wide range of conditions. These include testing its tolerance to the resonances of the MBC500 system by tapping the rotor with screwdrivers. The system remained stable throughout the whole regime of testing. The MBC500 magnetic bearing system has four different channels; three of the channels were successfully stabilized with the single FLC designed without any modifications or further adjustments. For the channel that failed to be robustly stabilized, the difficulty could be attributed to the strong resonances in that particular channel which have very large magnitude. After some tuning to the input and output scaling values of the FLC, robust stabilization was also achieved for this difficult channel.

Comparing Figures 16 and 22, 18 and 24, 20 and 26, it can be seen that the system step responses with the controller designed via analytical interpolation approach exhibit smaller overshoot and shorter settling time with similar control effort as shown in Figures 17 and 23, 19 and 25, 21 and 27. The step and step disturbance rejection responses with the designed FLC exhibit smaller steady-state error and overshoot as shown in Figures 28, 30 and 32 with much bigger control signal displayed in Figures 29, 31 and 33. However, it must be pointed out that the system stability is achieved with the designed FLC without using the two notch filters to eliminate the unwanted resonant modes.

9. Conclusion and future work

In this chapter, the controller structure and performance of a conventional controller and an analytical feedback controller have been compared with those of a fuzzy logic controller (FLC) when they are applied to the MBC500 magnetic bearing system stabilization problem.

The conventional and the analytical feedback controller were designed on the basis of a reduced order model obtained from an identified 8^{th}-order model of the MBC500 magnetic bearing system. Since there are resonant modes that can threaten the stability of the closed-loop system, notch filters were employed to help secure stability.

The FLC uses error and rate of change of error in the position of the rotor as inputs and produces an output voltage to control the current of the amplifier in the magnetic bearing system. Since a model is not required in this approach, this greatly simplified the design process. In addition, the FLC can stabilize the magnetic bearing system without the use of any notch filters. Despite the simplicity of FLC, experimental results have shown that it produces less steady-state error and has less overshoot than its model based counterpart.

While the model based controllers are linear systems, it is not a surprise that their stability condition depends on the level of the disturbance. This is because the magnetic bearing system is a nonlinear system. However, although the FLC exhibits some of the common characteristics of high authority linear controllers (small steady-state error and amplification of measurement noise), it does not have the low stability robustness property usually associated with such high gain controllers that we would have expected.

Future work will include finding some explanations for the above unusual observation on FLC. We believe the understanding achieved through attempting to address the above issue would lead to better controller design methods for active magnetic bearing systems.

10. References

Williams, R.D, Keith, F.J., and Allaire, P.E. (1990). Digital Control of Active Magnetic Bearing, *IEEE trans. on Indus. Electr*. Vol. 37, No. 1, pp. 19-27, February 1990.

Lee, K.C, Jeong, Y.H., Koo, D.H., and Ahn, H. (2006) Development of a Radial Active Magnetic Bearing for High Speed Turbo-machinery Motors, *Proceedings of the 2006 SICE-ICASE International Joint Conference*, 1543-1548, 18-21 October, 2006.

Bleuler, H., Gahler, C., Herzog, R., Larsonneur, R., Mizuno, T., Siegwart, R. (1994) Application of Digital Signal Processors for Industrial Magnetic Bearings, *IEEE Trans. on Control System Technology,* Vol. 2, No. 4, pp. 280-289, December 1994.

Magnetic Moments (1995), LLC, *MBC 500 Magnetic Bearing System Operating Instructions*, December, 1995.

Shi, J. and Revell, J. (2002) System Identification and Reengineering Controllers for a Magnetic Bearing System, *Proceedings of the IEEE Region 10 Technical Conference on Computer, Communications, Control and Power Engineering*, Beijing, China, pp.1591-1594, 28-31 October, 2002.

Dorato, P. (1999) *Analytic Feedback System Design: An Interpolation Approach*, Brooks/Cole, Thomson Learning, 1999.

Dorato, P., Park, H.B., and Li, Y. (1989) An Algorithm for Interpolation with Units in H∞, with Applications to Feedback Stabilization, *Automatica*, Vol. 25, pp.427-430, 1989.

Shi, J., and Lee, W.S. (2009) Analytical Feedback Design via Interpolation Approach for the Strong Stabilization of a Magnetic Bearing System, *Proceedings of the 2009 Chinese Control and Decision Conference (CCDC2009)*, Guilin, China, 17-19 June, 2009, pp. 280-285.

Shi, J., Lee, W.S., and Vrettakis, P. (2008) Fuzzy Logic Control of a Magnetic Bearing System, *Proceedings of the 20th Chinese Control and Decision Conference(2008 CCDC),* Yantai, China, 1-6, 2-4 July, 2008.

Shi, J., and Lee, W.S. (2009) An Experimental Comparison of a Model Based Controller and a Fuzzy Logic Controller for Magnetic Bearing System Stabilization, *Proceedings of the 7th IEEE International Conference on Control & Automation (**ICCA**'09)*, Christchurch, New Zealand, 9-11 December, 2009, pp. 379-384.

Habib, M.K., and Inayat-Hussain, J.I. (2003). Control of Dual Acting Magnetic Bearing Actuator System Using Fuzzy Logic, *Proceedings 2003 IEEE International Symposium on Computational Intelligence in Robotics and Automation*, Kobe, Japan, pp. 97-101, July 16-20, 2003.

Morse, N., Smith, R. and Paden, B. (1996) Magnetic Bearing System Identification, *MBC 500 Magnetic System Operating Instructions*, pp.1-14, May 29, 1996.

Van den Hof, P.M.J. and Schrama, R.J.P. (1993) "An indirect method for transfer function estimation from closed-loop data", Automatica, Volume 29, Issue 6, pp.1523-1527, 1993.

Freudenberg, J.S. and Looze, D.P. (1985), Right Half Plane Poles and Zeros and Design Tradeoffs in Feedback Systems, *IEEE Trans. Automat. Control,* 30, pp.555-565, 1985.

Dorato, P. (1999) *Analytic Feedback System Design: An Interpolation Approach*, Brooks/Cole, Thomson Learning, 1999.

Youla, D.C., Borgiorno J.J. Jr., and Lu, C.N. (1974) Single-loop feedback stabilization of linera multivariable dynamical plants, *Automatica*, Vol. 10, 159-173, 1974.

Passino, K.M. and Yurkovich, S. (1998) *Fuzzy Control*, Addison-Wesley Longman, Inc., 1998.

2

Linearization of radial force characteristic of active magnetic bearings using finite element method and differential evolution

Boštjan Polajžer, Gorazd Štumberger, Jože Ritonja and Drago Dolinar
University of Maribor, Faculty of Electrical Engineering and Computer Science
Slovenia

1. Introduction

Active magnetic bearings (AMBs) are used to provide contact-less suspension of a rotor (Schweitzer et al., 1994). No friction, no lubrication, precise position control, and vibration damping make AMBs appropriate for different applications. In-depth debate about the research and development has been taken place the last two decades throughout the magnetic bearings community (ISMB12, 2010). However, in the future it is likely to be focused towards the superconducting applications of magnetic bearings (Rosner, 2001). Nevertheless, the discussion in this work is restricted to the design and analysis of "classical" AMBs, which are indispensable elements for high-speed, high-precision machine tools (Larsonneur, 1994). Two radial AMBs, which control the vertical and horizontal rotor displacements in four degrees of freedom (DOFs) are placed at the each end of the rotor, whereas an axial AMB is used to control the fifth DOF, as it is shown in Fig. 1. Rotation (the sixth DOF) is controlled by an independent driving motor. Because AMBs constitute an inherently unstable system, a closed-loop control is required to stabilize the rotor position. Different control techniques (Knospe & Collins, 1996) are employed to achieve advanced features of AMB systems, such as higher operating speeds or control of the unbalance response. However, a decentralized PID feedback is, even nowadays, normally used in AMB industrial applications, whereas prior to a decade ago, more than 90% of the AMB systems were based on PID decentralized control (Bleuer et al., 1994).

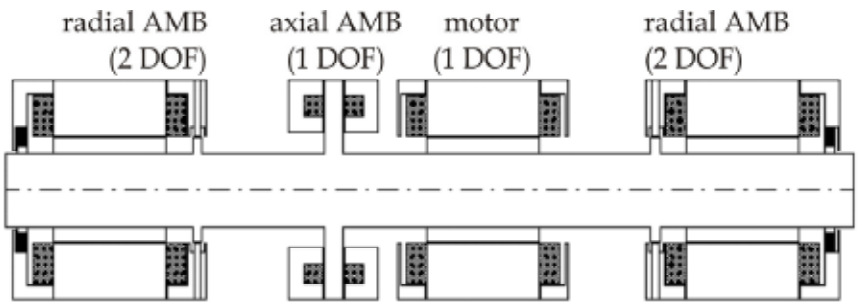

Fig. 1. Typical AMB system

The development and design of AMBs is a complex process, where possible interdependencies of requirements and constrains should be considered. This can be done either by trials using analytical approach (Maslen, 1997), or by applying numerical optimization methods (Meeker, 1996; Carlson-Skalak et al., 1999; Štumberger et al., 2000). AMBs are a typical non-linear electro-magneto-mechanical coupled system. A combination of stochastic search methods and analysis based on the finite element method (FEM) is recommended for the optimization of such constrained, non-linear electromagnetic systems (Hameyer & Belmans, 1999).
In this work the numerical optimization of radial AMBs is performed using differential evolution (DE) – a direct search algorithm (Price et al., 2005) – and the FEM (Pahner et al., 1998). The objective of the optimization is to linearize current and position dependent radial force characteristic over the entire operating range. The objective function is evaluated by two dimensional FEM-based magnetostatic computations, whereas the radial force is determined using Maxwell's stress tensor method. Furthermore, through the comparison of the non-optimized and optimized radial AMB, the impact of non-linearities of the radial force characteristic, on static and dynamic properties of the overall system is evaluated over the entire operating range.

2. Radial Force Characteristic of Active Magnetic Bearings

An eight-pole radial AMB is discussed, as it is shown in Fig. 2. The windings of all electromagnets are supplied in such a way, that a NS-SN-NS-SN pole arrangement is achieved. Four independent magnetic circuits – electromagnets are obtained in such way. The electromagnets in the same axis generate the attraction forces acting on the rotor in opposite directions. The resultant radial force of such a pair of electromagnets is a non-linear function of the currents, rotor position, and magnetization of the iron core. The differential driving mode of currents is introduced by the following definitions: $i_1 = I_0 + i_x$, $i_2 = I_0 - i_x$, $i_3 = I_0 + i_y$, and $i_4 = I_0 - i_y$, where I_0 is the constant bias current, i_x and i_y are the control currents in the x and y axis, where $| i_x | \leq I_0$, and $| i_y | \leq I_0$.

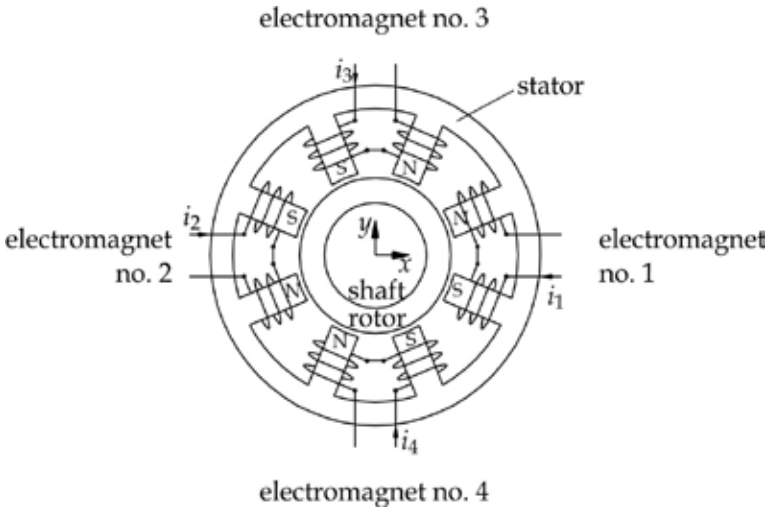

Fig. 2. Eight-pole radial AMB

2.1 Linearized AMB model for one axis

When the magnetic non-linearities and cross-coupling effects are neglected, the force generated by a pair of electromagnets in the x axis can be expressed by (1). δ_0 is the nominal air gap for the rotor central position ($x = y = 0$), μ_0 is permeability of vacuum, N is the number of turns of each coil, and A is the area of one pole. Note that the force generated by a pair of electromagnets in the y axis is defined in the same way as in (1).

$$F_x = \frac{1}{4}\mu_0 A N^2 \cos(\pi/8)\left(\left(\frac{I_0 + i_x}{\delta_0 - x}\right)^2 - \left(\frac{I_0 - i_x}{\delta_0 + x}\right)^2\right) \tag{1}$$

Non-linear equation (1) can be linearized at a nominal operating point ($x = 0$, $i_x = 0$). The obtained linear equation (2) is valid only in the vicinity of the point of linearization. In such way two parameters are introduced at a nominal operating point; the current gain $h_{x,\mathrm{nom}}$ by (3) and the position stiffness $c_{x,\mathrm{nom}}$ by (4).

$$F_x = h_{x,\mathrm{nom}}\, i_x + c_{x,\mathrm{nom}}\, x \tag{2}$$

$$h_{x,\mathrm{nom}} = \left.\frac{\partial F_x}{\partial i_x}\right|_{(i_x=0,x=0)} = \mu_0 A N^2 \cos(\pi/8)\,\frac{I_0}{\delta_0^2} \tag{3}$$

$$c_{x,\mathrm{nom}} = \left.\frac{\partial F_x}{\partial x}\right|_{(i_x=0,x=0)} = \mu_0 A N^2 \cos(\pi/8)\,\frac{I_0^2}{\delta_0^3} \tag{4}$$

The motion of the rotor between two electromagnets in the x axis is described by (5), where m is the mass of the rotor. When the equation (2) is used then the linearized AMB model for one axis is described by (6).

$$F_x = m\frac{d^2x}{dt^2} \tag{5}$$

$$\frac{d^2x}{dt^2} = \frac{h_{x,\mathrm{nom}}}{m} i_x + \frac{c_{x,\mathrm{nom}}}{m} x \tag{6}$$

The dynamic model (6) is used for determining the controller settings, where the nominal values of the model parameters are used ($h_{x,\mathrm{nom}}$ and $c_{y,\mathrm{nom}}$). However, due to the magnetic non-linearities, the current gain and position stiffness vary according to the operating point. Consequently, a damping and stiffness of the closed-loop system might be deteriorated in the cases of high signal amplitudes, such as heavy load unbalanced operation.

2.2 Magnetic field distribution and radial force computation using FEM

The magnetostatic problem is formulated by Poisson's equation (7), where **A** denotes the magnetic vector potential, ν is the magnetic reluctivity, **J** is the current density, • denotes the dot product and ∇ is the Hamilton's differential operator.

$$\nabla \bullet (\nu \nabla \mathbf{A}) = -\mathbf{J} \tag{7}$$

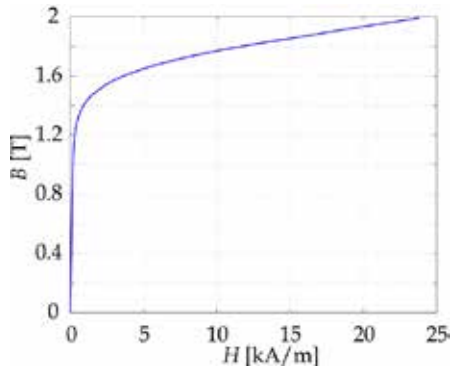

Fig. 3. *B-H* characteristic for laminated ferromagnetic material 330-35-A5

The Poisson's equation (7) is solved numerically using the two dimensional FEM. The stator and rotor are constructed of laminated steel sheets – lamination thickness is 0.35 mm. Ferromagnetic material 330-35-A5, whose magnetization characteristic is shown in Fig. 3 is used. The discretization of the model is shown in Fig. 4a), where standard triangular elements are applied. The non-linear solution of the magnetic vector potential (7) is computed by a conjugate gradient and the Newton-Raphson method. During the analysis of errors, adaptive mesh refinement is applied until the solution error is smaller than a predefined value. Note that the initial mesh is composed of 9973 nodes and 19824 elements, whereas 16442 nodes and 32762 elements are used for the refined mesh. In Fig. 4b) the refined mesh is shown for the air gap region. Example of the magnetic field distribution is shown in Fig. 5. The radial force is computed by Maxwell's stress tensor method (8), where $\boldsymbol{\sigma}$ is Maxwell's stress tensor, $\mathbf{n}$ is the unit vector normal to the integration surface S and $\mathbf{B}$ is the magnetic flux density. The integration is performed over a contour placed along a middle layer of the three-layer mesh in the air gap, as it is shown in Fig. 4b).

$$\mathbf{F} = \oint_S \boldsymbol{\sigma}\, dS = \int_S \left(\frac{1}{\mu_0} (\mathbf{B} \bullet \mathbf{n}) \mathbf{B} - \frac{1}{2\mu_0} \mathbf{B}^2 \mathbf{n} \right) dS \tag{8}$$

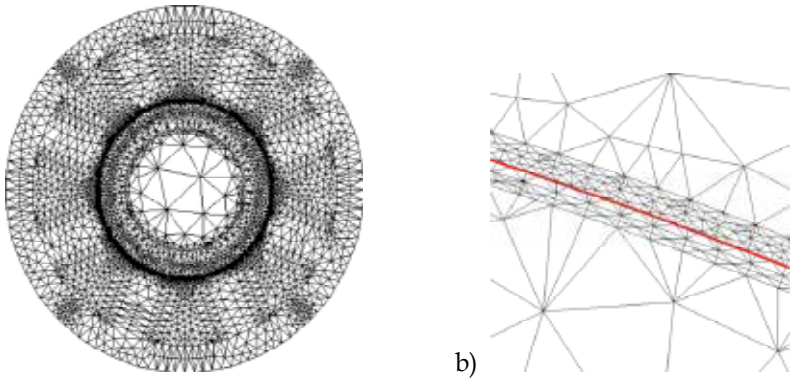

a) b)

Fig. 4. Discretization of the model (a), and refined mesh in the air gap with integration contour for radial force computation (b)

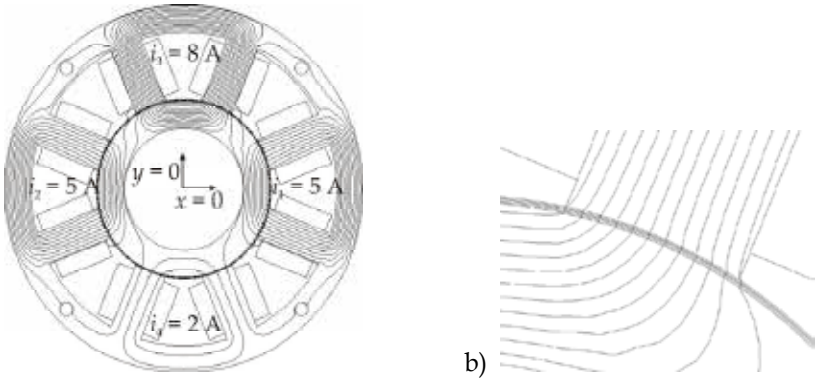

a) b)

Fig. 5. Magnetic field distribution for the case $i_x = 0$ A, $i_y = 3$ A, $I_0 = 5$ A, and $x = y = 0$ mm; equipotential plot for the whole geometry (a), and in the air gap and the pole (b)

2.3 Impact of magnetic non-linearities on radial force characteristic

The flux density plot and the equipotential plot is given in Figs. 5 and 6 for a heavy load condition in the y axis ($i_x = 0$ A, $i_y = 3$ A) at the rotor central position ($x = y = 0$). Note that for this case only the radial force in the y axis is generated, whereas the component in the x axis is zero. In Fig. 6 the iron core saturation in the region of the upper electromagnet is observed; an average value of the flux density in the iron core is 1.31 T, whereas at the corners the maximum value of even 1.86 T is reached. However, value of the flux density in the air gap of the upper electromagnet is 1.09 T, as it is marked in Fig. 6. Due to the iron core saturation in the upper electromagnet the radial force generated by a pair of electromagnets in the y axis is reduced. Moreover, the flux lines of the upper electromagnet also link with all other electromagnets, as it is shown in Figs. 5 and 6. Due to these magnetic cross-couplings the asymmetrical air gap flux density is generated in both electromagnets in the x axis, i.e. 0.67 T and 0.70 T (Figure 6). Consequently, electromagnets in the x axis generate a negative radial force component in the y axis, as it is shown by the vector analysis in Fig. 6. In such way, the resultant radial force in the y axis is additionally reduced.

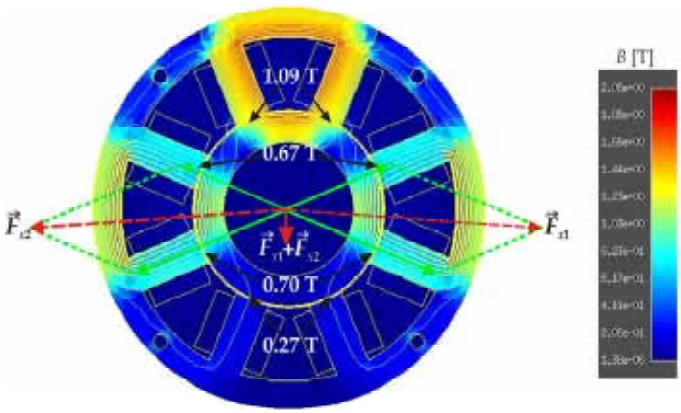

Fig. 6. Magnetic field distribution for the case $i_x = 0$ A, $i_y = 3$ A, $I_0 = 5$ A, and $x = y = 0$ mm with air gap values of the flux density and vector analysis of a radial force of a pair of electromagnets in the x axis

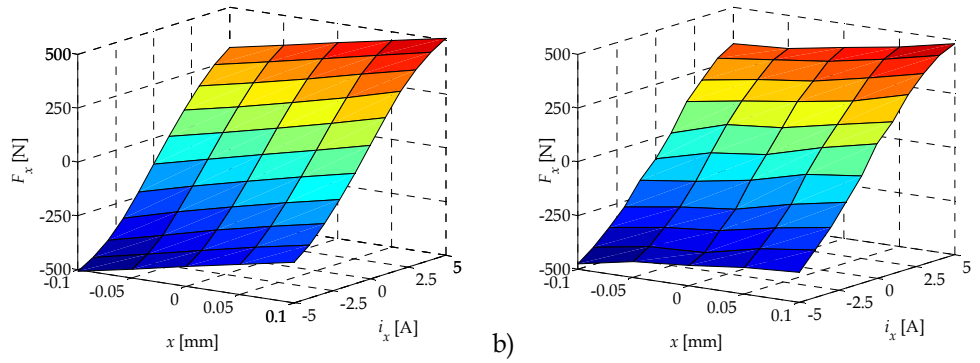

a) b)

Fig. 7. Radial force characteristic $F_x(i_x,x)$: FEM-computed (a), and measured (b)

The radial force characteristic $F_x(i_x,i_y,x,y)$ has been calculated over the entire operating range ($i_x \in$ [-5 A, 5 A], $i_y \in$ [-5 A, 5 A], $x \in$ [-0.1 mm, 0.1 mm], $y \in$ [-0.1 mm, 0.1 mm]). The radial force characteristic $F_x(i_x,x)$ is shown in Fig. 7. A good agreement is obtained between the FEM-computed and measured characteristic. Note that the air gap has been increased in FEM computations from 0.4 to 0.45 mm because the magnetic air gap is larger than the geometric one due to the manufacturing process of the rotor steel sheets. The increase of 0.05 mm in the air gap can be compared with the findings in (Antila et al., 1998). Furthermore, the radial force characteristic $F_x(i_x,x)$ obtained by (1) and (2) are shown in Fig. 8 for the discussed radial AMB. Through the comparison between the FEM-computed and analytical results obtained by a non-linear equation (1) (Figs. 7a and 8a), the considerable radial force reduction is determined. However, in the vicinity of the nominal operating point, the radial force characteristic is surprisingly linear, which is verified through the comparison among the FEM-computed and analytical results obtained by a linearized equation (2) (Figs. 7a and 8b). As it has been already mentioned, the radial force is reduced due to the impact of magnetic non-linearities and cross-coupling effects, especially near the operating range margin ($|i_x| > 2$ A, $|x| > 0.05$ mm), which is reached in the cases of a heavy load unbalanced operation. A more detailed analysis is performed in the section 4 through evaluation of variations of the current gain h_x and position stiffness c_x over the entire operating range.

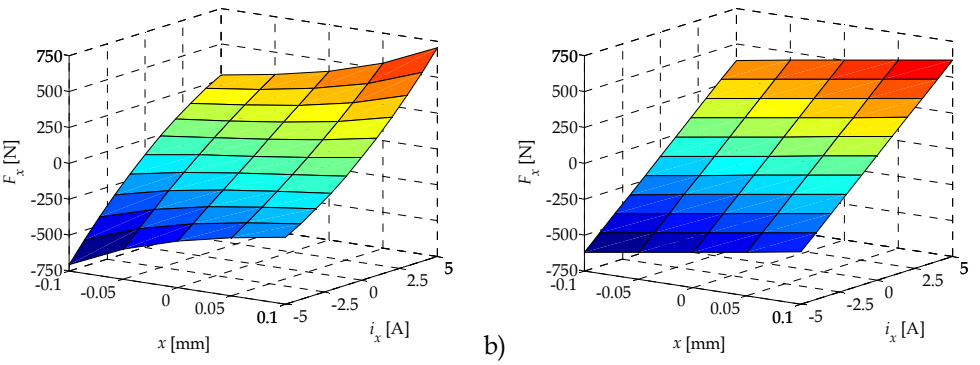

a) b)

Fig. 8. Radial force characteristic $F_x(i_x,x)$: obtained by non-linear equation (1) – (a), and by linearized equation (2) – (b)

3. Design of Radial Active Magnetic Bearings by DE and the FEM

The goal is to design a radial AMB whose radial force characteristic is linear as much as possible over the entire operating range. An experimental radial AMB, shown in Fig. 9 (Polajžer, 2002), is considered for the initial design.
In the author's opinion, DE in combination with the FEM-based analysis is at present still one of the most powerful tools for optimization of such a problem class, where the dependency of the objective function on the design parameters is unknown. According to (Pahner et al., 1998), for optimization of electromagnetic devices in combination with the FEM, DE converges faster and is more stable when compared to other stochastic direct search algorithms such as simulated annealing and self-adaptive evolution strategies. In this work a DE/FEM-based design procedure for radial AMBs is applied, similar to the procedure proposed in our earlier work (Polajžer et al., 2008).

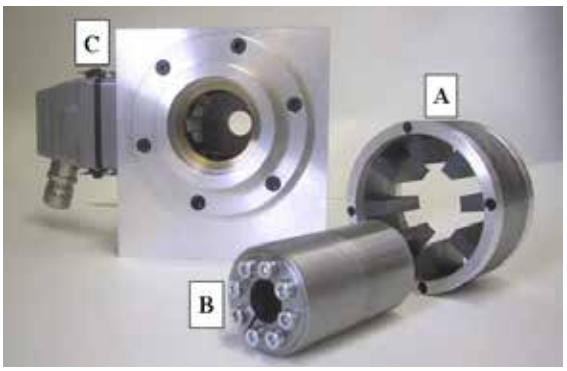

Fig. 9. Experimental radial AMB – initial design: A – stator, B – rotor, C – housing

3.1 Objective function and design parameters

The objective function should be formulated in such a way, that contradictory partial aims are avoided. Otherwise it is possible for the algorithm to stick in a local minimum. This can be prevented by choosing appropriate constraints for the optimization problem. As it is mentioned earlier, the aim is to linearize the radial force characteristic of AMBs over the entire operating range. The non-linearity of a radial force characteristic $F_x(i_x,i_y,x,y)$ is described by the current gain $h_x = \partial F_x/\partial i_x$ and position stiffness $c_x = \partial F_x/\partial x$, which are approximated with differential quotients between two points of the numerically expressed function $F_x(i_x,i_y,x,y)$. The aim of the optimization is thus formulated as a minimization of variations of the linearized AMB model parameters.
The objective function q and penalties p_1, p_2 are found empirically and are defined by (9)–(11). The discussed parameter variations are determined by differences between the nominal and maximal parameter values $\Delta h_x = (h_{x,\mathrm{nom}} - h_{x,\mathrm{max}})$ and $\Delta c_x = (c_{x,\mathrm{nom}} - c_{x,\mathrm{max}})$. The nominal parameter values refer to the nominal operating point where the rotor is in the central position ($x = y = 0$), while both control currents equal zero ($i_x = i_y = 0$). The maximal parameter values refer to the maximal rotor eccentricity ($x = y = E_{\mathrm{max}}$) and maximal control currents ($i_x = i_y = I_0$), which is expected for a heavy load unbalanced operation. Note that the differences $\Delta h_{x0} := (h_{x0,\mathrm{nom}} - h_{x0,\mathrm{max}})$ and $\Delta c_{x0} := (c_{x0,\mathrm{nom}} - c_{x0,\mathrm{max}})$ are defined for the initial AMB design.

$$q = 0.8\frac{|\Delta h_y|}{\Delta h_{y0}} + 0.2\frac{|\Delta c_y|}{\Delta c_{y0}} + p_1 + p_2 \tag{9}$$

$$p_1 = 0.8\frac{|\Delta h_y|}{\Delta h_{y0}} \quad \text{if} \quad |\Delta h_y| > 1.1\,\Delta h_{y0} \tag{10}$$

$$p_2 = 0.2\frac{|\Delta c_y|}{\Delta c_{y0}} \quad \text{if} \quad |\Delta c_y| > 1.1\,\Delta c_{y0} \tag{11}$$

The design parameters (x_1, x_2, x_3, x_4) are the rotor yoke width w_{ry}, stator yoke width w_{sy}, pole width w_p (all shown in Fig. 10) and axial length of the bearing l, respectively. The design constraints are fixed mainly by the mounting conditions, which are given by the shaft radius r_{sh} = 17.5 mm and stator outer radius r_s = 52.8 mm (Fig. 10). Two additional constraints are given by the nominal air gap δ_0 = 0.45 mm and the bias current I_0 = 5 A in order to achieve the maximum force slew rate $|dF/dt|_{\max} = 5{\cdot}10^6$ N/s. Furthermore, the maximum eccentricity of the rotor $E_{\max}$ = 0.1 mm is determined in order to prevent the rotor touchdown.

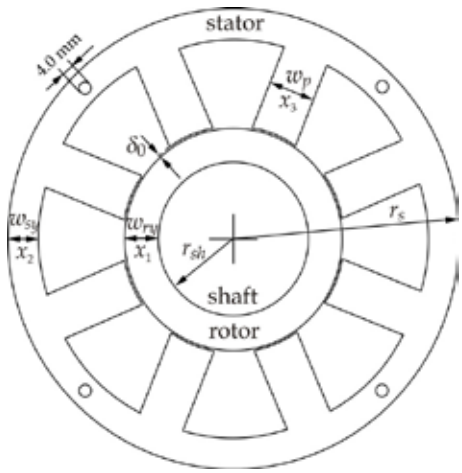

Fig. 10. Geometry of the discussed radial AMB – design parameters are denoted by x_1, x_2, x_3

3.2 Optimization procedure

Optimization of the discussed radial AMBs has been carried out in a special programming environment tuned for FEM-based numerical optimizations (Pahner et al., 1998). The procedure is described by the following steps:

- **Step 1)** The geometry of the initial AMB is described parametrically.
- **Step 2)** The new values for the design parameters are determined by the DE (Price et al., 2005), where strategy "DE/best/1/exp" is used with the population size NP = 25, the DE step size F = 0.5 and for the crossover probability constant CR = 0.75.
- **Step 3)** The geometry, the materials, the current densities, and the boundary conditions are defined. The procedure continues with **Step 2)** if the parameters of the bearing are outside the design constraints.

- **Step 4)** The radial force is computed by the FEM, as it is described in the previous section. Computations are performed for eight different cases: near the nominal operating point for $i_x = 0 \pm 0.1 I_0$ and $x = 0 \pm 0.1 E_{max}$, as well as near the maximal operating point for $i_x = 0.9 I_0 \pm 0.1 I_0$ and $x = E_{max} \pm 0.1 E_{max}$. Note that the control current i_y and the rotor position in the y axis are both zero during these computations.
- **Step 5)** The current gain values $h_{x,nom}$ and $h_{x,max}$, as well as the position stiffness values $c_{x,nom}$ and $c_{x,max}$ are calculated with differential quotients, whereas values of the radial force are obtained from **Step 4)**.
- **Step 6)** The value of the objective function (9) is calculated. The optimization proceeds with **Step 2)** until a minimal optimization parameter variation step or a maximal number of evolutionary iterations are reached.

3.3 Results of the optimization

The objective function has been minimized from 1 to even 0.46, while the minimal value has been reached after 41 iterations. The data and parameters for the initial – non-optimized radial AMB and for the optimized radial AMB are given in Table 1. All design parameters are rounded off to one tenth of a millimetre. Nominal values for the current gain and position stiffness, i.e. at the nominal operating point ($i_x = 0$, $x = 0$), as well as the mass of the rotor of the optimized bearing are, indeed, slightly lower. Consequently, the controller settings need to be recalculated for the new nominal parameter values. In such way the closed-loop system dynamics is not changed. Furthermore, the maximal force at the rotor central position ($x = y = 0$) is increased within the optimized design.

Parameter	Non-optimized	Optimized
Rotor yoke width w_{ry} [mm]	7.7	5.1
Stator yoke width w_{sy} [mm]	7.8	9.1
Pole width w_p [mm]	9.4	5.3
Axial length l [mm]	38	45.6
Current gain $h_{x,nom}$ [N/A]	100.8	95.6
Position stiffness $c_{x,nom}$ [N/mm]	1161	967
Maximal force $F_{x,max}$ [N]	411	435
Rotor mass m [kg]	0.596	0.576

Table 1. Data and parameters for the non-optimized and optimized radial AMB

4. Evaluation of static and dynamic properties of non-optimized and optimized radial AMB

4.1 Current gain and position stiffness characteristics

The current gain and position stiffness characteristics $h_x(i_x,i_y,x,y)$ and $i_x(i_x,i_y,x,y)$ are determined by approximations with differential quotients over the entire operating range ($i_x \in$ [-5 A, 5 A], $i_y \in$ [-5 A, 5 A], $x \in$ [-0.1 mm, 0.1 mm], $y \in$ [-0.1 mm, 0.1 mm]). The obtained results are shown in Figs. 11–14, where characteristics are normalized to the nominal parameter values, which are defined at the nominal operating point ($x = y = 0$, $i_x = i_y = 0$) and are given in Table 1. In Figs. 11 and 13 the current gain and position stiffness characteristics are shown for the non-optimized radial AMB. The current gain and position stiffness characteristics for the optimized radial AMB are shown in Figs. 12 and 14.

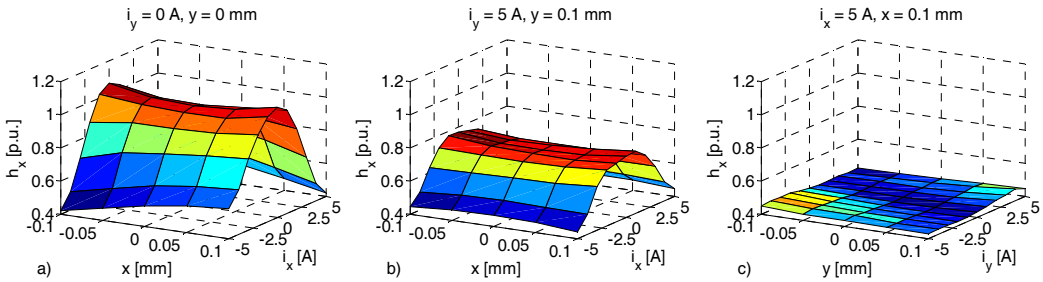

Fig. 11. Current gain characteristic $h_x(i_x,i_y,x,y)$ normalized to the nominal value 100.8 N/A – non-optimized AMB

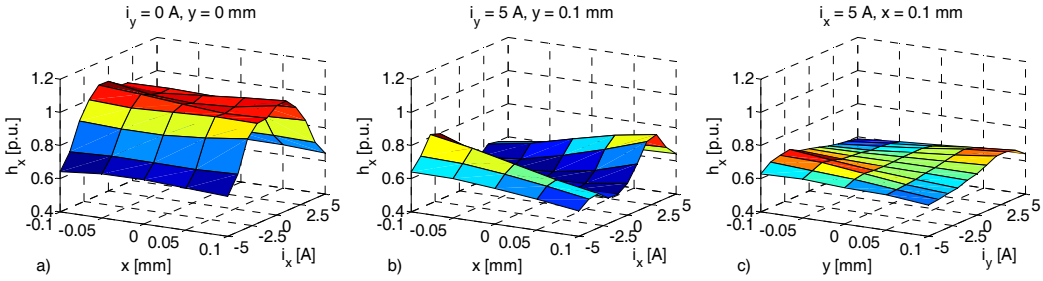

Fig. 12. Current gain characteristic $h_x(i_x,i_y,x,y)$ normalized to the nominal value 95.6 N/A – optimized AMB

In order to evaluate the obtained results, maximal and average variations are determined over the entire operating range ($i_x \in$ [-5 A, 5 A], $i_y \in$ [-5 A, 5 A], $x \in$ [-0.1 mm, 0.1 mm], $y \in$ [-0.1 mm, 0.1 mm]), and for the high signal amplitudes ($|i_x| >$ 2 A, $|i_y| >$ 2 A, $|x| >$ 0.05 mm, $|y| >$ 0.05 mm). Note that all variations are given relatively with respect to the nominal parameter values.

Let us first observe maximal variations of the current gain and the position stiffness. The obtained maximal variation of the current gain is 59% for the non-optimized design and 46% for the optimized design, whereas the obtained maximal variation of the position stiffness is 40% for the non-optimized design and 32% for the optimized design. Average parameter variations are determined next. When observed over the entire operating range, average variation of the current gain is 27% for the non-optimized design and 20% for the optimized design, whereas average variation of the position stiffness is 14% for the non-optimized design and 13% for the optimized design. However, when the margin of the operating range is observed (high signal case), average variation of the current gain is 43% for the non-optimized design and 28% for the optimized design, whereas average variation of the position stiffness is 21% for the non-optimized design and 13% for the optimized design.

Based on the performed evaluation of the obtained results, it can be concluded that the impact of magnetic non-linearities on variations of the linearized AMB model parameters is considerably lower for the optimized AMB, particularly for high signal amplitudes. However, the impact of magnetic cross-couplings slightly increases. Furthermore, normalized values of the current gain and position stiffness are higher for the optimized AMB. Consequently higher load forces are possible for the optimized AMB, as it is shown in the following section.

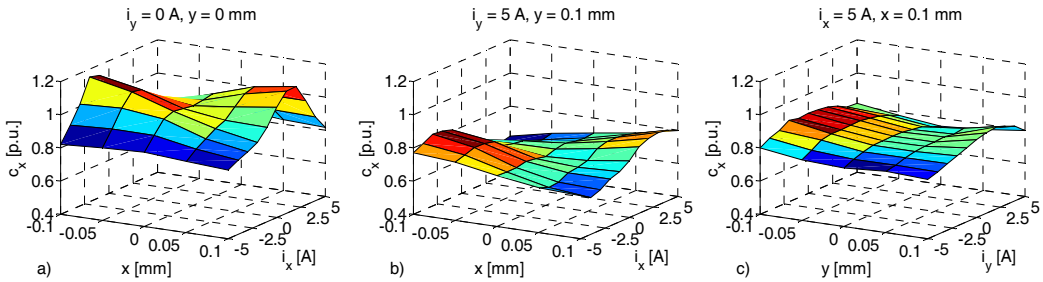

Fig. 13. Position stiffness characteristic $c_x(i_x,i_y,x,y)$ normalized to the nominal value 1161 N/mm – non-optimized AMB

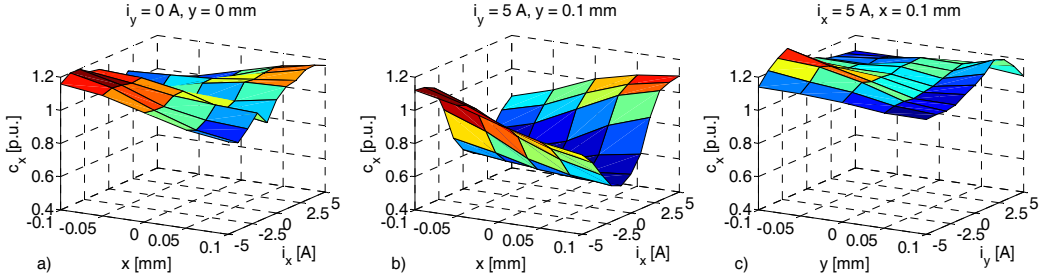

Fig. 14. Position stiffness characteristic $c_x(i_x,i_y,x,y)$ normalized to the nominal value 967 N/mm – optimized AMB

4.2 Dynamic behaviour of a closed-loop controlled system

In order to evaluate the robustness of the closed-loop controlled system, two radial AMBs that control the unbalanced rigid shaft are modeled. A dynamic model is tested for the non-optimized and for the optimized radial AMBs, where calculated radial force characteristics $F_x(i_x,i_y,x,y)$ and $F_y(i_x,i_y,x,y)$ are incorporated. The AMB coils are supplied with ideal current sources, whereas the impact of electromotive forces is not taken into account. The structure of the closed-loop system used in numerical simulations is shown in Fig. 15, where $\mathbf{i} = [i_x, i_y]^T$, $\mathbf{F} = [F_x, F_y]^T$ and $\mathbf{y} = [x, y]^T$ denote current, force and position vectors, respectively. The reference position vector is denoted as $\mathbf{y}_r = [x_r, y_r]^T$, whereas $\mathbf{d} = [F_{dx}, F_{dy} + mg]^T$ is the disturbance vector. In order to evaluate the impact of non-linearities of the radial force characteristic on the closed-loop system, a decentralized control feedback is employed. Position control loops are realized by two independent PID controllers in the x and y axis.

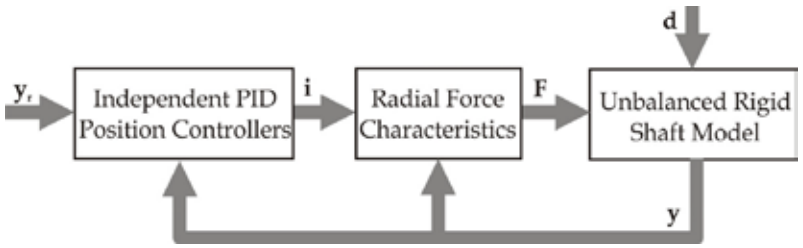

Fig. 15. Structure of the closed-loop AMB system

Responses for the rotor position in the x and y axis and for the control currents i_x and i_y are calculated with Matlab/Simulink®. Fig. 16 shows results of the no rotation test, where the reference rotor position and the disturbance forces are changed in the following sequence: $F_{dy}(0.1) = 250$ N, $y_r(0.3) = -0.09$ mm, $F_{dx}(0.5) = 100$ N and $x_r(0.7) = -0.1$ mm. In the obtained results, it can be noticed that for the case of a reference position change, a considerably higher closed-loop damping is achieved within optimized AMBs, whereas for the heavy load case considerably higher closed-loop stiffness is achieved again within the optimized AMBs. The impact of cross-coupling effects can also be noticed, since changes in the x axis variables are reflected in the y axis variables. Furthermore, from the results shown in Fig. 16, it can be concluded that the control current is much higher for the non-optimized AMBs. Consequently, an operation with the considerably higher load forces can be achieved within the optimized AMBs.

These conclusions are completely confirmed with the results of a simulation unbalance test, which are shown in Figs. 17 and 18. A rotation with 6000 rpm of a highly unbalanced rigid shaft is simulated. Consequently, the unbalanced responses are obtained, which is shown by trajectories of the rotor position and control currents. The trajectories for the unbalanced no load condition are shown together with the trajectories during the 180 N load impact in the y axis. From the obtained results it can be noticed that during the no load condition the rotor eccentricity is slightly larger for the optimized AMBs. Note that this is mostly due to the lower current gain and position stiffness in the linear region. However, during the heavy load operation a current limit is reached (5 A) in the case of the non-optimized AMBs (Fig. 17), whereas the rotor eccentricity is critical (>0.1 mm). On the contrary, the unbalanced response of the optimized design is much less severe, which is mostly due to lower variations of the current gain and position stiffness. The rotor eccentricity stays within the safety boundaries (±0.1 mm), as it is shown in Fig. 18, whereas for the same load condition considerably lower control currents are applied.

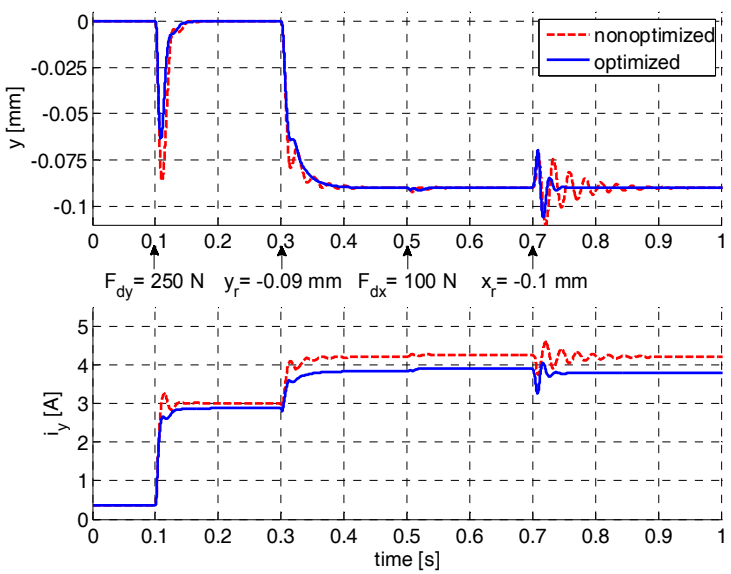

Fig. 16. Simulation-based time responses of the non-optimized and optimized radial AMBs

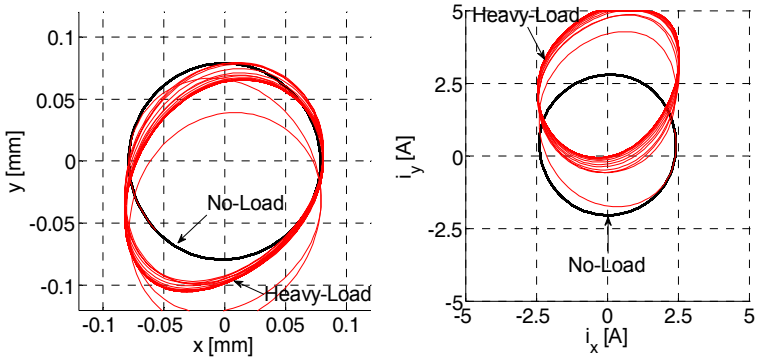

Fig. 17. Simulation-based unbalance responses for rotation test at 6000 rmp and 180 N load impact in the *y* axis – non-optimized AMBs

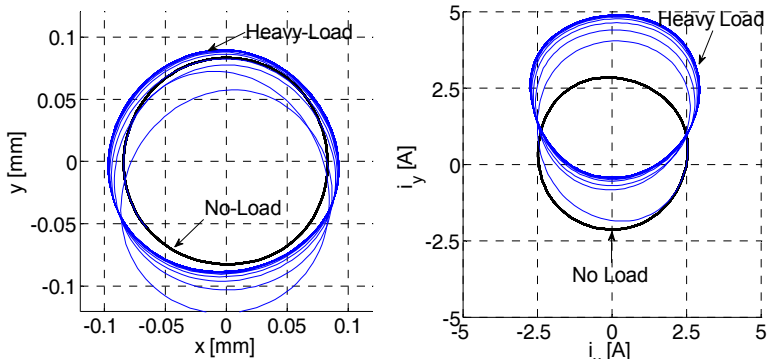

Fig. 18. Simulation-based unbalance responses for rotation test at 6000 rmp and 180 N load impact in the *y* axis – optimized AMBs

5. Conclusion

This work deals with non-linearities of radial force characteristic of AMBs. A linearized AMB model for one axis is presented first. It is used to define the current gain and position stiffness, parameters that are used for calculation of the controller settings. Next, FEM-based computations of the radial force are described. Based on the obtained results, a considerable radial force reduction is determined. It is caused by the magnetic non-linearities and cross-coupling effects. Therefore, the optimization of a radial AMB is proposed, where the aim is to find a such design, where a radial force characteristic is linear as much as possible over the entire operating range. A combination of differential evolution and FEM-based analysis is used, whereas the objective function is minimized by even 54%. Static and dynamic properties of the non-optimized and optimized AMB are evaluated in final section. The results presented here show that considerably lower variations of the current gain and position stiffness are achieved for the optimized AMB over the entire operating range, especially on its margins that are reached during heavy load unbalanced operation. Furthermore, a closed-loop damping and stiffness of an overall system are considerably higher with the optimized AMBs. Moreover, the operation with the higher load forces is also expected for the optimized radial AMB.

6. References

Antila, M., Lantto, E. & Arkkio, A. (1998). Determination of forces and linearized parameters of radial active magnetic bearings by finite element technique. *IEEE Transactions on Magnetics.* Vol. 34, No. 3, pp. 684–694.

Bleuer, H., Gähler, C., Herzog, R., Larsonneur, R., Mizuno, T., Siegwart, R., Woo, S.-J., (1994). Application of digital signal processors for industrial magnetic bearings. *IEEE Transactions on control systems technology.* Vol. 2, No. 4, pp. 278-289.

Carlson-Skalak, S., Maslen, E., & Teng, Y. (1999). Magnetic bearings actuator design using genetic alghoritms. *Journal of Engineering Design*. Vol. 10, No. 2, pp. 143–164.

Hameyer, K. & Belmans, R. (1999). *Numerical modelling and design of electrical machines and devices.* WIT Press, Suthampton.

ISMB12, (2010). The Twelfth International Symposium on Magnetic Bearings, Wuhan, China, http://ismb12.meeting.whut.edu.cn/

Knospe, C. R. & Collins, E. G. (1999). Introduction to the special issue on magnetic bearing control. *IEEE Transactions on control systems technology.* Vol. 4, No. 5, pp. 481–483.

Larsonneur, R. (1994). *Design and control of active magnetic bearing systems for high speed rotation,* Ph.D. dissertation, ETH Zürich.

Maslen, E. H. (1997). Radial bearing design, in *Short Course on Magnetic Bearings*, Lecture 7, Alexandria, Virginia.

Meeker, D. C. (1996). *Optimal solutions to the inverse problem in quadratic magnetic actuators,* Ph.D. dissertation, School of Engineering and Applied Science, University of Virginia.

Pahner, U., Mertens, R., DeGersem, H., Belmans, R. & Hameyer, K. (1998). A parametric finite element environment tuned for numerical optimization. *IEEE Transactions on Magnetics*. Vol. 34, No. 5, pp. 2936–2939.

Polajžer, B. (2002). *Design and analysis of an active magnetic bearing experimental system,* Ph.D. dissertation, University of Maribor, Faculty of Electrical Engineering and Computer Science, Maribor.

Polajžer, B., Štumberger, G., Ritonja, J. & Dolinar, D. (2008). Variations of active magnetic bearings linearized model parameters analyzed by finite element computation. *IEEE Transactions on Magnetics.* Vol. 44, No. 6, pp. 1534–1537.

Price, K., Storn, R., & Lampinen, J. (2005). *Differential evolution: a practical approach to global optimization*. Springer-Verlag: Berlin Heidelberg.

Rosner, C. H. (2001). Superconductivity: star technology for the 21st century. *IEEE Transactions on applied superconductivity.* Vol. 11, No. 1, pp. 39–48.

Schweitzer, G., Bleuler, H. & Traxler A. (1994). *Active magnetic bearings: Basics, properties and applications of active magnetic bearings*, Vdf Hochschulverlag AG an der ETH Zürich.

Štumberger, G., Dolinar, D., Pahner, U. & Hameyer, K. (2000). Optimization of radial active magnetic bearings using the finite element technique and the differential evolution algorithm. *IEEE Transactions on Magnetics.* Vol. 36, No. 4, pp. 1009–1013.

3

Magnetic levitation technique for active vibration control

Md. Emdadul Hoque and Takeshi Mizuno
Saitama University
Japan

1. Introduction

This chapter presents an application of zero-power controlled magnetic levitation for active vibration control. Vibration isolation are strongly required in the field of high-resolution measurement and micromanufacturing, for instance, in the submicron semiconductor chip manufacturing, scanning probe microscopy, holographic interferometry, cofocal optical imaging, etc. to obtain precise and repeatable results. The growing demand for tighter production tolerance and higher resolution leads to the stringent requirements in these research and industry environments. The microvibrations resulted from the tabletop and/or the ground vibration should be carefully eliminated from such sophisticated systems. The vibration control research has been advanced with passive and active techniques. Conventional passive technique uses spring and damper as isolator. They are widely used to support the investigated part to protect it from the severe ground vibration or from direct disturbance on the table by using soft and stiff suspensions, respectively (Haris & Piersol, 2002; Rivin, 2003). Soft suspensions can be used because they provide low resonance frequency of the isolation system and thus reduce the frequency band of vibration amplification. However, it leads to potential problem with static stability due to direct disturbance on the table, which can be solved by using stiff suspension. On the other hand, passive systems offer good high frequency vibration isolation with low isolator damping at the cost of vibration amplification at the fundamental resonance frequency. It can be solved by using high value of isolator damping. Therefore, the performance of passive isolators are limited, because various trade-offs are necessary when excitations with a wide frequency range are involved.

Active control technique can be introduced to resolve these drawbacks. Active control system has enhanced performances because it can adapt to changing environment (Fuller et al., 1997; Preumont, 2002; Karnopp, 1995). Although conventional active control system achieves high performance, it requires large amount of energy source to drive the actuators to produce active damping force (Benassi et al., 2004a & 2004b; Yoshioka et al., 2001; Preumont et al., 2002; Daley et al., 2006; Zhu et al., 2006; Sato & Trumper, 2002). Apart from this, most of the researches use high-performance sensors, such as servo-type accelerometer for detecting vibration signal, which are rather expensive. These are the difficulties to expand the application fields of active control technique.

The development and maintenance cost of vibration isolation system should be lowered in order to expand the application fields of active control. Considering the point of view, a vibration isolation system have been developed using an actively zero-power controlled magnetic levitation system (Hoque et al., 2006; Mizuno et al., 2007a; Hoque et al., 2010a). In the proposed system, eddy-current relative displacement sensors were used for displacement feedback. Moreover, the control current converges to zero for the zero-power control system. Therefore, the developed system becomes rather inexpensive than the conventional active systems.

An active zero-power controlled magnetic suspension is used in this chapter to realize negative stiffness by using a hybrid magnet consists of electromagnet and permanent magnets. Moreover, it can be noted that realizing negative stiffness can also be generalized by using linear actuator (voice coil motor) instead of hybrid magnet (Mizuno et al., 2007b). This control achieves the steady state in which the attractive force produced by the permanent magnets balances the weight of the suspended object, and the control current converges to zero. However, the conventional zero-power controller generates constant negative stiffness, which depends on the capacity of the permanent magnets. This is one of the bottlenecks in the field of application of zero-power control where the adjustment of stiffness is necessary. Therefore, this chapter will investigate on an improved zero-power controller that has capability to adjust negative stiffness. Apart from this, zero-power control has inherently nonlinear characteristics. However, compensation to zero-power control can solve such problems (Hoque et al., 2010b). Since there is no steady energy consumption for achieving stable levitation, it has been applied to space vehicles (Sabnis et al., 1975), to the magnetically levitated carrier system in clean rooms (Morishita et al., 1989) and to the vibration isolator (Mizuno et al., 2007a). Six-axis vibration isolation system can be developed as well using this technique (Hoque et al., 2010a).

In this chapter, an active vibration isolation system is developed using zero-power controlled magnetic levitation technology. The isolation system is fabricated by connecting a mechanical spring in series with a suspension of negative stiffness (see Section 4 for details). Middle tables are introduced in between the base and the isolation table.

In this context, the nomenclature on the vibration disturbances, compliance and transmissibility are discussed for better understanding. The underlying concept on vibration isolation using magnetic levitation technique, realization of zero-power, stiffness adjustment, nonlinear compensation of the maglev system are presented in detail. Some experimental results are presented for typical vibration isolation systems to demonstrate that the maglev technique can be implemented to develop vibration isolation system.

2. Vibration Suppression Terminology

2.1 Vibration Disturbances

The vibration disturbance sources are categorized into two groups. One is direct disturbance or tabletop vibration and another is ground or floor vibration.

Direct disturbance is defined by the vibrations that applies to the tabletop and generates deflection or deformation of the system. *Ground vibration* is defined by the detrimental vibrations that transmit from floor to the system through the suspension. It is worth noting that zero or low compliance for tabletop vibration and low transmissibility (less than unity) are ideal for designing a vibration isolation system.

Almost in every environment, from laboratory to industry, vibrational disturbance sources are common. In modern research or application arena, it is certainly necessary to conduct experiments or make measurements in a vibration-free environment. Think about a industry or laboratory where a number of energy sources exist simultaneously. Consider the silicon wafer photolithography system, a principal equipment in the semiconductor manufacturing process. It has a stage which moves in steps and causes disturbance on the table. It supports electric motors, that generates periodic disturbance. The floor also holds some rotating machines. Moreover, earthquake, movement of employees with trolley transmit seismic disturbance to the stage. Assume a laboratory measurement table in another case. The table supports some machine tools, and change in load on the table is a common phenomena. In addition, air compressor, vacuum pump, oscilloscope and dynamic signal analyzer with cooling fan rest on the floor. Some more potential energy souces are elevator mechanisms, air conditioning, rail and road transport, heat pumps that contribute to the vibrational background noise and that are coupled to the foundations and floors of the surrounding buildings. All the above sources of vibrations affect the system either directly on the table or transmit from the floor.

2.2 Compliance

Compliance is defined as the ratio of the linear or angular displacement to the magnitude of the applied static or constant force. Moreover, in case of a varying dynamic force or vibration, it can be defined as the ratio of the excited vibrational amplitude in any form of angular or translational displacement to the magnitude of the forcing vibration. It is the most extensively used transfer function for the vibrational response of an isolation table. Any deflection of the isolation table is demonstrated by the change in relative position of the components mounted on the table surface. Hence, if the isolation system has virtually zero or lower compliance (infinite stiffness) values, by definition , it is a better-quality table because the deflection of the surface on which fabricated parts are mounted is reduced. Compliance is measured in units of displacement per unit force, i.e., meters/Newton (m/N) and used to measure deflection at different frequencies.

The deformation of a body or structure in response to external payloads or forces is a common problem in engineering fields. These external disturbance forces may be static or dynamic. The development of an isolation table is a good example of this problem where such static and dynamic forces may exist. A static laod, such as that caused by a large, concentrated mass loaded or unloaded on the table, can cause the table to deform. A dynamic force, such as the periodic disturbance of a rotating motor placed on top of the table, or vibration induced from the building into the isolation table through its mounting points, can cause the table to oscillate and deform.

Assume the simplest model of conventional mass-spring-damper system as shown in Fig. 1(a), to understand compliance with only one degree-of-freedom system. Consider that a single frequency sinusoidal vibration applied to the system. From Newton's laws, the general equation of motion is given by

$$m\ddot{x} + c\dot{x} + kx = F_0 \sin \omega t \ , \tag{1}$$

where m : the mass of the isolated object, x : the displacement of the mass, c : the damping, k : the stiffness, F_0 : the maximum amplitude of the disturbance, ω : the rotational frequency of disturbance, and t : the time.

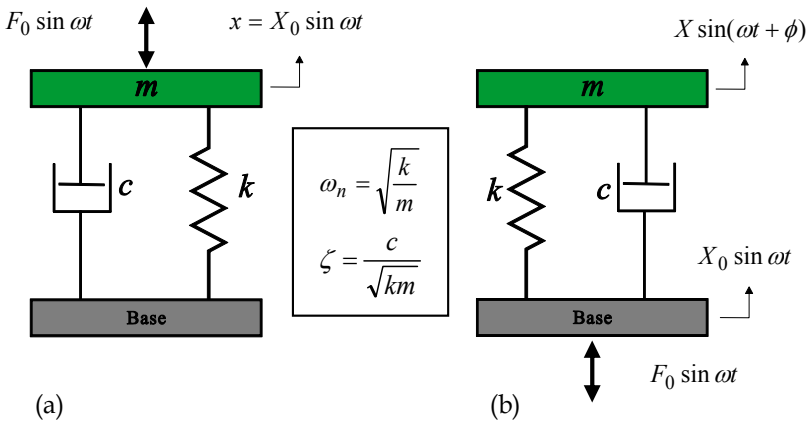

Fig. 1. Conventional mass-spring-damper vibration isolator under (a) direct disturbance (b) ground vibration.

The general expression for compliance of a system presented in Eq. (1) is given by

$$\text{Compliance} = \frac{x}{F} = \frac{1}{\sqrt{(k - m\omega^2)^2 + (c\omega)^2}}. \tag{2}$$

The compliance in Eq. (2) can be represented as

$$\text{Compliance} = \frac{x}{F} = \frac{1/k}{\sqrt{(1-(\omega/\omega_n)^2)^2 + 4\zeta^2(\omega/\omega_n)^2}}, \tag{3}$$

where ω_n : the natural frequency of the system and ζ : the damping ratio.

2.3 Transmissibility

Transmissibility is defined as the ratio of the dynamic output to the dynamic input, or in other words, the ratio of the amplitude of the transmitted vibration (or transmitted force) to that of the forcing vibration (or exciting force).

Vibration isolation or elimination of a system is a two-part problem. As discussed in Section 2.1, the tabletop of an isolation system is designed to have zero or minimal response to a disturbing force or vibration. This is itself not sufficient to ensure a vibration free working surface. Typically, the entire table system is subjected continually to vibrational impulses from the laboratory floor. These vibrations may be caused by large machinery within the building as discussed in Section 2.1 or even by wind or traffic-excited building resonances or earthquake.

The model shown in Fig. 1(a) is modified by applying ground vibration, as shown in Fig. 1(b). The absolute transmissibility, T of the system, in terms of vibrational displacement, is given by

$$\frac{X}{X_0} = \sqrt{\frac{1+4\zeta^2(\omega/\omega_n)^2}{(1-(\omega/\omega_n)^2)^2+4\zeta^2(\omega/\omega_n)^2}}\,. \tag{4a}$$

Similarly, the transmissibility can also be defined in terms of force. It can be defined as the ratio of the amplitude of force tranmitted (F) to the amplitude of exciting force (F0). Mathematically, the transmissibility in terms of force is given by

$$\frac{F}{F_0} = \sqrt{\frac{1+4\zeta^2(\omega/\omega_n)^2}{(1-(\omega/\omega_n)^2)^2+4\zeta^2(\omega/\omega_n)^2}}\,. \tag{4b}$$

3. Zero-Power Controlled Magnetic Levitation

3.1 Magnetic Suspension System

Since last few decades, an active magnetic levitation has been a viable choice for many industrial machines and devices as a non-contact, lubrication-free support (Schweitzer et al., 1994; Kim & Lee, 2006; Schweitzer & Maslen, 2009). It has become an essential machine element from high-speed rotating machines to the development of precision vibration isolation system. Magnetic suspension can be achieved by using electromagnet and/or permanent magnet. Electromagnet or permanent magnet in the magnetic suspension system causes flux to circulate in a magnetic circuit, and magnetic fields can be generated by moving charges or current. The attractive force of an electromagnet, F can be expressed approximately as (Schweitzer et al., 1994)

$$F = K\frac{I^2}{\delta^2}, \tag{5}$$

where K: attractive force coefficient for electromagnet, I: coil current, δ: mean gap between electromagnet and the suspended object.

Each variable is given by the sum of a fixed component, which determines its operating point and a variable component, such as

$$I = I_0 + i, \tag{6}$$

$$\delta = D_0 - x, \tag{7}$$

where I_0: bias current, i: coil current in the electromagnet, D_0: nominal gap, x: displacement of the suspended object from the equilibrium position.

3.2 Magnetic Suspension System with Hybrid Magnet

In order to reduce power consumption and continuous power supply, permanent magnets are employed in the suspension system to avoid providing bias current. The suspension system by using hybrid magnet, which consists of electromagnet and permanent magnet is shown in Fig. 2. The permanent magnet is used for the purpose of providing bias flux (Mizuno & Takemori, 2002). This control realizes the steady states in which the electromagnet coil current converges to zero and the attractive force produced by the permanent magnet balances the weight of the suspended object.

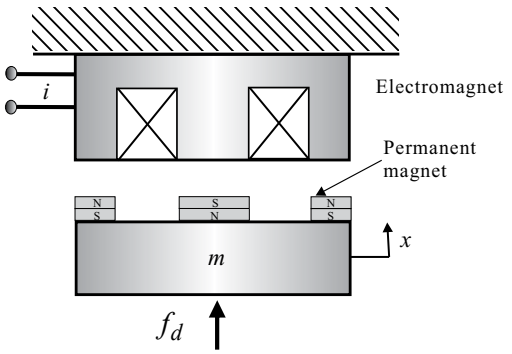

Fig. 2. Model of a zero-power controlled magnetic levitation

It is assumed that the permanent magnet is modeled as a constant-current (bias current) and a constant-gap electromagnet in the magnetic circuit for simplification in the following analysis. Attractive force of the electromagnet, F can be written as

$$F = K\frac{(I_0 + i)^2}{(D_0 - x)^2}, \tag{8}$$

where bias current, I_0 is modified to equivalent current in the steady state condition provided by the permanent magnet and nominal gap, D_0 is modified to the nominal air gap in the steady state condition including the height of the permanent magnet. Equation (8) can be transformed as

$$F = K\frac{I_0^2}{D_0^2}\left(1-\frac{x}{D_0}\right)^{-2}\left(1+\frac{i}{I_0}\right)^2. \tag{9}$$

Using Taylor principle, Eq. (9) can be expanded as

$$F = K\frac{I_0^2}{D_0^2}\left(1+2\frac{x}{D_0}+3\frac{x^2}{D_0^2}+4\frac{x^3}{D_0^3}+\ldots\right)\left(1+2\frac{i}{I_0}+\frac{i^2}{I_0^2}\right). \tag{10}$$

For zero-power control system, control current is very small, especially, in the phase approaches to steady-state condition and therefore, the higher-order terms are not considered. Equation (10) can then be written as

$$F = F_e + k_i i + k_s (x + p_2 x^2 + p_3 x^3 + ...) , \tag{11}$$

where

$$F_e = K \frac{I_0^2}{D_0^2} , \tag{12}$$

$$k_i = 2K \frac{I_0}{D_0^2} , \tag{13}$$

$$k_s = 2K \frac{I_0^2}{D_0^3} , \tag{14}$$

$$p_2 = \frac{3}{2D_0} , \tag{15}$$

$$p_3 = \frac{4}{2D_0^2} . \tag{16}$$

For zero-power control system, the control current of the electromagnet is converged to zero to satisfy the following equilibrium condition

$$F_e = mg , \tag{17}$$

and the equation of motion of the suspension system can be written as

$$m\ddot{x} = F - mg . \tag{18}$$

From Eqs. (11), (17) and (18),

$$m\ddot{x} = k_i i + k_s (x + p_2 x^2 + p_3 x^3 + ...) . \tag{19}$$

This is the fundamental equation for describing the motion of the suspended object.

3.3 Design of Zero-Power Controller

Negative stiffness is generated by actively controlled zero-power magnetic suspension. The basic model, controller and the characteristic of the zero-power control system is described below.

3.3.1 Model

A basic zero-power controller is designed for simplicity based on linearized equation of motions. It is assumed that the displacement of the suspended mass is very small and the

nonlinear terms are neglected. Hence the linearized motion equation from Eq. (19) can be written as

$$m\ddot{x} = k_i i + k_s x \ . \tag{20}$$

The suspended object with mass of m is assumed to move only in the vertical translational direction as shown by Fig. 2. The equation of motion is given by

$$m\ddot{x} = k_s x + k_i i + f_d \ , \tag{21}$$

where x : displacement of the suspended object, k_s : gap-force coefficient of the hybrid magnet, k_i : current-force coefficient of the hybrid magnet, i : control current, f_d : disturbance acting on the suspended object. The coefficients k_s and k_i are positive. When each Laplace-transform variable is denoted by its capital, and the initial values are assumed to be zero for simplicity, the transfer function representation of the dynamics described by Eq. (21) becomes

$$X(s) = \frac{1}{s^2 - a_0}(b_0 I(s) + d_0 W(s)), \tag{22}$$

where $a_0 = k_s / m, b_0 = k_i / m,$ and $d_0 = 1/m.$

3.3.2 Suspension with Negative Stiffness

Zero-power can be achieved either by feeding back the velocity of the suspended object or by introducing a minor feedback of the integral of current in the PD (proportional-derivative) control system (Mizuno & Takemori, 2002). Since PD control is a fundamental control law in magnetic suspension, zero-power control is realized from PD control in this work using the second approach. In the current controlled magnetic suspension system, PD control can be represented as

$$I(s) = -(p_d + p_v s)X(s), \tag{23}$$

where p_d : proportional feedback gain, p_v : derivative feedback gain. Figure 3 shows the block diagram of a current-controlled zero-power controller where a minor integral feedback of current is added to the proportional feedback of displacement.

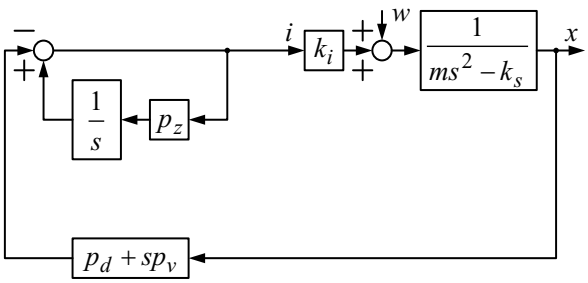

Fig. 3. Transfer function representation of the zero-power controller of the magnetic levitation system

The control current of zero-power controller is given by

$$I(s) = -(\frac{s}{s - p_z} p_d + p_v s) X(s), \tag{24}$$

where p_z: integral feedback in the minor current loop. From Eqs. (22) to (24), it can be written as

$$\frac{X(s)}{W(s)} = \frac{(s - p_z) d_0}{s^3 + (b_0 p_v - p_z) s^2 + (b_0 p_d - b_0 p_v p_z - a_0) s + a_0 p_z}, \tag{25}$$

$$\frac{I(s)}{W(s)} = \frac{-s(s p_v + p_d - p_v p_z) d_0}{s^3 + (b_0 p_v - p_z) s^2 + (b_0 p_d - b_0 p_v p_z - a_0) s + a_0 p_z}. \tag{26}$$

To estimate the stiffness for direct disturbance, the direct disturbance, $W(s)$ on the isolation table is considered to be stepwise, that is

$$W(s) = \frac{F_0}{s}, \ (F_0 : constant). \tag{27}$$

The steady displacement of the suspension, from Eqs. (25) and (27), is given by

$$\lim_{t \to \infty} x(t) = \lim_{s \to 0} sX(s) = -\frac{d_0}{a_0} F_0 = -\frac{F_0}{k_s}. \tag{28}$$

The negative sign in the right-hand side illustrates that the new equilibrium position is in the direction opposite to the applied force. It means that the system realizes negative stiffness. Assume that stiffness of any suspension is denoted by *k*. The stiffness of the zero-power controlled magnetic suspension is, therefore, negative and given by

$$k = -k_s. \tag{29}$$

3.3.3 Realization of Zero-Power

From Eqs. (26) and (27)

$$\lim_{t \to \infty} i(t) = \lim_{s \to 0} sI(s) = 0. \tag{30}$$

It indicates that control current, all the time, converges to zero in the zero-power control system for any load.

3.4 Stiffness Adjustment

The stiffness realized by zero-power control is constant, as shown in Eq. (29). However, it is necessary to adjust the stiffness of the magnetic levitation system in many applications, such as vibration isolation systems. There are two approaches to adjust stiffness of the zero-power control system. The first one is by adding a minor displacement feedback to the zero-power control current, and the other one is by adding a proportional feedback in the minor current feedback loop (Ishino et al., 2009). In this research, stiffness adjustment capability of zero-power control is realized by the first approach. Figure 4 shows the block diagram of the modified zero-power controller that is capable to adjust stiffness. The control current of the modified zero-power controller is given by

$$I'(s) = -(\frac{p_d s}{s - p_z} + \frac{p_v s^2}{s - p_z} + p_s)X(s), \tag{31}$$

where p_s : proportional displacement feedback gain across the zero-power controller.

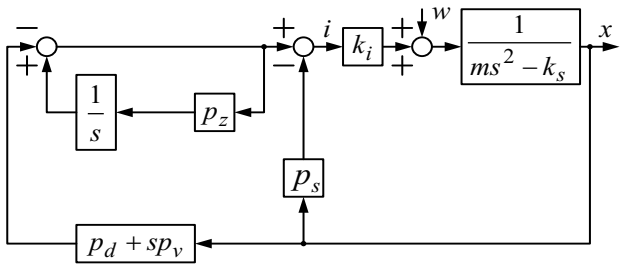

Fig. 4. Block diagram of the modified zero-power controller that can adjust stiffness

The transfer-function representation of the dynamics shown in Fig. 4 is given by

$$\frac{X(s)}{W(s)} = \frac{(s - p_z)d_0}{s^3 + (b_0 p_v - p_z)s^2 + (b_0 p_d + b_0 p_s - a_0)s + a_0 p_z - b_0 p_s p_z}. \tag{32}$$

From Eqs. (27) and (32), the steady displacement becomes

$$\lim_{t\to\infty} x(t) = \lim_{s\to 0} sX(s) = -\frac{d_0 p_z}{a_0 p_z - b_0 p_s p_z} F_0 = -\frac{F_0}{k_s - k_i p_s} \tag{33}$$

Therefore, the stiffness of the modified system becomes

$$k = -k_s + k_i p_s. \tag{34}$$

It indicates that the stiffness can be increased or decreased by changing the feedback gain p_s .

3.5 Nonlinear Compensation of Zero-Power Controller

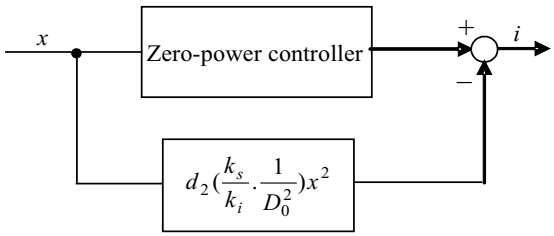

Fig. 5. Block diagram of the nonlinear compensator of the zero-power controlled magnetic levitation

It is shown that the zero-power control can generate negative stiffness. The control current of the zero-power controlled magnetic suspension system is converged to zero for any added mass. To counterbalance the added force due to the mass, the stable position of the suspended object is changed. Due to the air gap change between permanent magnet and the object, the magnetic force is also changed, and hence, the negative stiffness generated by this system varies as well according to the gap (see Eq. (14)). To compensate the nonlinearity of the basic zero-power control system, the first nonlinear terms of Eq. (19) is considered and added to the basic system. From Eq. (19), the control current can be expressed as

$$i = i_{ZP} - d_2(\frac{k_s}{k_i}.\frac{1}{D_0^2})x^2 , \tag{35}$$

where d_2 : the nonlinear control gain and, i_{zp} : the current in the zero-power controller, k_s , k_i and D_0 are constant for the system. The square of the displacement (x^2) is fed back to the normal zero-power controller. The block diagram of the nonlinear controller arrangement is shown in Fig. 5. The air gap between the permanent magnet and the suspended object can be changed in order to choose a suitable operating point.
It is worth noting that the nonlinear compensator and the stiffness adjustment controller can be used simultaneously without instability. Moreover, performance of the nonlinear compensation could be improved furthermore if the second and third nonlinear terms and so on are considered together.

4. Vibration Suppression Using Zero-Power Controlled Magnetic Levitation

4.1 Theory of Vibration Control

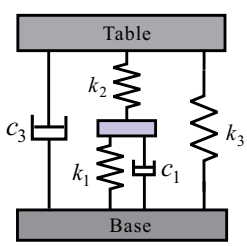

Fig. 6. A model of vibration isolator that can suppress both tabletop and ground vibrations

The vibration isolation system is developed using magnetic levitation technique in such a way that it can behave as a suspension of virtually zero compliance or infinite stiffness for direct disturbing forces and a suspension with low stiffness for floor vibration. Infinite stiffness can be realized by connecting a mechanical spring in series with a magnetic spring that has negative stiffness (Mizuno, 2001; Mizuno et al., 2007a & Hoque et al., 2006). When two springs with spring constants of k_1 and k_2 are connected in series, the total stiffness k_c is given by

$$k_c = \frac{k_1 k_2}{k_1 + k_2}. \tag{36}$$

The above basic system has been modified by introducing a secondary suspension to avoid some limitations for system design and supporting heavy payloads (Mizuno, et al., 2007a & Hoque, et al., 2010a). The concept is demonstrated in Fig. 6. A passive suspension (k_3 , c_3) is added in parallel with the serial connection of positive and negative springs. The total stiffness $\widetilde{k}_c$ is given by

$$\widetilde{k}_c = \frac{k_1 k_2}{k_1 + k_2} + k_3. \tag{37}$$

However, if one of the springs has negative stiffness that satisfies

$$k_1 = -k_2, \tag{38}$$

the resultant stiffness becomes infinite for both the case in Eqs. (36) and (37) for any finite value of k_3, that is

$$\left|\widetilde{k}_c\right| = \infty. \tag{39}$$

Equation (39) shows that the system may have infinite stiffness against direct disturbance to the system. Therefore, the system in Fig. 6 shows virtually zero compliance when Eq. (38) is satisfied. On the other hand, if low stiffness of mechanical springs for system (k_1 , k_3) are used, it can maintain good ground vibration isolation performance as well.

4.2 Typical Applications of Vibration Suppression

In this section, typical vibration isolation systems using zero-power controlled magnetic levitation are presented, which were developed based on the principle discussed in Eq. (37). The isolation system consists mainly of two suspensions with three platforms- base, middle table and isolation table. The lower suspension between base and middle table is of positive stiffness and the upper suspension between middle table and base is of negative stiffness realized by zero-power control. A passive suspension directly between base and isolation table acts as weight support mechanism.

A typical single-axis and a typical six-axis vibration isolation apparatuses are demonstrated in Fig. 7. The single-axis apparatus (Fig. 7(a)) consisted of a circular base, a circular middle table and a circular isolation table. The height, diameter and weight of the system were 300mm, 200mm and 20 kg, respectively. The positive stiffness in the lower part was realized by three mechanical springs and an electromagnet. To reduce coil current in the electromagnet, four permanent magnets (15mm×2mm) were used. The permanent magnets are made of Neodymium-Iron-Boron (NdFeB). The stiffness of each coil springs was 3.9

N/mm. The electromagnet coil had 180-turns and 1.3Ω resistance. The wire diameter of the coil was 0.6 mm. The relative displacement of the base to middle table was measured by an eddy-current displacement sensor, provided by Swiss-made Baumer electric. The negative stiffness suspension in the upper part was achieved by a hybrid magnet consisted of an electromagnet that was fixed to the middle table, and six permanent magnets attached to the electromagnet target on the isolation table. Another displacement sensor was used to measure the relative displacement between middle table to isolation table. The isolation table was also supported by three coil springs as weight support mechanism, and the stiffness of the each spring was 2.35 N/mm.

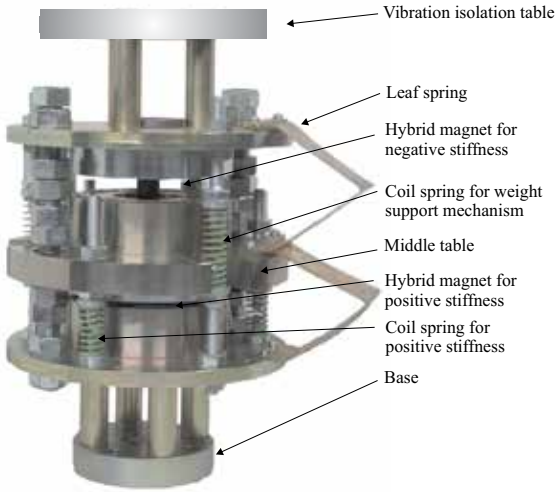

(a)

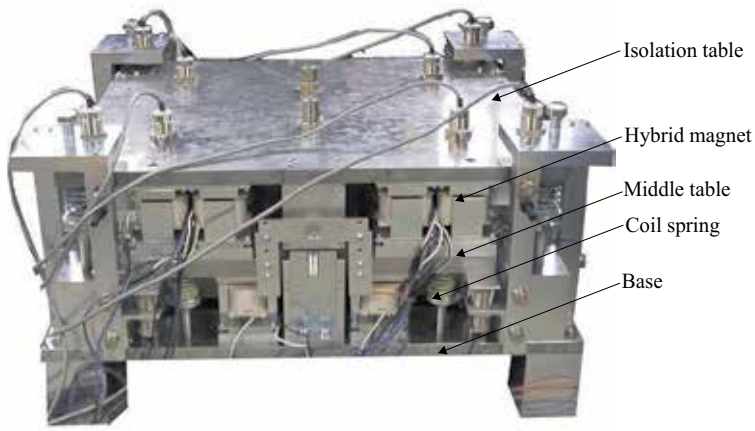

(b)

Fig. 7. Typical applications of zero-power controlled magnetic levitation for active vibration control (a) single-degree-of-freedom system (b) six-degree-of-freedom system

The six-axis vibration isolation system with magnetic levitation technology is shown in Fig. 7(b) (Hoque, et al., 2010a). It consisted of a rectangular isolation table, a middle table and base. A positive stiffness suspension realized by electromagnet and normal springs was used between the base and the middle table. On the other hand, a negative stiffness suspension generated by hybrid magnets was used between the middle table and the isolation table. The height, length, width and mass of the apparatus were 300 mm, 740 mm, 590 mm and 400 kg, respectively. The isolation and middle tables weighed 88 kg and 158 kg, respectively. The isolation table had six-degree-of-freedom motions in the x, y, z, roll, pitch and yaw directions.

The base was equipped with four pairs of coil springs and electromagnets to support the middle table in the vertical direction and six pairs of coil springs and electromagnets (two pairs in the x-direction and four pairs in the y-direction) in the horizontal directions. The middle table was equipped with four sets of hybrid magnets to levitate and control the motions of the isolation table in the vertical direction and six sets of hybrid magnets (two sets in the x-direction and four sets in the y-direction) to control the motions of the table in the horizontal directions. The isolation table was also supported by four coil springs in the vertical direction and six coil springs (two in the x-direction and four in the y-direction) in the horizontal directions as weight support mechanism. Each set of hybrid magnet for zero-power suspension consisted of five square-shaped permanent magnets (20 mm×20 mm×2 mm) and five 585-turn electromagnets. The spring constant of each normal spring was 12.1 N/mm and that of weight support spring was 25.5 N/mm. There was flexibility to change the position of the weight support springs both in the vertical and horizontal directions to make it compatible for designing stable magnetic suspension system using zero-power control. The relative displacements of the isolation table to the middle table and those of the middle table to the base were detected by eight eddy-current displacement sensors attached to the corners of the isolation table and the base.

A DSP-based digital controller (DS1103) was used for the implementation of the designed control algorithms by simulink in Matlab. The sampling rate was 10 kHz.

4.3 Experimental Demonstrations

Several experiments have been conducted to verify the aforesaid theoretical analysis. The nonlinear compensation of zero-power controlled magnetic levitation, stiffness adjustment of the levitation system are confirmed initially. Then the characteristics of the developed isolation systems are measured in terms of compliance and transmissibility.

4.3.1 Nonlinear Compensation of Magnetic Levitation System

First of all, zero-power control was realized between the isolation table and the middle table for stable levitation. Static characteristic of the zero-power controlled magnetic levitation was measured as shown in Fig. 8 when the payloads were increased to produce static direct disturbances on the table in the vertical direction.

In this case, the middle table was fixed and the table was levitated by zero-power control. The result presents the load-stiffness characteristic of the zero-power control system. The figure without nonlinear compensation indicates that there was a wide variation of stiffness when the downward load force changed. For the uniform load increment, the change of gap was not equal due to the nonlinear magnetic force. Therefore, the negative stiffness generated from zero-power control was nonlinear which may severely affect the vibration isolation system.

To overcome the above problem, the nonlinear compensator was introduced in parallel with the zero-power control system. The nonlinear control gain (d_2) was chosen by trial and error method. The gap (D_0) between the table and the electromagnet was 5.1 mm after stable levitation by zero-power control. The value of k_s and k_i were determined from the system characteristics. The load-stiffness characteristic using nonlinear compensation is also shown in the figure. It is obvious from the figure that the linearity error was reduced when control gain (d_2) was increased. For $d_2 = 55$, the linearity error was very low and the stiffness generated from the system was approximately constant. This result shows the potential to improve the static response performance of the isolation table to direct disturbance.

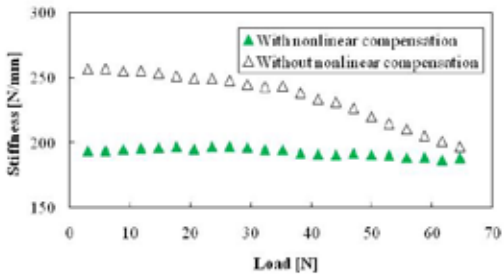

Fig. 8. Nonlinear compensation of the conventional zero-power controlled magnetic levitation system

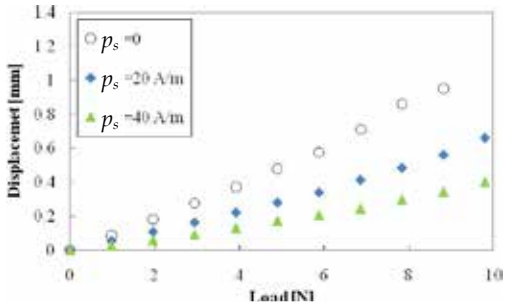

Fig. 9. Load-displacement characteristics of the modified zero-power controlled magnetic levitation system

4.3.2 Stiffness Adjustment of Zero-Power Controlled Magnetic Levitation

The experiments have been carried out to measure the performances of the modified zero-power controller. Figure 9 shows the load-displacement characteristics of the system with the improved zero-power controller (Fig. 4). When the proportional feedback gain, $p_s = 0$, it can be considered as a conventional zero-power controller (Fig. 3). The result shows that when the payloads were put on the suspended object, the table moved in the direction opposite to the applied load, and the gap was widened. It indicates that the zero-power control realized negative displacement, and hence its stiffness is negative, as described by Eqs. (28) and (29). The conventional zero-power controller ($p_s = 0$) realized fixed negative stiffness of magnitude -9.2 N/mm. When the proportional feedback gain, p_s was changed, the stiffness also gradually increased. When $p_s = 40$ A/m, negative stiffness was increased to -21.5 N/mm. It confirms that proportional feedback gain, p_s can change the stiffness of the zero-power controller, as explained in Eq. (34).

4.3.3 Experimental Results with Vibration Isolation System

Further experiments were conducted with the linearized zero-power controller with the vibration isolation system, as shown in Fig. 10. In this case, the positive and negative stiffness springs were, then, adjusted to satisfy Eq. (38). The stiffness could either be adjusted in the positive or negative stiffness part. In the former, PD control could be used in the electromagnets that were employed in parallel with the coil springs. The latter technique was presented in Section 4.3.2. For better performance, the latter was adopted in this work.

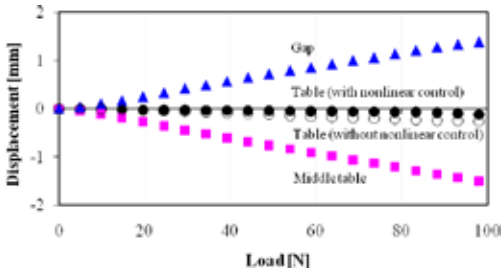

Fig. 10. Static characteristics of the isolation table with and without nonlinear control

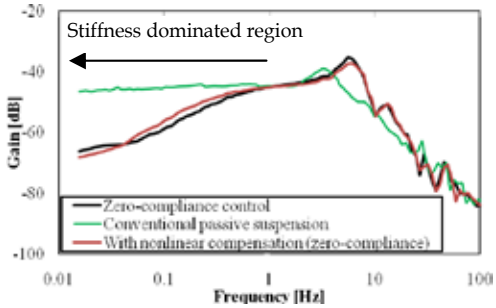

Fig. 11. Dynamic characteristics of the isolation table in the vertical direction

Figure 10 demonstrates the performance improvement of the controller for static response to direct disturbance. The displacements of the isolation table and middle table were plotted against disturbing forces produced by payload in the vertical direction. It is clear that zero-compliance to direct disturbance was realized up to 100 N payloads with nonlinear controller (d_2=55). The stiffness of the isolation system was increased to 960 N/mm which was approximately 2.8 times more than that of without nonlinear control. The figure illustrates significant improvement in rejecting on-board-generated disturbances.

The dynamic performance of the isolation table was measured in the vertical direction as shown in Fig. 11. In this case, the isolation table was excited to produce sinusoidal disturbance force by two voice coil motors which were attached to the base and can generate force in the Z-direction. The displacement of the table was measured by gap sensors and the data was captured by a dynamic signal analyzer. It is found from the figure that high stiffness, that means virtually zero-compliance, was realized at low frequency region (-66 dB[mm/N] at 0.015 Hz). It also demonstrates that direct disturbance rejection performance was not worsened even nonlinear zero-power control was introduced.
Finally a comparative study of the disturbance suppression performance was conducted with zero-compliance control and conventional passive suspension technique as shown in the figure. The experiment was carried out with same lower suspension for ground vibration isolation. First, the isolation table was suspended by positive suspension (conventional spring-damper) and frequency response to direct disturbance was measured. The stiffness dominated region is marked in the figure, and it is seen from the figure that the displacement of the isolation table was almost same below 1 Hz (approximately -46 dB). However, when the isolation table was suspended by zero-compliance control satisfying Eqs. (38) and (39), displacement of the table was abruptly reduced at the low frequency region below 1 Hz (-66 dB at 0.015 Hz). It is confirmed from the figure that the developed zero-compliance system had better direct disturbance rejection performance over the conventional passive suspension even both the systems used similar vibration isolation performances.

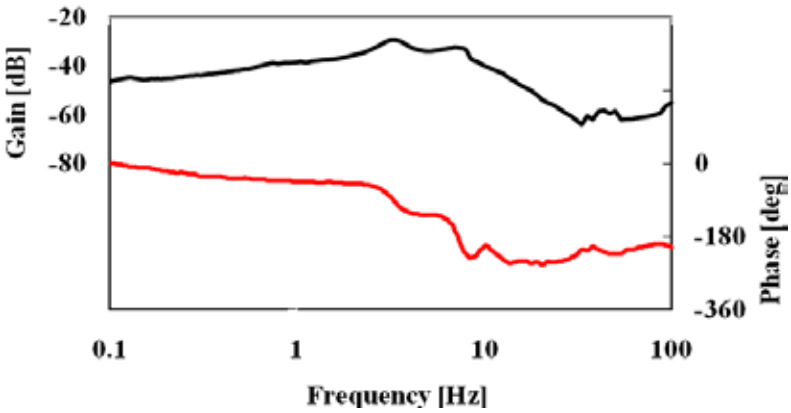

Fig. 12. Dynamic characteristics of the isolation table in the vertical direction.

The characteristics of the isolation table were further investigated by measuring the response of the table to direct disturbance in the horizontal directions as shown in Fig. 12. In this case, four voice coil motors were used to excite the isolation table along the horizontal direction. The results show the dynamic response of the isolation table when the table was excited along yaw mode. The response of the table to direct dynamic disturbance was captured by dynamic signal analyzer. The results justify that the displacements of the table to direct disturbance in the horizontal rotational motions were also low at the low frequency regions. The results confirmed that the isolation table was realized high stiffness against disturbing forces in the motion associated with horizontal direction.

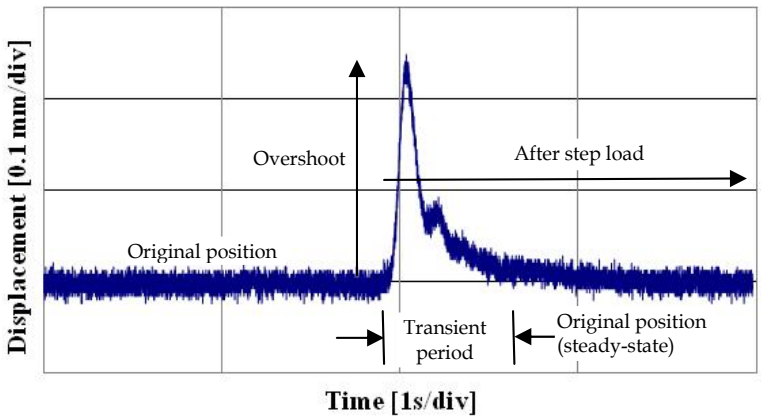

Fig. 13. Step response of the isolation table with magnetic levitation technology

The step response of the isolation table is shown in Fig. 13. In this experiment, a stepwise disturbance was generated by suddenly removing a certain amount of load from the table and the response was measured. The results showed that the table moved upward in the direction of load removal and returned to the original position (steady-state) after certain period. However, there was a reverse action in case of step wise disturbance. Therefore, a

peak was appeared due to the response of the step load. This unpleasant response might hamper the objective function of many advanced systems. It can be noted that a feedforward controller can be added in combination with zero-power control to overcome this problem.

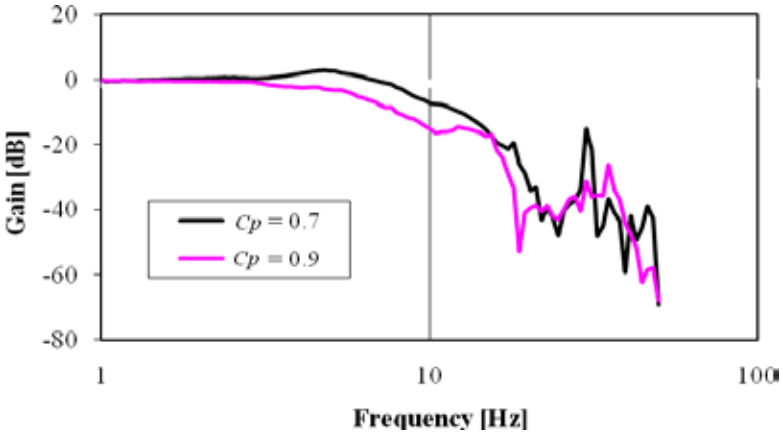

Fig. 14. Transmissibility characteristics of the isolation table.

Figure 14 shows the absolute transmissibility of the isolation table from the base of the developed system. In this case, the base of the system was sinusoidally excited in the vertical direction by a high-powered pneumatic actuator attached to the base, and the displacement transfer function (transmissibility) of the isolation table was measured from the base. The base displacement in the vertical direction was considered as input, and the output signal was the displacement of the isolation table. The damping coefficient (c_p) between the base and the middle table played important role to suppress the resonance peak. The figure shows that the resonant peak was almost suppressed when c_p was chosen as 0.9. It is clear from the figure that the developed system can effectively isolate the floor vibration that transmitted through the suspensions, such as active-passive positive suspensions and active zero-power controlled magnetic levitation.

5. Conclusions

A zero-power controlled magnetic levitation system has been presented in this chapter. The unique characteristic of the zero-power control system is that it can generate negative stiffness with zero control current in the steady-state which is realized in this chapter. The detail characteristics of the levitation system are investigated. Moreover, two major contributions, the stiffness adjustment and nonlinear compensation of the suspension system have been introduced elaborately. Often, there is a challenge for the vibration isolator designer to tackle both direct disturbance and ground vibration simultaneously with minimum system development and maintenance costs. Taking account of the point of view, typical applications of active vibration isolation using zero-power controlled magnetic levitation has been presented. The vibration isolation system is capable to suppress the effect of tabletop vibration as well as to isolate ground vibration. Some experimental demonstrations are presented that verifies the feasibility of its application in many industries and space related instruments. Moreover, it can be noted that a feedforward controller in combination with the zero-power controller can be used to improve the performance of the isolator to suppress direct disturbances.

6. Acknowledgment

The authors gratefully acknowledge the financial support made available from the Japan Society for the Promotion of Science as a Grant-in-Aid for scientific research (Grant no. 20.08380) for the foreign researchers and the Ministry of Education, Culture, Sports, Science and Technology of Japan, as a Grant-in-Aid for Scientific Research (B).

7. References

Benassi, L. ; Elliot, S. J. & Gardonio, P. (2004a). Active vibration isolation using an inertial actuator with local force feedback control, *Journal of Sound and Vibration*, Vol. 276, No. 3, pp. 157-179

Benassi, L. & Elliot, S. J. (2004b). Active vibration isolation using an inertial actuator with local displacement feedback control, *Journal of Sound and Vibration*, Vol. 278, No. 4-5, pp. 705-724

Daley, S. ; Hatonen, J. & Owens, D. H. (2006). Active vibration isolation in a "smart spring" mount using a repetitive control approach, *Control Engineering Practice*, Vol. 14, pp. 991-997.

Fuller, C. R. ; Elliott, S. J. & Nelson, P. A. (1997). *Active Control of Vibration*, Academic Press, ISBN 0-12-269440-6, New York, USA

Harris, C. M. & Piersol, A. G. (2002). *Shock and Vibration Handbook*, McGraw Hill, Fifth Ed., ISBN 0-07-137081-1, New York, USA

Hoque, M. E. ; Takasaki, M. ; Ishino, Y. & Mizuno, T. (2006). Development of a three-axis active vibration isolator using zero-power control, *IEEE/ASME Transactions on Mechatronics*, Vol. 11, No. 4, pp. 462-470

Hoque, M. E. ; Mizuno, T. ; Ishino, Y. & Takasaki, M. (2010a), A six-axis hybrid vibration isolation system using active zero-power control supported by passive support mechanism, *Journal of Sound and Vibration*, Vol. 329, No. 17, pp. 3417-3430

Hoque, M. E. ; Mizuno, T. ; Kishita, D. ; Takasaki, M. & Ishino, Y. (2010b). Development of an Active Vibration Isolation System Using Linearized Zero-Power Control with Weight Support Springs, *ASME Journal of Vibration and Acoustics*, Vol. 132, No. 4, pp. 041006-1/9

Ishino, Y. ; Mizuno, T. & Takasaki, M. (2009). Stiffness Control of Magnetic Suspension by Local Feedback, Proceedings of the European Control Conference 2009, pp. 3881-3886, Budapest, Hungary, 23-26 August, 2009

Karnopp, D. (1995). Active and semi-active vibration isolation, *ASME Journal of Mechanical Design*, Vol. 117, pp. 177-185

Kim, H. Y. & Lee, C. W. (2006). Design and control of Active Magnetic Bearing System With Lorentz Force-Type Axial Actuator, *Mechatronics*, vol. 16, pp. 13–20

Mizuno, T. (2001). Proposal of a Vibration Isolation System Using Zero-Power Magnetic Suspension, Proceedings of the Asia Pacific Vibration Conference 2001, pp. 423-427, Hangzhau, China

Mizuno, T. & Takemori, Y. (2002). A transfer-function approach to the analysis and design of zero-power controllers for magnetic suspension system, *Electrical Engineering in Japan*, Vol. 141, No. 2, pp. 933-940

Mizuno, T. ; Takasaki, M. ; Kishita, D. & Hirakawa, K. (2007a). Vibration isolation system combining zero-power magnetic suspension with springs, *Control Engineering Practice*, Vol. 15, No. 2, pp. 187-196

Mizuno, T. ; Furushima, T. ; Ishino, Y. & Takasaki, M. (2007b). General Forms of Controller Realizing Negative Stiffness, Proceedings of the SICE Annual Conference 2007, pp. 2995-3000, Kagawa University, Japan, 17-20 September, 2007

Morishita, M. ; Azukizawa, T. ; Kanda, S. ; Tamura, N. & Yokoyama, T. (1989). A new maglev system for magnetically levitated carrier system, *IEEE Transaction on Vehicular Technology*, Vol. 38, No. 4, pp. 230-236

Platus, D. L. (1991). Negative-stiffness-mechanism vibration isolation system, Proceedings of the SPIE, Vibration Control in Microelectronics, Optics, and Metrology, Vol. 1619, pp. 44-54

Preumont, A. (2002). *Vibration Control of Active Structures, An Introduction*, Kluwer, Second ed., ISBN 1-4020-0496-6, Dordrecht

Preumont, A. ; Francois, A. ; Bossens, F. & Hanieh, A. A. (2002). Force feedback versus acceleration feedback in active vibration isolation, *Journal of Sound and Vibration*, Vol. 257, No. 4, pp. 605-613

Rivin, E. I. (2003). *Passive Vibration Isolation*, ASME Press, ISBN: 0-7918-0187-X, New York, USA

Sabnis, A. V. ; Dendy, J. B. & Schmitt, F. M. (1975). Magnetically suspended large momentum wheel, *Journal of Spacecraft and Rockets*, Vol. 12, pp. 420-427

Sato, T. & Trumper, D. L. (2002). A novel single degree-of-freedom active vibration isolation system, Proceedings of the 8th International Symposium on Magnetic Bearing, pp. 193-198, Japan, August 26-28, 2002

Schweitzer, G. ; Bleuler, H. & Traxler, A. (1994). *Active Magnetic Bearings*, vdf Hochschulverlag AG an der ETH Zurich, Zurich, Switzerlannd

Schweitzer, G. & Maslen, E. H. (2009). *Magnetic Bearings- Theory, Design, and Application to Rotating Machinery*, ISBN : 978-3-642-00496-4, Springer, Germany

Yoshioka, H. ; Takahashi, Y. ; Katayama, K. ; Imazawa, T. & Murai, N. (2001). An active microvibration isolation system for hi-tech manufacturing facilities, *ASME Journal of Vibration and Acoustics*, Vol. 123, pp. 269-275

Zhu, W. H. ; Tryggvason, B. & Piedboeuf, J. C. (2006). On active acceleration control of vibration isolation systems, *Control Engineering Practice*, Vol. 14, No. 8, pp. 863-873

4

Salient pole permanent magnet axial-gap self-bearing motor

Quang-Dich Nguyen and Satoshi Ueno
Ritsumeikan University
Japan

1. Introduction

Recently, active magnetic-bearing motors have been designed to overcome the limitations of the conventional mechanical-bearing motors. Magnetic-bearing motors can work in all environments without lubrication and do not cause contamination; further, they can run at very high speeds. Therefore, they are very valuable machines with a number of novel features, and with a vast range of diverse applications (Dussaux, 1990).

The conventional magnetic-bearing motor usually has a rotary motor installed between two radial magnetic bearings, or a mechanical combination of a rotary motor and a radial magnetic bearing (The mechanically combined magnetic bearing motor usually has n-pole motor windings and n±2-pole suspension windings), as shown in Figs. 1 and 2 (Okada et al., 1996), (Oshima et al., 1996 a,b), (Zhaohui & Stephens, 2005), (Chiba et al., 2005). The radial magnetic bearings create radial levitation forces for rotor, while an axial magnetic bearing produces a thrust force to keep the rotor in the correct axial position relative to the stator. However, these magnetic-bearing motors are large, heavy, and complex in control and structure, which cause problems in applications that have limit space. Thus, a simpler and smaller construction and a less complex control system are desirable.

An axial magnetic bearing is composed of a rotary disc fixed on a rotary shaft and electromagnets arranged on both sides of the disc at a proper minute distance. This structure is similar to that of an axial-flux AC motor (Aydin et al., 2006), (Marignetti et al., 2008). Based on this, Satoshi Ueno has introduced an electrically combined motor-bearing which is shown in Fig. 3, in which the stator has only three-phase windings; however it can simultaneously provide non-contact levitation and rotation (Ueno & Okada, 1999), (Ueno & Okada, 2000). This motor is then called an axial-gap self-bearing motor (AGBM) to imply that the motor has self levitation function. Obviously, it is simpler in structure and control since hardware components can be reduced.

The AGBM can be realized as an induction motor (IM) (Ueno & Okada, 1999), or a permanent magnet (PM) motor (Ueno & Okada, 2000), (Okada et al., 2005), (Horz et al., 2006), (Nguyen & Ueno, 2009 a,b). The PM motor is given special attention, because of its high power factor, high efficiency, and simplicity in production.

In this chapter, the mathematical model of the salient 2-pole AGBM with double stators is introduced and analyzed (sandwich type). A closed loop vector control method for the axial position and the speed is developed in the way of eliminating the influence of the reluctance

torque. The vector control method for the AGBM drive is based on the reference frame theory, where the direct axis current i_d is used for controlling the axial force and the quadrate axis current i_q is used for controlling the rotating torque. The proposed control method is initially utilized for the salient AGBM ($L_{sd} < L_{sq}$), however it can be used for non-salient AGBM ($L_{sd} = L_{sq}$), too.

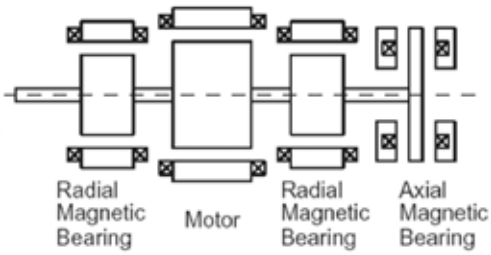

Fig. 1. Structure of conventional magnetic-bearing motor

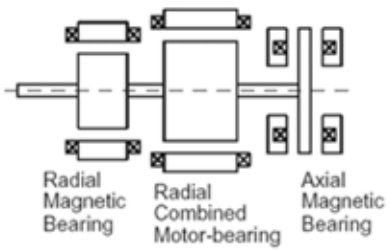

Fig. 2. Structure of radial-combined magnetic-bearing motor

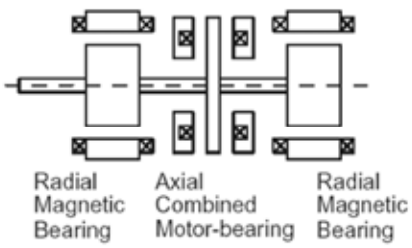

Fig. 3. Structure of axial-gap self-bearing motor

2. Mathematical Model

Per-phase equivalent circuits have been widely used in steady-state analysis of the AC machines. However, they are not appropriate to predict the dynamic performance of the motor. For vector control, a dynamic model of the motor is necessary. The analysis of three-phase motor is based on the reference frame theory. Using this technique, the dynamic equations of the AC motor are simplified and become similar to those of the DC motor.

The structure of an axial gap self-bearing motor is illustrated in Fig. 4. It consists of a disc rotor and two stators, which is arranged in sandwich type. The radial motions x, y, θ_x, and θ_y of the rotor are constrained by two radial magnetic bearings such as the repulsive bearing

shown. Only rotational motion and translation along the z axis are considered. The motor has two degrees of freedom (2 DOFs).

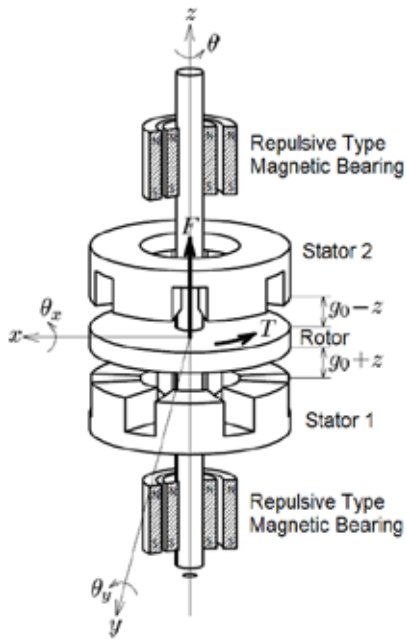

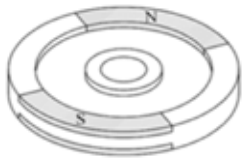

Salient pole rotor

Fig. 4. Detail structure and coordinates of the AGBM

The rotor is a flat disc with PMs inserted on both faces of the disc to create a salient-pole rotor. Two stators, one in each rotor side, have three-phase windings that generate rotating magnetic fluxes in the air gap. These produce motoring torques T_1 and T_2 on the rotor and generate attractive forces F_1 and F_2 between the rotor and the stators. The total motoring torque T is the sum of these torques, and the axial force F is the difference of the two attractive forces.

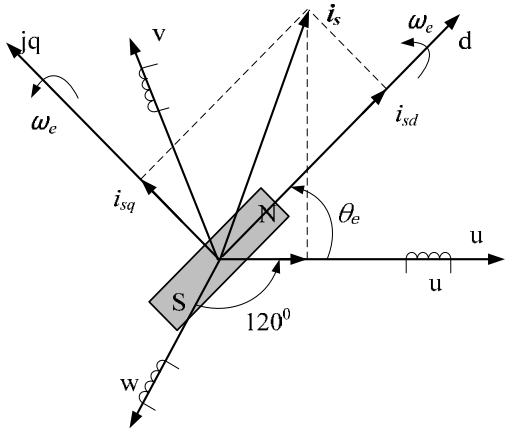

Fig. 5. Define of coordinates

To obtain a mathematical model of the AGBM, the axial force F_s and motoring torque T_s are first calculated for one stator. Similar to the non-salient AGBM, the mathematical model of the salient AGBM is presented in a rotor-field-oriented reference frame or so-called d, q coordinates, as indicated in Fig. 5. The d axis is aligned with the center lines of the permanent magnets and the q axis between the magnets. The axes u, v, and w indicate the direction of the flux produced by the corresponding phase windings. The phase difference between the u axis and the d axis is the electrical angular position θ_e of the rotor flux vector.

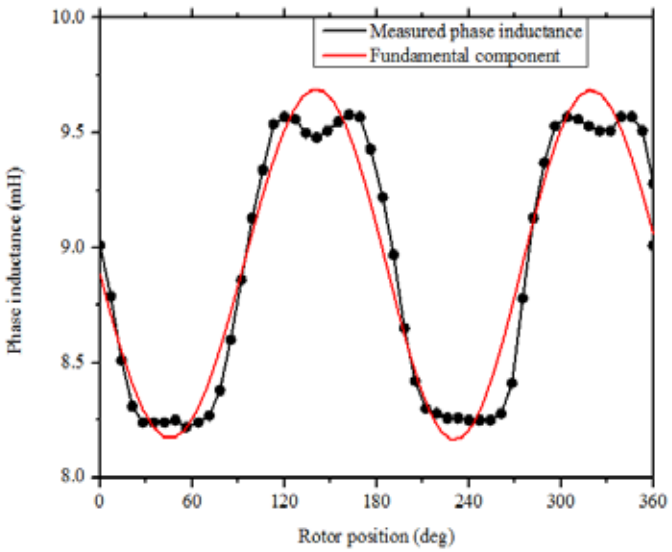

Fig. 6. Relation between phase inductance and rotor position

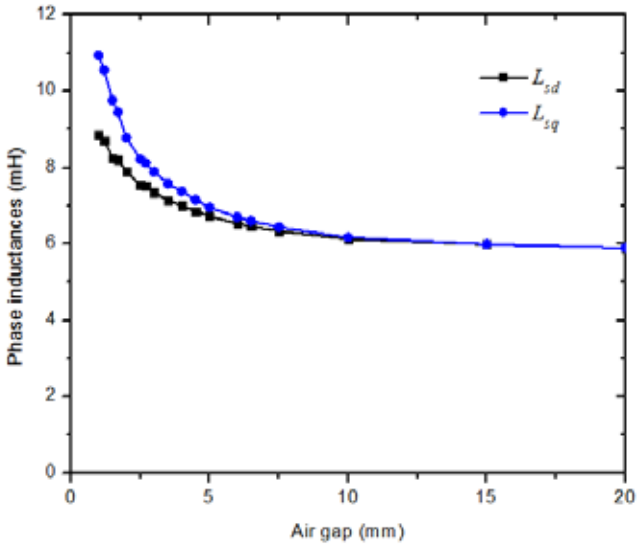

Fig. 7. Relation between phase inductance and air gap

Since the PM with unity permeability is used, the rotor is a salience; therefore the self-phase inductance of the stator is dependent on the rotor angular position, which means that the d-axis inductance is different from q-axis inductance. Furthermore, the self-phase inductance is a function of the air gap g between the rotor and the stator. The relation between self-phase inductance and rotor position as well as air gap is illustrated in Fig. 6 and 7. Obviously, the self-phase inductance is inversely proportional to the air gap, so the d- and q-axis phase inductance of the stator windings can be derived as (Fitzgerald, 1992)

$$\begin{cases} L_{sd} = \dfrac{3L'_{sd0}}{2g} + L_{sl} \\ L_{sq} = \dfrac{3L'_{sq0}}{2g} + L_{sl} \end{cases} \tag{1}$$

where, L'_{sd0}, L'_{sq0} are the d- and q-axis magnetizing inductances multiplied by the air gap length. They can be determined by calculating the motor parameters or measuring the phase inductance. L_{sl} is the leakage inductance. It can be estimated from the analysis of the measured phase inductance. By using the power invariant transformation method, the components of the stator voltage and the flux of the AGBM in the d,q coordinates can be expressed in the following equations:

$$\begin{cases} u_{sd} = R_s i_{sd} + L_{sd} \dfrac{di_{sd}}{dt} - \omega_e L_{sq} i_{sq} \\ u_{sq} = R_s i_{sq} + L_{sq} \dfrac{di_{sq}}{dt} + \omega_e L_{sd} i_{sd} + \omega_e \lambda_m \\ \lambda_{sd} = L_{sd} i_{sd} + \lambda_m \\ \lambda_{sq} = L_{sq} i_{sq} \end{cases} \tag{2}$$

where $\lambda_m = L_m i_f$ is the flux linkage caused by PM. For simplicity, the magnetic flux of the rotor is replaced by an equivalent winding with a DC current i_f and an inductance L_f. The rotor flux can be expressed only in d axis as follows:

$$\lambda_f = \lambda_{fd} = i_f L_f + L_m i_{sd} \tag{3}$$

with

$$L_f = \frac{3}{2} \frac{L'_{sd0}}{g} + L_{sl} \tag{4}$$

and mutual inductance

$$L_m = \frac{3L'_{sd0}}{2g} \tag{5}$$

From (2) to (5), the magnetic co-energy in the air gap for a stator is calculated as follows:

$$\begin{aligned} W &= \frac{1}{2}(\lambda_f i_f + \lambda_{sd} i_{sd} + \lambda_{sq} i_{sq}) \\ &= \frac{1}{2}\left\{L_{sd}\left(i_f^2 + i_{sd}^2\right) + L_{sq} i_{sq}^2 + 2L_m i_{sd} i_f\right\} \end{aligned} . \tag{6}$$

$$\Rightarrow W = \frac{1}{2}\left\{\left(\frac{3}{2}\frac{L'_{sd0}}{g} + L_{sl}\right)\left(i_f + i_{sd}\right)^2 + \left(\frac{3}{2}\frac{L'_{sq0}}{g} + L_{sl}\right) i_{sq}^2\right\} \tag{7}$$

Therefore, the attractive force of one stator is received by the derivative of the magnetic co-energy with respect to the axial displacement:

$$F_s = \frac{\partial W}{\partial z} = -\frac{3L'_{sd0}}{4g^2}\frac{dg}{dz}\left(i_{sd} + i_f\right)^2 - \frac{3L'_{sq0}}{4g^2}\frac{dg}{dz} i_{sq}^2 \tag{8}$$

and the motoring torque for one stator is calculated as follows:

$$\begin{aligned} T_s &= P(-\lambda_{sd} i_{sq} + \lambda_{sq} i_{sd}) \\ &= \frac{3PL'_{sd0}}{2g} i_f i_{sq} + \frac{3P(L'_{sd0} - L'_{sq0})}{2g} i_{sd} i_{sq} = T_{seff} + T_{srl} \end{aligned} \tag{9}$$

where

P is the number of pole pairs

$T_{seff} = \dfrac{3PL'_{sd0}}{2g} i_f i_{sq}$ is the effective torque caused by q-axis current

$T_{srl} = \dfrac{3P(L'_{sd0} - L'_{sq0})}{2g} i_{sd} i_{sq}$ is the reluctance torque caused by the different between d- and q-axis inductances.

From (9), the output torque of the AGBM is a combination of an excitation torque and a reluctance torque. That means, in every operation mode, the motor has to produce an additional torque to compensate the reluctance torque. In the non-salient pole rotor, this reluctance torque can be ignored to make control system simpler. However, in the salient-pole rotor when the reluctance torque can reach the relative high amplitude, the neglect of this torque component will reduce the quality of system, especially in operation mode with axial load ($i_d \neq 0$).

From (8) and (9) F_1 and T_1 are calculated by substituting $g = g_0 + z$, $i_{sd} = i_{d1}$, and $i_{sq} = i_{q1}$, and F_2 and T_2 are calculated by substituting $g = g_0 - z$, $i_{sd} = i_{d2}$, and $i_{sq} = i_{q2}$. Thus, the total axial force F and torque T are given by:

$$F = F_2 + F_1 = \frac{3L'_{sd0}}{4(g_0 - z)^2}(i_{d2} + i_f)^2 + \frac{3L'_{sq0}}{4(g_0 - z)^2} i_{q2}^2 - \frac{3L'_{sd0}}{4(g_0 + z)^2}(i_{d1} + i_f)^2 - \frac{3L'_{sq0}}{4(g_0 + z)^2} i_{q1}^2 \quad (10)$$

$$T = T_1 + T_2 = \frac{3PL'_{sd0}}{2(g_0 + z)} i_f i_{q1} + \frac{3P(L'_{sd0} - L'_{sq0})}{2(g_0 + z)} i_{d1} i_{q1} + \frac{3PL'_{sd0}}{2(g_0 - z)} i_f i_{q2} + \frac{3P(L'_{sd0} - L'_{sq0})}{2(g_0 - z)} i_{d2} i_{q2} \quad (11)$$

where g_0 is the axial gap at the equilibrium point and z is the displacement.
For linearization at the equilibrium point ($z = 0$), (10) and (11) are expanded into a Maclaurin series and the first-order term is taken, yielding:

$$\begin{aligned} F = {} & K_{Fd}\left\{(i_{d2} + i_f)^2 - (i_{d1} + i_f)^2\right\} + K_{Fq}\left(i_{q2}^2 - i_{q1}^2\right) + \\ & + 2K_{Fd}\left\{(i_{d2} + i_f)^2 + (i_{d1} + i_f)^2\right\} z / g_0 \; + 2K_{Fq}\left(i_{q2}^2 + i_{q1}^2\right) z / g_0 \end{aligned} \quad (12)$$

$$T = K_T(i_{q1} + i_{q2}) + K_T(i_{q2} - i_{q1}) z / g_0 + K_R(i_{d1} i_{q1} + i_{d2} i_{q2}) + K_R(i_{d2} i_{q2} - i_{d1} i_{q1}) z / g_0 \quad (13)$$

where

$K_{Fd} = \dfrac{3L'_{sd0}}{4g_0^2}$ and $K_{Fq} = \dfrac{3L'_{sq0}}{4g_0^2}$ are the force factors,

$K_T = -\dfrac{3PL'_{sd0} i_f}{2g_0}$ and $K_R = -\dfrac{3(L'_{sd0} - L'_{sq0})}{2g_0}$ are the torque factors.

To increase the total moment twice the component moment created by one stator, the moment-generated currents for both stators must be same direction and value. To keep the rotor in right position between two stators, the forces acting on rotor from both sides must be same value but inverse, i.e. under the effect of the axial load, if the force-generated current of one side increases, then correspondingly, that current of other side has to decrease the same amount. The rotating torque can be controlled effectively by using the quadrate-axis current, and the axial force can be controlled by changing the direct-axis current. It is supposed that:

$$\begin{cases} i_{q1} = i_{q2} = i_q \\ i_{d1} = i_{d0} - i_d \\ i_{d2} = i_{d0} + i_d \end{cases} \quad (14)$$

where i_{d0} is an offset current, and the value can be zero or a small value around zero.

Inserting (14) into (12) and (13) yields:

$$T = 2K_T i_q + 2K_R i_{d0} i_q + 2K_R i_d i_q \frac{z}{g_0} = T_{eff} + T_{rl0} + T_{rlz} \tag{15}$$

$$\begin{aligned} F &= 4K_{Fd}(i_f + i_{d0})i_d + \\ &+ 4\left\{K_{Fd}(i_d^2 + i_{d0}^2 + i_f^2) + 2K_{Fd} i_f i_{d0} + K_{Fq} i_q^2\right\}\frac{z}{g_0} \end{aligned} \tag{16}$$

From (15), the total torque consists of three components.

1) The first component, $T_{eff} = 2K_T i_q$, is the efficient torque of the AGBM, this is main component of the output torque, which is caused by the interaction between PM flux and stator flux.
2) The second one, $T_{rl0} = 2K_R i_{d0} i_q$, is the reluctance torque caused by current i_{d0}. Therefore, assuming that $i_{d1} = -i_{d2} = -i_d$ *i.e.* $i_{d0} = 0$ then this reluctance torque is eliminated.
3) The last one, $T_{rlz} = 2K_R i_d i_q z / g_0$, is reluctance torque caused by current i_d under the effect of the displacement z. When the displacement is well controlled to be zero, or very small in comparison with air gap at the equilibrium point g_0, the influence of this component can be neglected.

As the result, the total torque becomes as follows:

$$T = 2K_T i_q \tag{17}$$

Obviously, the effect of the inductance difference to the total torque is vanished.
Using the control law (14), the total axial force is received from (16) when $i_{d0} = 0$ as

$$F = 4K_{Fd} i_f i_d + 4\left\{K_{Fd}(i_d^2 + i_f^2) + K_{Fq} i_q^2\right\} z / g_0 \tag{18}$$

When the displacement is zero or very small in comparison with air gap at the equilibrium point g_0, the total torque becomes

$$F = 4K_{Fd} i_f i_d \tag{19}$$

From (17) and (19), it is easy to see that the total torque is proportional with the quadrate axis current and the axial force is proportional with the direct axis current. Although the axial force depends lightly on the quadrature axis current, its main component is proportional to the direct axis current, so a decoupled d- and q-axis current control system can be implemented to control the axial force and motoring torque independently.

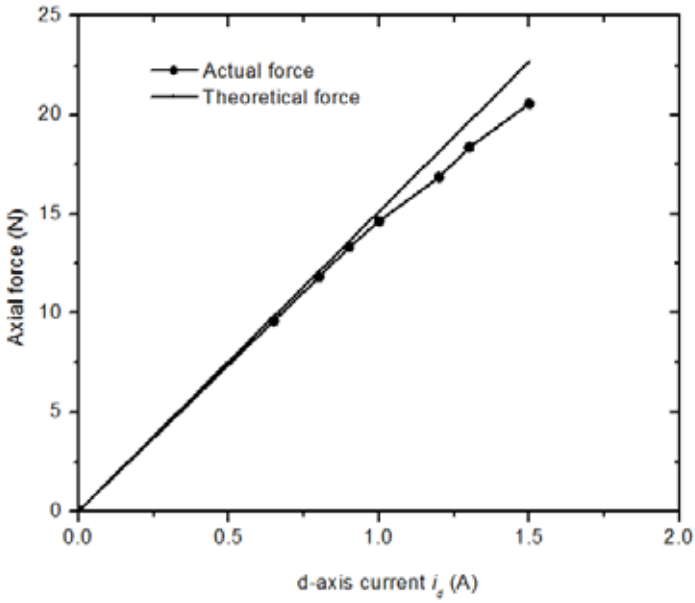

Fig. 8. Relation between axial force and d-axis current

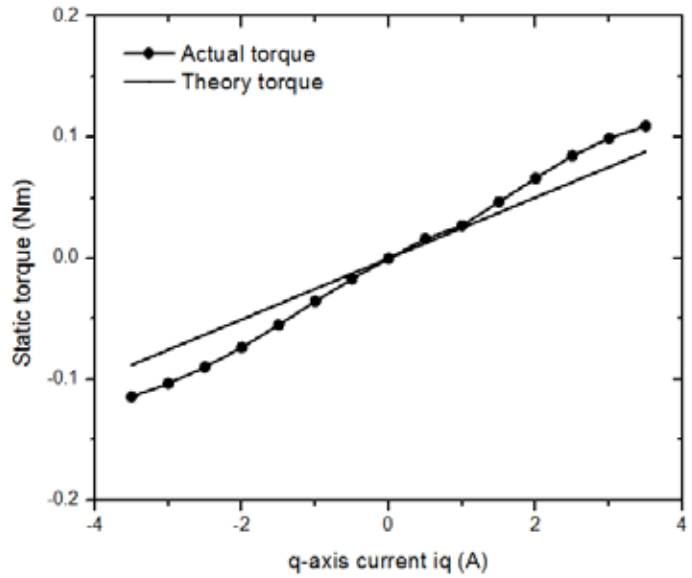

Fig. 9. Relation between rotational torque and q-axis current

From (2), (3), (17) and (19), the mathematical model of the AGBM is completely constructed with voltage, force, and torque equations. It can be seen that these are simple linear equations, so the control system can be easily implemented with conventional controllers.

3. Vector Control Structure

3.1 Generality

Vector control of the AGBM is based on decomposition of the instantaneous stator current into two components: axial force-producing current i_d (also flux current) and torque-producing current i_q. By this way the control structure of the AGBM becomes similar to that of the DC motor.

As stated above, the motoring torque of the AGBM can be controlled by the q-axis current (i_q), while the axial force can be controlled by the d-axis current (i_d). Fig. 10 shows the control scheme proposed for the AGBM drive with decoupled current controller.

The axial displacement from the equilibrium point along the z-axis, z, can be detected by the gap sensor. The detected axial position is compared with the axial position command z_{ref} and the difference is input to the axial position controller R_z. The position command z_{ref} is always set to zero to ensure the rotor is at the midpoint between the two stators. The output of the axial position controller is used to calculate the d-axis reference current i_{dref}. The d-axis reference currents for the two stator windings i_{d1ref} and i_{d2ref} can be generated by using the offset current i_{d0} and respectively subtracting or adding i_{dref}. The value of the offset current can be zero or a small value around zero.

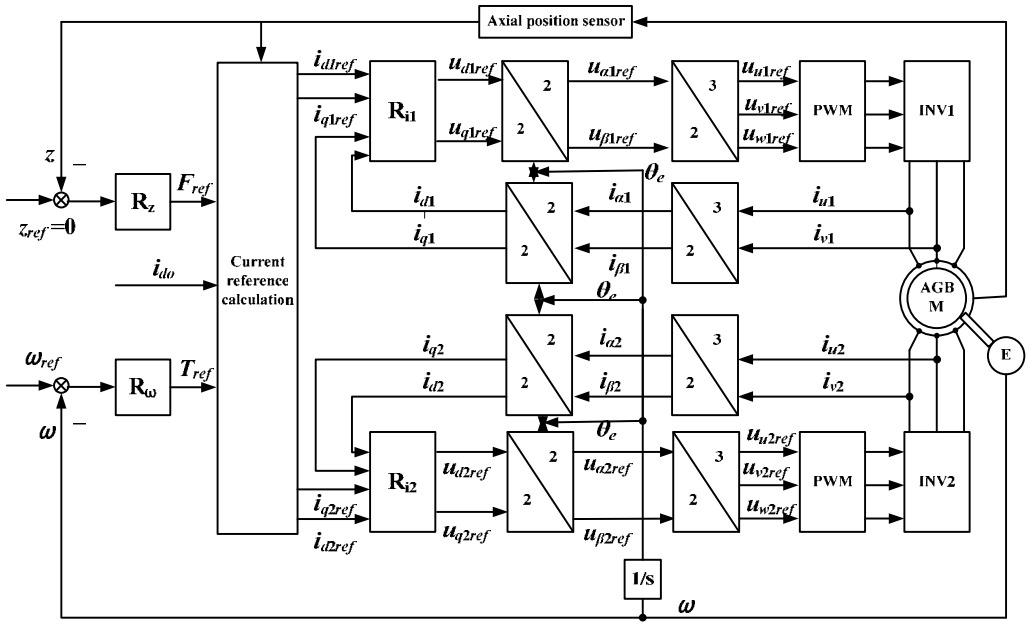

Fig. 10. Control structure for the AGBM.

The rotor speed detected from the encoder is compared with the reference speed and the difference is input to the speed controller R_ω. The output of the speed controller is used to calculate the q-axis reference current i_{qref}. The q-axis reference currents for the two stator windings i_{q1ref} and i_{q2ref} are then set the same as the calculated current i_{qref}.

The motor currents in the two-phase stator reference frame a,β are calculated by measuring two actual phase currents. Consequently, the d,q components are obtained using the rotor

position from the encoder. The quadrature components are controlled by the reference value that is given by the speed controller, while the direct components are controlled by the reference value that is given by the axial position controller. The outputs of the current controllers, representing the voltage references, are subsequently directed to the motor using the pulse width modulation (PWM) technique, once an inverse transformation from the rotating frame to the three-phase stator reference frame has been performed. All the controllers are PI controller except that the axial position controller is PID.

3.2 Current Control

Most of the modern AC motor drives have a control structure comprising an internal current control loop. Consequently, the performance of the drive system largely depends on the quality of applied current control strategy.

The main task of the current control loop is to force the current in a three-phase motor to follow the reference signals. By comparing the reference currents and measured currents, the current control loop generates the switching states for the inverter which decrease the current errors. Hence, in general the current control loop implements two tasks: *error compensation* (decrease current error) and *modulation* (determine switching states).

The design of the current controllers in the simplest cases of so-called parametric synthesis of linear controllers is limited to the selection of a controller type such as P, PI or PID and the definition of optimal setting of its parameters according to the criterion adopted. This design is normally done with complete knowledge of the controlled object and is described in many literatures (Kazmierkowski & Melasani, 1998), (Gerd, 2004).

From equation (2), the stator voltage equations are rewritten in a slightly different form as follows:

$$\begin{cases} u_{sd} = \left(R_s + sL_{sd}\right) i_{sd} - \Delta u_{sd} \\ u_{sq} = \left(R_s + sL_{sq}\right) i_{sq} + \Delta u_{sq} \end{cases} \tag{20}$$

with s is laplace operator and

$$\begin{cases} \Delta u_{sd} = \omega_e L_{sq} i_{sq} \\ \Delta u_{sq} = \omega_e L_{sd} i_{sd} + \omega_e \lambda_m \end{cases} \tag{21}$$

Equations (20) and (21) describe a coupled system. In actual, the current control loop is much faster than a change of the rotor speed and rotor flux, therefore decoupling of the two current controllers can be achieved by adding voltages Δu_{sd} and Δu_{sq} at the output of the current controllers compensating the cross coupling in the motor.

The structure of the current control loop is shown in Fig. 11.

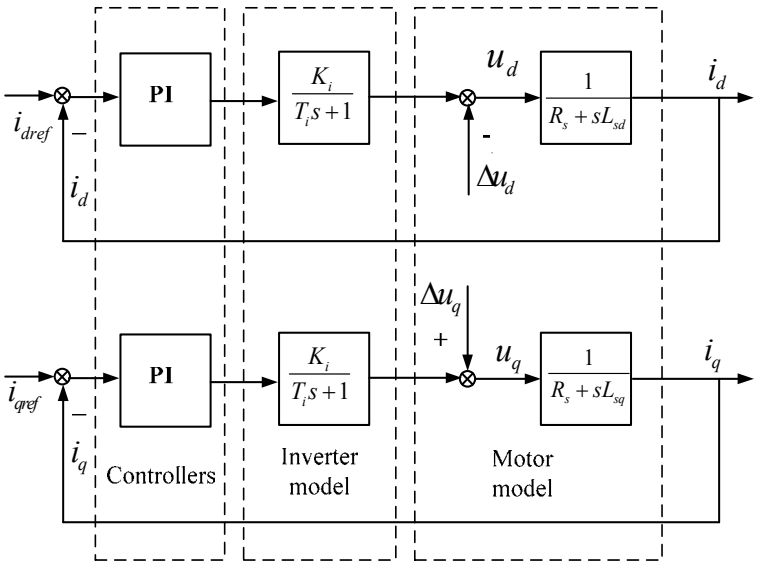

Fig. 11. Decoupled current control loop

Due to the difference between the d- and q-axis inductance, the current control design for i_d and i_q is performed separately.

The decoupled current control loop of the d-axis current contains a dominant stator time constant $T_s = L_{sd}/R_s$ and an inverter time constant T_i. The latter is the time required for the conversion of the reference voltage to the inverter output voltage, mainly depending on the constant sample time τ_s and PWM frequency $f_{PWM} = 1/T_{PWM}$:

$$T_i = \tau_s + T_{PWM} \tag{22}$$

Due to the similarity of the control structure, the design of current controller is only made for one current control loop, the other current control loops are obtained similarly.

Considering that the PI controller is utilized for current control, the open-loop transfer function of both d-axis and q-axis is:

$$G_{0i}(s) = K_{pd}\frac{T_{id}s+1}{T_{id}s}\frac{K_i}{T_i s+1}\frac{1}{T_{sd}s+1}\frac{1}{R_s} \tag{23}$$

According to optimal modulus criterion, the time constant T_{id} of the PI controller within such system is optimally chosen to neutralize the largest time constant in the loop:

$$T_{id} = T_{sd} \tag{24}$$

The optimum value of the controller gain is chosen as follows:

$$K_{pd} = \frac{R_s T_{id}}{2K_i T_i} \tag{25}$$

Consequently, the closed-loop transfer function of the d-axis current control loop becomes:

$$G_{si}(s) = \frac{i_d}{i_{dref}} = \frac{G_{0i}}{G_{0i}+1} = \frac{1}{2T_i^2 s^2 + 2T_i s + 1} \tag{26}$$

For the overlaid axial displacement control loop, the closed-loop transfer function is often simplified to a first order system with an equivalent time constant $T_{eq} = 2\sqrt{2}T_i$:

$$G_{si}(s) = \frac{i_d}{i_{dref}} = \approx \frac{1}{T_{eq}s + 1} \tag{27}$$

By the same way, the parameters of the q-axis current controller are as follows

$$\begin{cases} T_{iq} = T_{sq} \\ K_{pq} = \dfrac{R_s T_{iq}}{2K_i T_i} \end{cases} \tag{28}$$

and the closed-loop transfer function of the q-axis current control loop used for overlaid speed control loop becomes:

$$G_{si}(s) = \frac{i_q}{i_{qref}} = \approx \frac{1}{T_{eq}s + 1} \tag{29}$$

3.3 Axial Displacement Control

For simplicity, it is assumed that the radial motion of the rotor is restricted by two ideal radial bearings. Therefore, the axial motion is independent of the radial motion and can be expressed as follows:

$$F - F_L = m\ddot{z} \tag{30}$$

where m is the mass of the moving parts and F is the axial force. Then substituting (18) into (30) yields

$$m\ddot{z} + F_L = 4K_{Fd} i_f i_d + 4\left\{K_{Fd}\left(i_f^2 + i_d^2\right) + K_{Fq} i_q^2\right\}\frac{z}{g_0}. \tag{31}$$

This can be summarized as

$$m\ddot{z} + F_L + K_z z = K_m i_d \tag{32}$$

where

$K_z = -4\left\{K_{Fd}\left(i_f^2 + i_d^2\right) + K_{Fq} i_q^2\right\} / g_0$ is the stiffness of the motor, and

$K_m = 4K_{Fd} i_f$ is the force gain.

It is easy to see that K_z is negative, which means that this system is unstable. To stabilize the system, a controller with the derivative component must be used. The axial displacement control loop is shown in Fig. 12.
The axial displacement control loop contains the closed-loop transfer function of the inner d-axis current control loop and axial motion function. Since the axial load is usually unknown, it is handled in a first step as an external system disturbance.
Assuming that the proportional derivative controller (PD) is used, the output of the axial position controller will represent the direct axis reference current, i.e.,

$$i_d = -K_P z - K_D \dot{z} \tag{33}$$

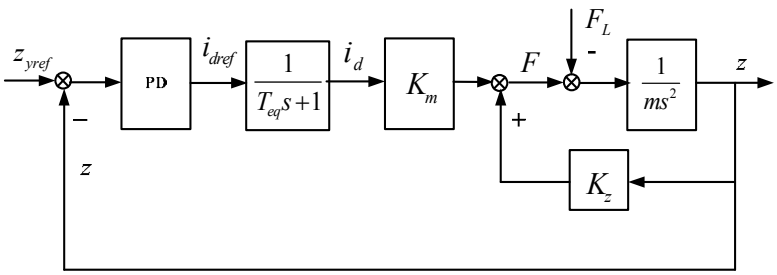

Fig. 12. Axial displacement control loop

where K_p is the proportional constant and K_d is the derivative constant of the axial position controller. Substituting (33) into (32) gives

$$m\ddot{z} + K_m K_D \dot{z} + \left(K_z + K_m K_P\right) z = 0\,. \tag{34}$$

The system becomes stable only when all the constant coefficients of the polynomial function have the same sign. Therefore, if $K_d > 0$, the system will be stable if the proportional constant satisfies the condition

$$\begin{cases} K_P > -\dfrac{K_z}{K_m} = \dfrac{K_{Fd}\left(i_f^2 + i_d^2\right) + K_{Fq} i_q^2}{K_{Fd} i_f g_0} \\ K_D > 0 \end{cases}. \tag{35}$$

Steady-state error occurs when only the PD controller is used, and to remove this, a PID controller should be used. The transfer function of the PID controller is expressed as follows:

$$G_{cz}(s) = K_P + \frac{K_I}{s} + K_D s \tag{36}$$

By the same way as stated above, the system will be stable when the controller parameters satisfy:

$$\begin{cases} K_P > \dfrac{K_{Fd}\left(i_f^2 + i_d^2\right) + K_{Fq} i_q^2}{K_{Fd} i_f g_0} \\ K_I < \dfrac{K_D\left(K_m K_P + K_z\right)}{m} \\ K_I > 0 \\ K_D > 0 \end{cases} \tag{37}$$

In practice, the output of an ideal derivative element unfortunately includes considerable noise. High frequency noise at the input terminals results in significant amplification at the output terminals, therefore the ideal derivative element should be avoided in practical implementation. The practical controller function is expressed as follows:

$$G_{cz}(s) = K_P + \frac{K_I}{s} + \frac{K_D s}{T_f s + 1} \tag{38}$$

The denominator determines the high frequency limit with the cut-off frequency as $1/T_f$ and the numerator acts as a derivative function in the angular frequency range higher than $1/K_D$; therefore, the practical PID controller executes as a derivative function in a frequency range from $1/K_D$ to $1/T_f$. The low frequency gain is 0 dB and the high frequency gain is limited to K_D / T_f, hence T_f can be chosen from the actual signal condition.

In discrete time, equation (31) can be expressed as:

$$G_{cz}(s) = K_P + \frac{K_I \tau_s \left(z+1\right)}{2\left(z-1\right)} + \frac{2K_D\left(z-1\right)}{\left(2T_f + \tau_s\right)z - \left(2T_f - \tau_s\right)} \tag{39}$$

when the bilinear transform method is utilized.

3.4 Speed Control

For all motor types, the difference of electromagnetic torque T and load torque T_L causes acceleration of the rotor according to the mechanical property of the motor drives. The rotational motion equation can be written as:

$$T - T_L = J\frac{d\omega}{dt}, \tag{40}$$

or in fixed transfer function:

$$\frac{\omega}{T - T_L} = \frac{1}{Js} \tag{41}$$

Torque can be controlled by the q-axis current as shown in equation (16); therefore, the speed control loop is shown in Fig. 13.

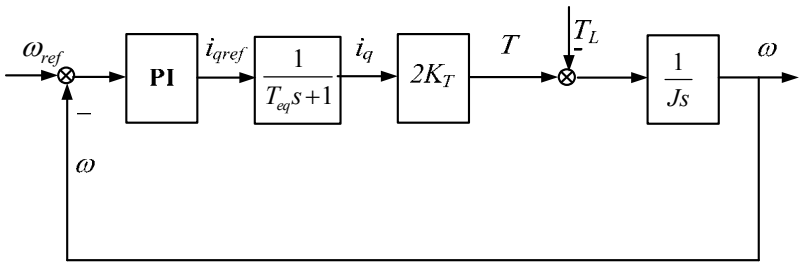

Fig. 13. Speed control loop

Like the axial displacement control loop, the speed control loop also contains the inner q-axis current control loop and rotational motion function. Since the rotational load is unknown, it is handled in a first step as an external system disturbance. The influence of the speed measurement is usually combined with the equivalent time constant of the current control.
Consequently, the resulting speed loop to be controlled is:

$$\frac{\omega}{i_{qref}} = \frac{2K_T}{T_{eq}s+1}\frac{1}{Js} \tag{42}$$

The simplest speed controller is a proportional controller (P), converting the speed error in the q-axis current command i_{qref}. Assuming no load (T_L=0), a positive speed error creates positive electromagnetic torque accelerating the drive until the error vanishes, and a negative speed error gives negative electromagnetic torque decelerating the drive until the error vanishes (braking mode). Thus, the steady-state error is zero in the no-load case. When the P-controller is used, the closed-loop transfer function is:

$$\frac{\omega}{\omega_{ref}} = \frac{1}{1+\frac{J}{2K_TK_p}s+\frac{JT_{eq}}{2K_TK_p}s^2} = \frac{1}{1+2\xi\left(\frac{s}{\omega_n}\right)+\left(\frac{s}{\omega_n}\right)^2} \tag{43}$$

with:

$$\omega_n = \sqrt{\frac{2K_TK_p}{JT_{eq}}} \text{ is the natural angular frequency, and} \tag{44}$$

$$\xi = \sqrt{\frac{J}{8K_TK_pT_{eq}}} \text{ is the damping constant.} \tag{45}$$

From these equations, it can be seen that the speed response to the external torque is determined by the natural angular frequency. Faster response is obtained at higher ω_n, while strong damper is achieved at higher ζ. For arriving at a compromise, the optimum gain of the current control is chosen as:

$$K_P = \frac{J}{4K_T T_{eq}} \text{ when the damping constant } \xi = 1/\sqrt{2}\,. \tag{46}$$

However, a simple P controller yields a steady-state error in the presence of rotational load torque, this error can be estimated as:

$$e_\omega = \left(\omega_{ref} - \omega\right)\Big|_{t\to\infty} = \frac{T_L}{K_p} \tag{47}$$

The most common approach to overcome this problem is applying an integral-acting part within the speed controller. The speed controller function is expressed as:

$$G_{c\omega}(s) = K_p\left(\frac{1+T_{i\omega}s}{T_{i\omega}s}\right) \tag{48}$$

Then the open-loop transfer function of speed loop is:

$$G_{0\omega}(s) = K_p \frac{1+T_{i\omega}s}{T_{i\omega}s}\frac{2K_T}{T_{eq}s+1}\frac{1}{Js} \tag{49}$$

Similar to the current control, the calculation of the controller parameters $K_{1\omega}$ and $T_{1\omega}$ depend on the system to be controlled. For optimum speed response, parameter calculation is done according to symmetrical optimization criterion. The time constant $T_{1\omega}$ of the speed controller is chosen bigger than the largest time constant in the loop, and the gain is chosen so that the cut-off frequency is at maximum phase. The results can be expressed as:

$$\begin{cases} T_{i\omega} = 20T_{eq} \\ K_p = \dfrac{J}{2K_T\sqrt{T_{i\omega}T_{eq}}} \end{cases} \tag{50}$$

4. Experimental Results

4.1 Hardware

To demonstrate the proposed control method for a PM-type AGBM, an experimental setup was constructed; it is shown schematically in Fig. 14. The rotor disc, shown in Fig. 15, has a diameter of 50mm. Four neodymium magnets with a thickness of 1mm for each side are mounted to the disc's surfaces to create two pole pairs. In this paper, only rotational motion of the rotor and translation of the stator along the z axis are considered, hence for a more simple experiment, the rotor is supported by two radial ball bearings that restrict the radial motion.
The stator, shown in Fig. 16, has a core diameter 50 mm and six concentrated wound poles, each with 200 coil turns. The stators can slide on the linear guide to ensure a desired air gap between the rotor and the two stators. A DC generator (Sanyo T402) is installed to give the load torque. A rotary encoder (Copal RE30D) measures the rotor angle and an eddy-current-type displacement sensor (Shinkawa VC-202N) measures the axial position.

The control hardware of the AGBM drive is based on a dSPACE DS1104 board dedicated to the control of electrical drives. It includes PWM units, general purpose input/output units (8 ADC and 8 DAC), and an encoder interface. The DS1104 reads the displacement signal from the displacement sensor via an A/D converter, and the rotor angle position and speed from the encoder via an encoder interface. Two motor phase currents are sensed, rescaled, and converted to digital values via the A/D converters. The DS1104 then calculates reference currents using the rotation control and axial position control algorithms and sends its commands to the three-phase inverter boards. The AGBM is supplied by two three-phase PWM inverters with a switching frequency of 20 kHz.

Stator phase resistance R_s	2.6 Ω
Effective inductance per unit gap in d axis L'_{sd0}	8.2e-6 Hm
Effective inductance per unit gap in q axis L'_{sq0}	9.6e-6 Hm
Leakage inductance L_{sl}	6e-3 H
Inertial moment of rotor J	0.00086 kgm^2
Number of pole pairs P	1
Permanent magnet flux λ_m	0.0126 Wb

Table 1. Parameters of salient pole AGBM

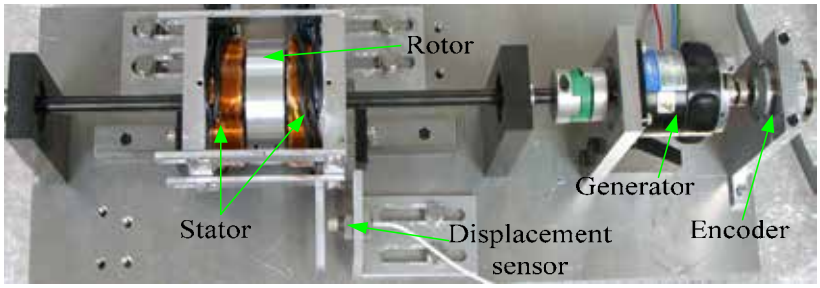

Fig. 14. Picture of the experimental setup

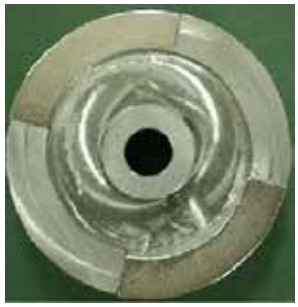

Fig. 15. Picture of the rotor of the AGBM

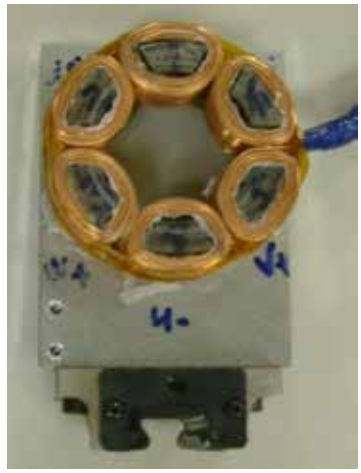

Fig. 16. Picture of the stator of the AGBM

4.2 Response of Speed and Axial Displacement

Fig. 17 shows the axial displacement at 0 rpm. The original displacement is set to 0.32 mm, and at the time of 0.45 s, the axial position controller starts to work. In transient state, the maximum error is 0.05 mm, much smaller than the air gap at the equilibrium point (g_0 = 1.7mm) and the settling time is about 0.05 s. After that, the displacement is almost zero in a steady state, i.e. the air gaps between stators and rotor are equal ($g_1 = g_2 = g_0$). The rotor now stands in the middle of two stators.

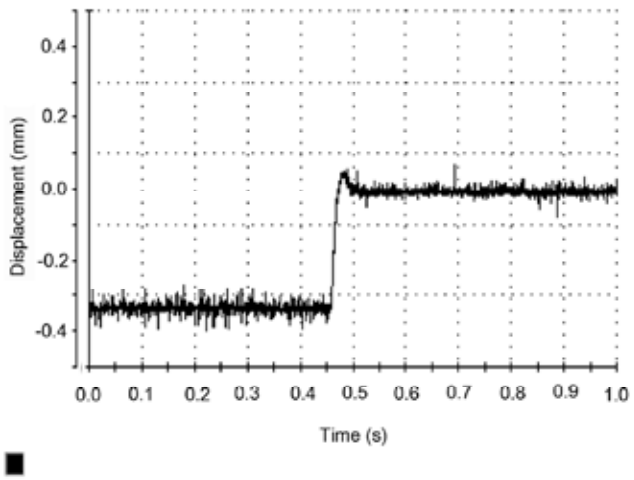

Fig. 17. Response of axial displacement at zero speed

Fig. 18 describes the change in the speed from zero to 6000 rpm and vice versa when the displacement is zero and the limited current is ±5A. The AGBM does not bear any load. With small starting time (about 0.7s) and stopping time (about 0.4s) the AGBM drive shows its good dynamic response.

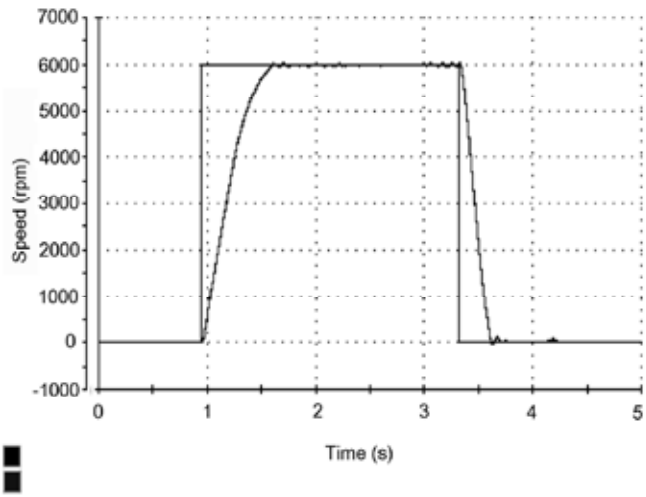

Fig. 18. Response of speed at zero displacement

Figs. 19 and 20 show response of the axial displacement and the speed when the AGBM starts to work. Initial displacement error is adjusted to 0.32mm, and the reference speed is 1500 rpm. When the AGBM operates, the displacement jumps immediately to zero. At the same time, the rotor speed increases and reaches 1500 rpm after 0.5s without influence of each other.
From above experimental results, it is obvious that the axial displacement and the speed are controlled independently with each other.
Fig. 21 illustrates the change of the direct axis current i_d, the quadrate axis current i_q, and the displacement when the motor speed changes from 1000 rpm to 1500 rpm and vice versa. The limited currents are set to ±3A. The AGBM drive works with rotational load. The rotational load is created by closing the terminals of a DC generator using a 1 Ω resistor. When the reference speed is changed from 1000 rpm to 1500 rpm, the q-axis current increases to the limited current. At the speed of 1500 rpm, the q-axis current is about 2.5A. Due to the influence of the q-axis current as shown in equation (18), there is little higher vibration in the displacement and the d-axis current at 1500 rpm. However, the displacement error is far smaller than the equilibrium air gap g_0, therefore the influence can be neglected.

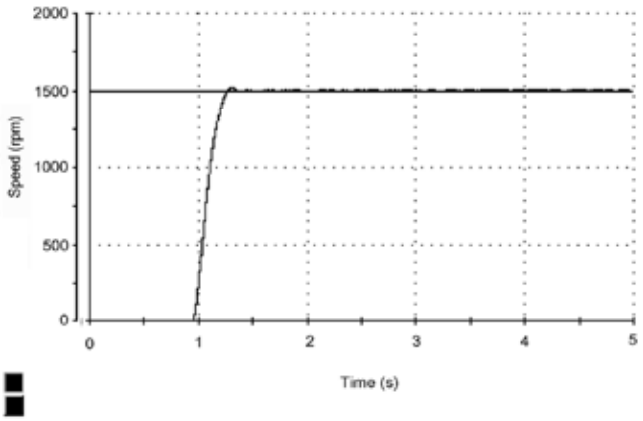

Fig. 19. Response of speed at start

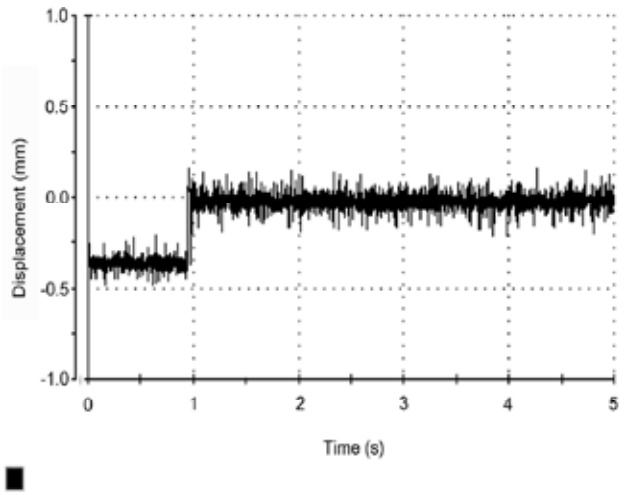

Fig. 20. Response of axial displacement at start

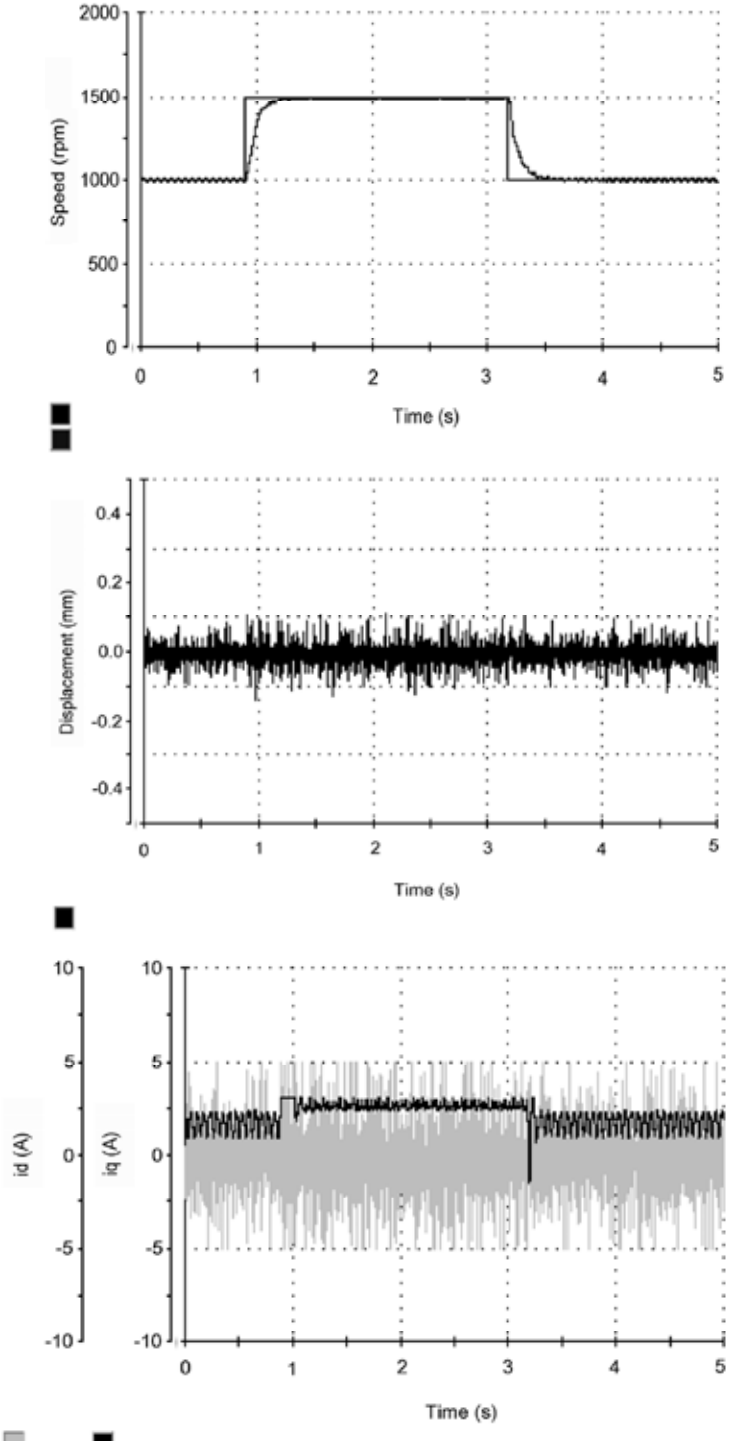

Fig. 21. Currents and displacement when rotor speed was changed

5. Conclusion

This chapter introduces and explains a vector control of the salient two-pole AGBM drives as required for high-performance motion control in many industrial applications.
Firstly, a general dynamic model of the AGBM used for vector control is developed, in which the saliency of the rotor is considered. The model development is based on the reference frame theory, in which all the motor electrical variables is transformed to a rotor field-oriented reference frame (d,q reference frame). As seen from the d,q reference frame rotating with synchronous speed, all stator and rotor variables become constant in steady state. Thus, dc values, very practical regarding DC motor control strategies, are obtained. Furthermore, by using this transformation, the mutual magnetic coupling between d- and q-axes is eliminated. The stator current in d-axis is only active in the affiliated windings of the d-axis, and the same applies for the q-axis.
Secondly, the vector control technique for the AGBM drives is presented in detail. In spite of many different control structures available, the cascaded structure, inner closed-loop current control and overlaid closed-loop speed and axial position control, is chosen. This choice guarantees that the AGBM drive is closed to the modern drives, which were developed for the conventional motors. Furthermore, the closed-loop vector control method for the axial position and the speed is developed in the way of eliminating the influence of the reluctance torque. The selection of suitable controller types and the calculation of the controller parameters, both depending on the electrical and mechanical behavior of the controlled objects, are explicitly evaluated.
Finally, the AGBM was fabricated with an inset PM type rotor, and the vector control with decoupled d- and q-axis current controllers was implemented based on dSpace DS1104 and Simukink/Matlab. The results confirm that the motor can perform both functions of motor and axial bearing without any additional windings. The reluctance torque and its influence are rejected entirely. Although, there is very little interference between the axial position control and speed control in high speed range and high rotational load, the proposed AGBM drive can be used for many kind of applications, which require small air gap, high speed and levitation force.

6. References

Aydin M.; Huang S. and Lipo T. A. (2006). Torque quality and comparison of internal and external rotor axial flux surface-magnet disc machines. IEEE Transactions on Industrial Electronics, Vol. 53, No. 3, June 2006, pp. 822-830.

Chiba A.; Fukao T.; Ichikawa O.; Oshima M., Takemoto M. and Dorrell D.G. (2005). *Magnetic Bearings and Bearingless Drives*, 1st edition, Elsevier, Burlington, 2005.

Dussaux M. (1990). The industrial application of the active magnetic bearing technology, *Proceedings of the 2nd International Symposium on Magnetic Bearings*, pp. 33-38, Tokyo, Japan, July 12–14, 1990.

Fitzgerald A. E.; C. Kingsley Jr. and S. D. Uman (1992). *Electric Machinery*, 5th edition, McGraw-Hill, New York,1992.

Gerd Terörde (2004). *Electrical Drives and Control Techniques*, first edition, ACCO, Leuven, 2004.

Grabner, H.; Amrhein, W.; Silber, S. and Gruber, W. (2010). Nonlinear Feedback Control of a Bearingless Brushless DC Motor. *IEEE/ASME Transactions on Mechatronics*, Vol. 15, No. 1, Feb. 2010, pp. 40 – 47.

Horz, M.; Herzog, H.-G. and Medler, N., (2006). System design and comparison of calculated and measured performance of a bearingless BLDC-drive with axial flux path for an implantable blood pump. *Proceedings of International Symposium on Power Electronics, Electrical Drives, Automation and Motion*, (SPEEDAM), pp.1024 – 1027, May 2006.

Kazmierkowski M. P. and Malesani L. (1998). Current control techniques for three-phase voltage-source PWM converters: a survey. IEEE Transactions on Industrial Electronics, Vol. 45, No. 5, Oct. 1998, pp. 691-703.

Marignetti F.; Delli Colli V. and Coia Y. (2008). Design of Axial Flux PM Synchronous Machines Through 3-D Coupled Electromagnetic Thermal and Fluid-Dynamical Finite-Element Analysis," *IEEE Transactions on Industrial Electronics*, Vol. 55, No. 10, pp. 3591-3601, Oct 2008.

Nguyen D. Q. and Ueno S. (2009). Axial position and speed vector control of the inset permanent magnet axial gap type self bearing motor. *Proceedings. of the International Conference on Advanced Intelligent Mechatronics* (AIM2009), pp. 130-135, Singapore, July 2009. (b)

Nguyen D. Q. and Ueno S. (2009). Sensorless speed control of a permanent magnet type axial gap self bearing motor. *Journal of System Design and Dynamics*, Vol. 3, No. 4, July 2009, pp. 494-505. (a)

Okada Y.; Dejima K. and Ohishi T. (1995). Analysis and comparison of PM synchronous motor and induction motor type magnetic bearing, *IEEE Transactions on Industry Applications*, vol. 32, Sept./Oct. 1995, pp. 1047-1053.

Okada, Y.; Yamashiro N.; Ohmori K.; Masuzawa T.; Yamane T.; Konishi Y. and Ueno S. (2005). Mixed flow artificial heart pump with axial self-bearing motor. *IEEE/ASME Transactions on Mechatronics*, Vol. 10, No. 6, Dec. 2005, pp. 658 – 665.

Oshima M.; Chiba A.; Fukao T. and Rahman M. A. (1996). Design and Analysis of Permanent Magnet-Type Bearingless Motors. *IEEE Transaction on Industrial Electronics*, Vol. 43, No. 2, pp. 292-299, Apr. 1996. (b)

Oshima M.; Miyazawa S.; Deido T.; Chiba A.; Nakamura F.; and Fukao T. (1996). Characteristics of a Permanent Magnet Type Bearingless Motor. *IEEE Transactions on Industry Applications*, Vol. 32, No. 2, pp. 363-370, Mar./Apr. 1996. (a)

Schneider, T. and Binder, A. (2007). Design and Evaluation of a 60000 rpm Permanent Magnet Bearingless High Speed Motor. *Proceedings on International Conference on Power Electronics and Drive Systems*, pp. 1 – 8, Bangkok, Thailand, Nov. 2007.

Ueno S. and Okada Y. (1999). Vector control of an induction type axial gap combined motor-bearing. *Proceedings of the IEEE International Conference on Advanced Intelligent Mechatronics*, Sept. 19-23, 1999, Atlanta, USA, pp. 794-799.

Ueno S. and Okada Y. (2000). Characteristics and control of a bidirectional axial gap combined motor-bearing. *IEEE Transactions on Mechatronics*, Vol. 5, No. 3, Sept. 2000, pp. 310-318.

Zhaohui Ren and Stephens L.S. (2005). Closed-loop performance of a six degree-of-freedom precision magnetic actuator, *IEEE/ASME Transactions on Mechatronics*, Vol. 10, No. 6, Dec. 2005 pp. 666 – 674.

5

Passive permanent magnet bearings for rotating shaft : Analytical calculation

Valerie Lemarquand*
LAPLACE. UMR5213. Universite de Toulouse
France

Guy Lemarquand†
LAUM. UMR6613. Universite du Maine
France

1. Introduction

Magnetic bearings are contactless suspension devices, which are mainly used for rotating applications but also exist for translational ones. Their major interest lies of course in the fact that there is no contact and therefore no friction at all between the rotating part and its support. As a consequence, these bearings allow very high rotational speeds. Such devices have been investigated for eighty years. Let's remind the works of F. Holmes and J. Beams (Holmes & Beams, 1937) for centrifuges.
The appearing of modern rare earth permanent magnets allowed the developments of passive devices, in which magnets work in repulsion (Meeks, 1974)(Yonnet, 1978).
Furthermore, as passive magnetic bearings don't require any lubricant they can be used in vacuum and in very clean environments.
Their main applications are high speed systems such as turbo-molecular pumps, turbo-compressors, energy storage flywheels, high-speed machine tool spindles, ultra-centrifuges and they are used in watt-hour meters and other systems in which a very low friction is required too (Hussien et al., 2005)(Filatov & Maslen, 2001).

The magnetic levitation of a rotor requires the control of five degrees of freedom. The sixth degree of freedom corresponds to the principal rotation about the motor axis. As a consequence of the Earnshaw's theorem, at least one of the axes has to be controlled actively. For example, in the case of a discoidal wheel, three axes can be controlled by passive bearings and two axes have to be controlled actively (Lemarquand & Yonnet, 1998). Moreover, in some cases the motor itself can be designed to fulfil the function of an active bearing (Barthod & Lemarquand, 1995). Passive magnetic bearings are simple contactless suspension devices but it must be emphazised that one bearing controls a single degree of freedom. Moreover, it exerts only a stiffness on this degree of freedom and no damping.

*valerie.lemarquand@ieee.org
†guy.lemarquand@ieee.org

Permanent magnet bearings for rotating shafts are constituted of ring permanent magnets. The simplest structure consists either of two concentric rings separated by a cylindrical air gap or of two rings of same dimensions separated by a plane air gap. Depending on the magnet magnetization directions, the devices work as axial or radial bearings and thus control the position along an axis or the centering of an axis. The several possible configurations are discussed throughout this chapter. The point is that in each case the basic part is a ring magnet. Therefore, the values of importance are the magnetic field created by such a ring magnet, the force exerted between two ring magnets and the stiffness associated.

The first author who carried out analytical calculations of the magnetic field created by ring permanent magnets is Durand (Durand, 1968). More recently, many authors proposed simplified and robust formulations of the three components of the magnetic field created by ring permanent magnets (Ravaud et al., 2008)(Ravaud, Lemarquand, Lemarquand & Depollier, 2009)(Babic & Akyel, 2008a)(Babic & Akyel, 2008b)(Azzerboni & Cardelli, 1993).
Moreover, the evaluation of the magnetic field created by ring magnets is only a helpful step in the process of the force calculation. Indeed, the force and the stiffness are the values of importance for the design and optimization of a bearing. So, authors have tried to work out analytical expressions of the force exerted between two ring permanent magnets (Kim et al., 1997)(Lang, 2002)(Samanta & Hirani, 2008)(Janssen et al., 2010)(Azukizawa et al., 2008).
This chapter intends to give a detailed description of the modelling and approach used to calculate analytically the force and the stiffness between two ring permanent magnets with axial or radial polarizations (Ravaud, Lemarquand & Lemarquand, 2009a)(Ravaud, Lemarquand & Lemarquand, 2009b). Then, these formulations will be used to study magnetic bearings structures and their properties.

2. Analytical determination of the force transmitted between two axially polarized ring permanent magnets.

2.1 Preliminary remark

The first structure considered is shown on Fig.1. It is constituted of two concentric axially magnetized ring permanent magnets. When the polarization directions of the rings are antiparallel, as on the figure, the bearing controls the axial position of the rotor and works as a so called axial bearing. When the polarization directions are the same, then the device controls the centering around the axis and works as a so called radial bearing. Only one of the two configurations will be studied thoroughly in this chapter because the results of the second one are easily deducted from the first one. Indeed, the difference between the configurations consists in the change of one of the polarization direction into its opposite. The consequence is a simple change of sign in all the results for the axial force and for the axial stiffness which are the values that will be calculated.
Furthermore, the stiffness in the controlled direction is often considered to be the most interesting value in a bearing. So, for an axial bearing, the axial stiffness is the point. Nevertheless, both stiffnesses are linked. Indeed, when the rings are in their centered position, for symmetry reasons, the axial stiffeness, K_z, and the radial one, K_r, verify:

$$2K_r + K_z = 0 \tag{1}$$

So, either the axial or the radial force may be calculated and is sufficient to deduct both stiffnesses. Thus, the choice was made for this chapter to present only the axial force and stiffness in the sections dealing with axially polarized magnets.

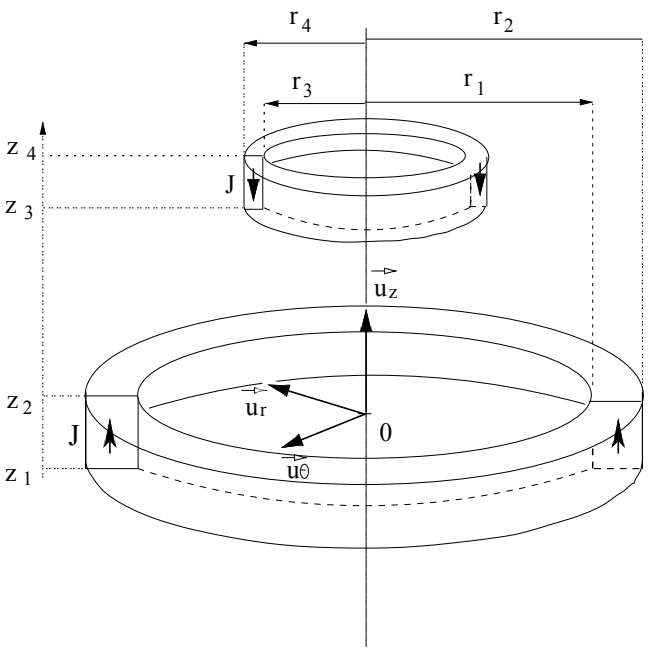

Fig. 1. Axial bearing constituted of two axially magnetized ring permanent magnets. J_1 and J_2 are the magnet polarizations

2.2 Notations

The parameters which describe the geometry of Fig.1 and its properties are listed below:
J_1: outer ring polarization [T].
J_2: inner ring polarization [T].
r_1, r_2: radial coordinates of the outer ring [m].
r_3, r_4: radial coordinates of the inner ring [m].
z_1, z_2: axial coordinates of the outer ring [m].
z_3, z_4: axial coordinates of the inner ring [m].
$h_1 = z_2 - z_1$: outer ring height [m].
$h_2 = z_4 - z_3$: inner ring height [m].
The rings are radially centered and their polarizations are supposed to be uniform.

2.3 Magnet modelling

The axially polarized ring magnet has to be modelled and two approaches are available to do so. Indeed, the magnet can have a coulombian representation, with fictitious magnetic charges or an amperian one, with current densities. In the latter, the magnet is modelled by two cylindrical surface current densities k_1 and k_2 located on the inner and outer lateral surfaces of the ring whereas in the former the magnet is modelled by two surface charge densities located on the plane top and bottom faces of the ring.
As a remark, the choice of the model doesn't depend on the nature of the real magnetic source, but is done to obtain an analytical formulation. Indeed, the authors have demontrated

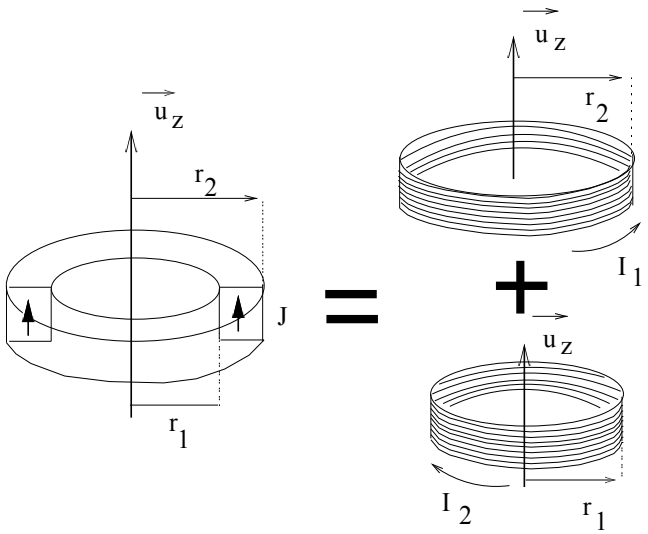

Fig. 2. Model of a ring magnet: amperian equivalence.

that depending on the polarization direction of the source only one of the model generally yields an analytical formulation. So, the choice rather depends on the considered problem.

2.4 Force calculation

The force transmitted between two axially polarized ring permanent magnets is determined by using the amperian approach. Thus, each ring is replaced by two coils of N_1 and N_2 turns in which two currents, I_1 and I_2, flow. Indeed, a ring magnet whose polarization is axial and points up, with an inner radius r_1 and an outer one r_2, can be modelled by a coil of radius r_2 with a current I_2 flowing anticlockwise and a coil of radius r_1 with a current I_1 flowing clockwise (Fig.2).
The equivalent surface current densities related to the coil heights h_1 and h_2 are defined as follows for the calculations:
$k_1 = N_1 I_1 / h_1$: equivalent surface current density for the coils of radii r_1 and r_2.
$k_2 = N_2 I_2 / h_2$: equivalent surface current density for the coils of radii r_3 and r_4.

The axial force, F_z, created between the two ring magnets is given by:

$$F_z = \frac{\mu_0 k_1 k_2}{2} \sum_{i=1}^{2} \sum_{j=3}^{4} (-1)^{1+i+j} \left\{ f_z(r_i, r_j) \right\} \tag{2}$$

with

$$f_z(r_i, r_j) = r_i r_j \int_{z_3}^{z_4} \int_{z_1}^{z_2} \int_{0}^{2\pi} \frac{(\tilde{\tilde{z}} - \tilde{z}) \cos(\tilde{\theta}) d\tilde{z} d\tilde{z} d\tilde{\theta}}{\left(r_i^2 + r_j^2 - 2 r_i r_j \cos(\tilde{\theta}) + (\tilde{\tilde{z}} - \tilde{z})^2 \right)^{\frac{3}{2}}}$$

Parameter	Definition
β	$\frac{b+c}{b-c}$
μ	$\frac{c}{b+c}$
ϵ	$\frac{c}{c-b}$

Table 1. Parameters in the analytical expression of the force exerted between two axially polarized ring magnets.

The current densities are linked to the magnet polarizations by:

$$k_1 = \frac{J_1}{\mu_0} \tag{3}$$

and

$$k_2 = \frac{J_2}{\mu_0} \tag{4}$$

Then the axial force becomes:

$$F_z = \frac{J_1 J_2}{2\mu_0} \sum_{i,k=1}^{2} \sum_{j,l=3}^{4} (-1)^{(1+i+j+k+l)} F_{i,j,k,l} \tag{5}$$

with

$$F_{i,j,k,l} = r_i r_j g\left(z_k - z_l, r_i^2 + r_j^2 + (z_k - z_l)^2, -2r_i r_j\right) \tag{6}$$

$g(a,b,c) = A + S$

$$A = \frac{a^2-b}{c}\pi + \frac{\sqrt{c^2-(a^2-b)^2}}{c}\left(\log\left[\frac{-16c^2}{(c^2-(a^2-b)^2)^{(\frac{3}{2})}}\right] + \log\left[\frac{c^2}{(c^2-(a^2-b)^2)^{(\frac{3}{2})}}\right]\right)$$

$$\begin{aligned} S &= \frac{2ia}{c\sqrt{b+c}}\left((b+c)\mathbf{E}\left[\arcsin\left[\sqrt{\beta},\beta^{-1}\right]\right] - c\mathbf{F}\left[\arcsin\left[\sqrt{\beta},\beta^{-1}\right]\right]\right) \\ &+ \frac{2a}{c\sqrt{b-c}\sqrt{\epsilon}}\left(\frac{c}{\sqrt{\mu}}\mathbf{E}\left[\beta^{-1}\right] - c\sqrt{\mu}\mathbf{K}\left[\beta^{-1}\right]\right) \\ &+ \sqrt{\epsilon\beta^{-1}}\left((b-a^2)\mathbf{K}\left[2\mu\right] + (a^2-b+c)\mathbf{\Pi}\left[\frac{2c}{b+c-a^2}, 2\mu\right]\right) \end{aligned} \tag{7}$$

The special functions used are defined as follows:
$\mathbf{K}[m]$ is the complete elliptic integral of the first kind.

$$\mathbf{K}[m] = \int_0^{\frac{\pi}{2}} \frac{1}{\sqrt{1 - m\sin(\theta)^2}} d\theta \tag{8}$$

$\mathbf{F}[\phi, m]$ is the incomplete elliptic integral of the first kind.

$$\mathbf{F}[\phi, m] = \int_0^{\phi} \frac{1}{\sqrt{1 - m\sin(\theta)^2}} d\theta \tag{9}$$

$\mathbf{E}[\phi, m]$ is the incomplete elliptic integral of the second kind.

$$\mathbf{E}[\phi, m] = \int_0^{\phi} \sqrt{1 - m\sin(\theta)^2} d\theta \tag{10}$$

$$\mathbf{E}[m] = \int_0^{\frac{\pi}{2}} \sqrt{1 - m\sin(\theta)^2} d\theta \tag{11}$$

$\mathbf{\Pi}[n, m]$ is the incomplete elliptic integral of the third kind.

$$\mathbf{\Pi}[n, m] = \mathbf{\Pi}\left[n, \frac{\pi}{2}, m\right] \tag{12}$$

with

$$\mathbf{\Pi}[n, \phi, m] = \int_0^{\phi} \frac{1}{\sqrt{1 - n\sin(\theta)^2}} \frac{1}{\sqrt{1 - m\sin(\theta)^2}} d\theta \tag{13}$$

3. Exact analytical formulation of the axial stiffness between two axially polarized ring magnets.

The axial stiffness, K_z existing between two axially polarized ring magnets can be calculated by deriving the axial force transmitted between the two rings, F_z, with regard to the axial displacement, z:

$$K_z = -\frac{d}{dz} F_z \tag{14}$$

F_z is replaced by the integral formulation of Eq.5 and after some mathematical manipulations the axial stiffness can be written:

$$K_z = \frac{J_1 J_2}{2\mu_0} \sum_{i,k=1}^{2} \sum_{j,l=3}^{4} (-1)^{(1+i+j+k+l)} C_{i,j,k,l} \tag{15}$$

where

$$\begin{aligned} C_{i,j,k,l} &= 2\sqrt{\alpha}\mathbf{E}\left[\frac{-4r_i r_j}{\alpha}\right] - 2\frac{r_i^2 + r_j^2 + (z_k - z_l)^2}{\sqrt{\alpha}}\mathbf{K}\left[\frac{-4r_i r_j}{\alpha}\right] \\ \alpha &= (r_i - r_j)^2 + (z_k - z_l)^2 \end{aligned} \tag{16}$$

4. Study and characteristics of axial bearings with axially polarized ring magnets and a cylindrical air gap.

4.1 Structures with two ring magnets

This section considers devices constituted of two ring magnets with antiparallel polarization directions. So, the devices work as axial bearings. The influence of the different parameters of the geometry on both the axial force and stiffness is studied.

4.1.1 Geometry

The device geometry is shown on Fig.1. The radii remain the same as previously defined. Both ring magnets have the same axial dimension, the height $h_1 = h_2 = h$. The axial coordinate, z, characterizes the axial displacement of the inner ring with regard to the outer one. The polarization of the magnets is equal to $1T$.
The initial set of dimensions for each study is the following:
$r_1 = 25mm, r_2 = 28mm, r_3 = 21mm, r_4 = 24mm, h = 3mm$
Thus the initial air gap is $1mm$ wide and the ring magnets have an initial square cross section of $3 \times 3mm^2$.

4.1.2 Air gap influence

The ring cross section is kept constant and the radial dimension of the air gap, $r_1 - r_3$, is varied by modifying the radii of the inner ring. Fig.3 and 4 show how the axial force and stiffness are modified when the axial inner ring position changes for different values of the air gap.
Naturally, when the air gap decreases, the modulus of the axial force for a given axial position of the inner ring increases (except for large displacements) and so does the modulus of the axial stiffness. Furthermore, it has to be noted that a positive stiffness corresponds to a stable configuration in which the force is a pull-back one, whereas a negative stiffness corresponds to an unstable position: the inner ring gets ejected!

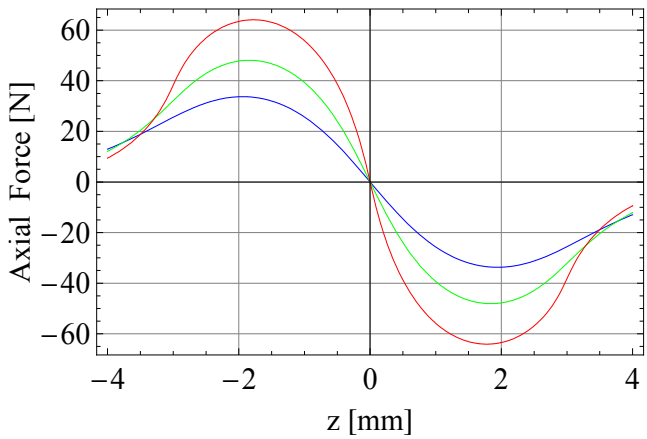

Fig. 3. Axial force for several air gap radial dimensions. Blue: $r_1 = 25mm, r_2 = 28mm, r_3 = 21mm, r_4 = 24mm, h = 3mm$ Air gap $1mm$, Green: Air gap $0.5mm$, Red: Air gap $0.1mm$

4.1.3 Ring height influence

The air gap is kept constant as well as the ring radii and the height of the rings is varied. Fig.5 and 6 show how the axial force and stiffness are modified. When the magnet height decreases, the modulus of the axial force for a given axial position of the inner ring decreases. This is normal, as the magnet volume also decreases.
The study of the stiffness is carried out for decreasing ring heights (Fig.6) but also for increasing ones (Fig.7). As a result, the stiffness doesn't go on increasing in a significant way above a given ring height. This means that increasing the magnet height, and consequently

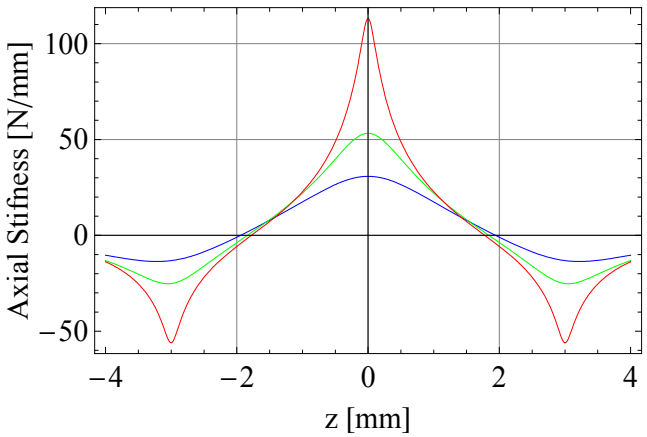

Fig. 4. Axial stiffness for several air gap radial dimensions. Blue: $r_1 = 25mm, r_2 = 28mm, r_3 = 21mm, r_4 = 24mm, h = 3mm$ Air gap $1mm$, Green: Air gap $0.5mm$, Red: Air gap $0.1mm$

the magnet volume, above a given value isn't interesting to increase the stiffness. Moreover, it has to be noted that when the height is reduced by half, from $3mm$ to $1.5mm$, the stiffness is only reduced by a third. This points out that in this configuration, the loss on the stiffness isn't that bad whereas the gain in volume is really interesting. This result will be useful for other kinds of bearing structures -stacked structures- in a further section. Besides, the magnet height shouln't become smaller than the half of its radial thickness unless the demagnetizing field inside the magnet becomes too strong and demagnetizes it.

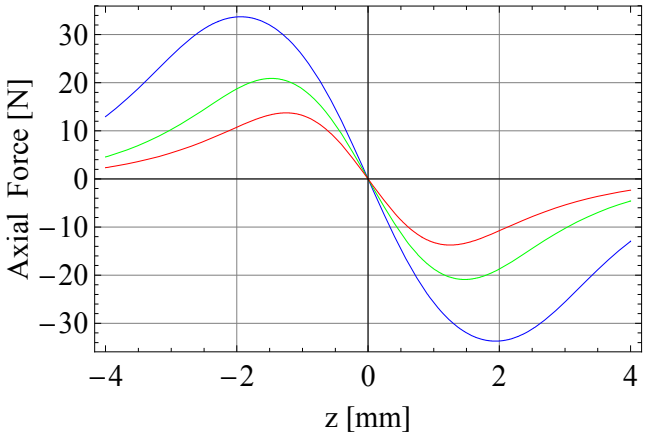

Fig. 5. Axial force for ring small heights. Blue: $r_1 = 25mm, r_2 = 28mm, r_3 = 21mm, r_4 = 24mm$, air gap $1mm$ $h = 3mm$, Green: $h = 2mm$, Red: $h = 1.5mm$.

4.1.4 Ring radial thickness influence

Now, the radial thickness of the ring magnets is varied. The ring height, $h = 3mm$, and the air gap length, $1mm$, are kept constant and the outer radius of the outer ring, r_2, is increased of

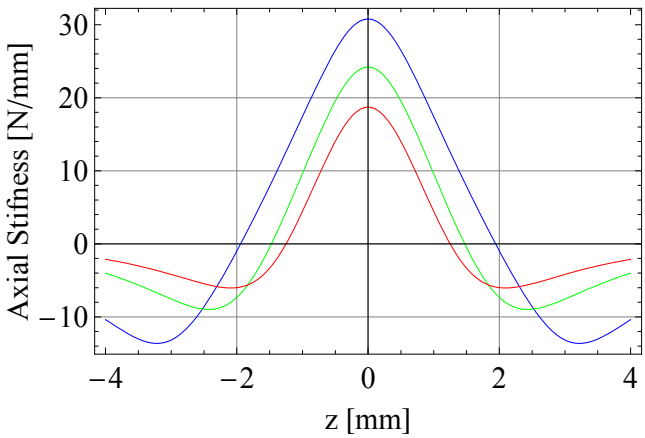

Fig. 6. Axial stiffness for ring small heights. Blue: $r_1 = 25mm, r_2 = 28mm, r_3 = 21mm, r_4 = 24mm$, air gap $1mm$ $h = 3mm$, Green: $h = 2mm$, Red: $h = 1.5mm$.

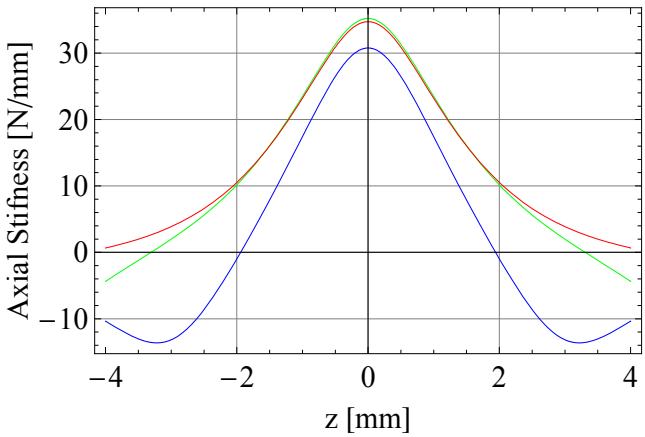

Fig. 7. Axial stiffness for ring large heights. Blue: $r_1 = 25mm, r_2 = 28mm, r_3 = 21mm, r_4 = 24mm$, air gap $1mm$ $h = 3mm$, Green: $h = 6mm$, Red: $h = 9mm$.

the same quantity as the inner radius of the inner ring, r_3, is decreased. So, the inner ring has always the same radial thickness as the outer one.
When the radial thickness increases, the modulus of the axial force for a given axial displacement of the inner ring also increases (Fig.8). This behavior is expected as once again the magnet volume increases. However, the ring thickness doesn't seem a very sensitive parameter. Indeed, the variation isn't as dramatic as with the previous studied parameters.

4.1.5 Ring mean perimeter influence

The outer ring perimeter is varied and all the radii are varied to keep the ring cross section and the air gap constant. As a result, when the device perimeter -or the air gap perimeter- increases, the modulus of the axial force for a given axial displacement of the inner ring also

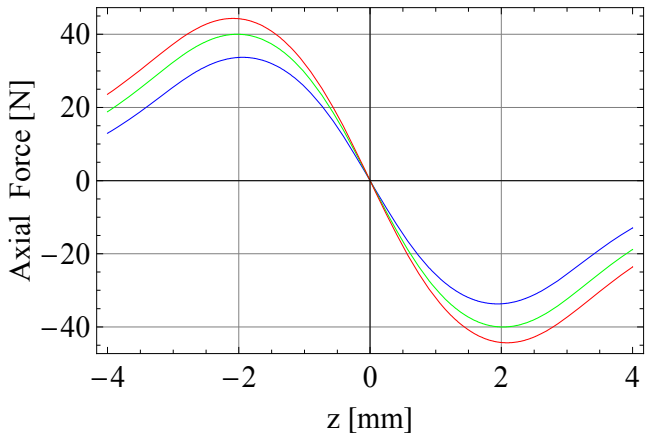

Fig. 8. Axial force for several radial thicknesses. Blue: $r_1 = 25mm, r_2 = 28mm, r_3 = 21mm, r_4 = 24mm$, $h = 3mm$, air gap $1mm$, Radial thickness $r_2 - r_1 = r_4 - r_3 = 3mm$, Green: $4mm$, Red: $5mm$.

increases (Fig.9). This result is expected as the magnet volume also increases.

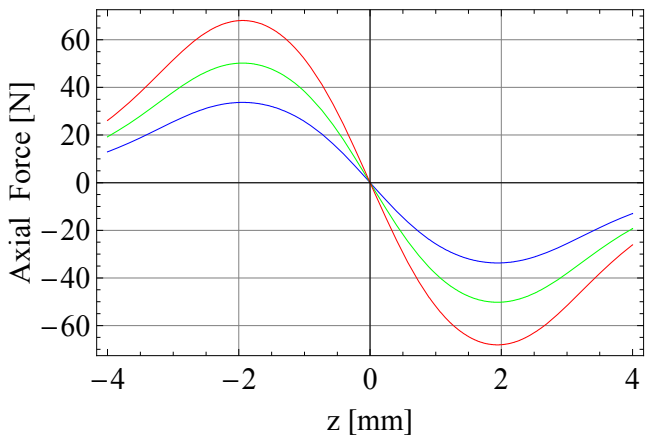

Fig. 9. Axial force for several air gap perimeters. $h = 3mm$, air gap $1mm$. Blue: $r_1 = 25mm, r_2 = 28mm, r_3 = 21mm, r_4 = 24mm$. Green: $r_1 = 37mm, r_2 = 40mm, r_3 = 33mm, r_4 = 36mm$. Red: $r_1 = 50mm, r_2 = 53mm, r_3 = 46mm, r_4 = 49mm$.

4.1.6 Maximum axial force

Previous results are interesting as they show the shape of the axial force and stiffness when different dimensional parameters are varied. Nevertheless, it is necessary to complete these results with additional studies, such as the study of the maximum force for example, in order to compare them. Indeed, a general conclusion is that the axial force increases when the magnet volume increases, but the way it increases depends on the parameter which makes the volume increase.

So, the blue line on Fig.10 shows that the maximum force varies linearly with the air gap diameter. Furthermore, this variation is also linear for radially thicker ring magnets (green and red lines on Fig.10).
As a conclusion, the maximum axial force, and the axial stiffness too, is proportional to the air gap diameter, as long as this diameter isn't too small (which means above 5mm).

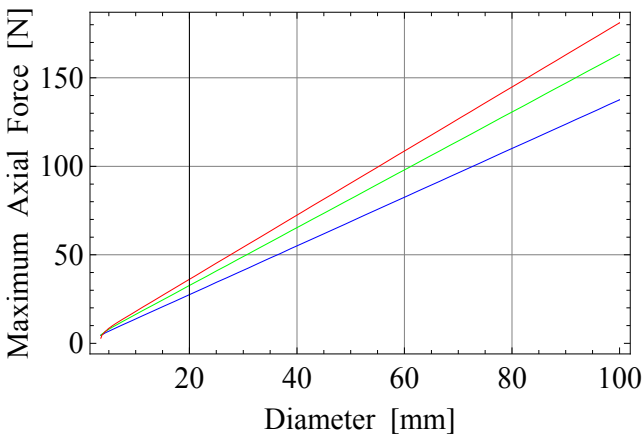

Fig. 10. Maximum axial force versus the air gap perimeter for several ring radial thicknesses. Air gap $1mm$, $h = 3mm$. Blue: $r_1 = 25mm, r_2 = 28mm, r_3 = 21mm, r_4 = 24mm$ Radial thickness $r_2 - r_1 = r_4 - r_3 = 3mm$, Green: Radial thickness $4mm$, Red: Radial thickness $5mm$.

Moreover, the blue line on Fig.11 shows that the maximum force varies inversely to the square of the air gap radial dimension. Thus, the maximum axial force is very sensitive to the air gap radial dimension, which should be as small as possible to have large forces but which is generally set by the mechanical constraints of the device. As a remark, for ring magnets of $3 \times 3mm^2$ cross section, if the radial mechanical air gap has to be $2mm$, the axial force exerted is rather negligible!

4.2 Multiple ring structures: stacked structures

A remark of the previous section will be exploited now. Indeed, the study of the ring height shew that diminishing the magnet height, and thus its volume, could be done without a dramatical decrease of the force. Hence the idea of using rather short rings but of stacking them with alternate polarization directions to achieve larger forces.
For example, let's consider a stack of elementary devices of same dimensions as the previously considered devices: $r_1 = 25mm$, $r_2 = 28mm$, $r_3 = 21mm$, $r_4 = 24mm$, $h = 3mm$, cross section $3 \times 3mm^2$. The bottom of the first device is located at $z = 0$, the bottom of the second one at $z = 3$ and so on (Fig. 12).
Fig.13 shows the axial stiffness for the elementary device (blue), for a stack of two elementary devices (green) and for a stack of three elementary devices (red). The consequence of stacking is that the different axial stiffnesses are additive, as they all act in the same way. So, the total axial stiffness of the device increases more rapidly than the number of stacked devices (Yonnet et al., 1991). Indeed, the maximal stiffness for one ring pair with a square section of $3 \times 3mm^2$ is 30.8 N/mm, for two pairs 87.9 N/mm and for three pairs 140 N/mm. If n is the number of pairs, the stiffness of a stack is approximately $2n - 1$ times greater than the stiffness of a pair.

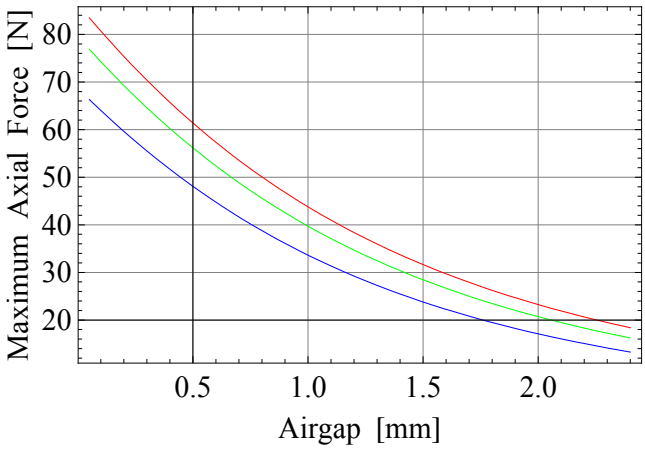

Fig. 11. Maximum axial force versus the air gap radial dimension for several ring radial thicknesses. $h = 3mm$. Blue: $r_1 = 25mm, r_2 = 28mm, r_3 = 21mm, r_4 = 24mm$ Radial thickness $r_2 - r_1 = r_4 - r_3 = 3mm$, Green: Radial thickness $4mm$, Red: Radial thickness $5mm$.

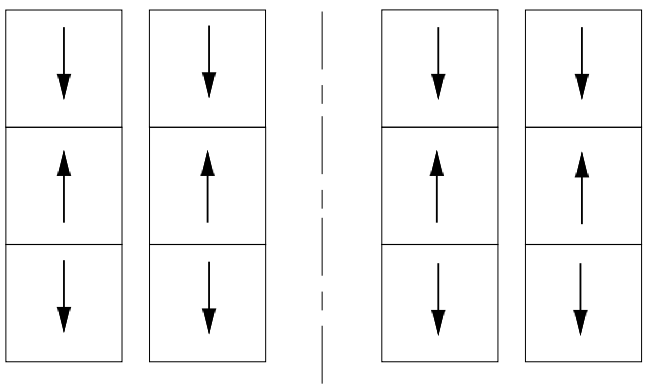

Fig. 12. Cross-section of a stack of three elementary devices with alternate axial polarizations.

Besides, the stiffness obtained for a ring pair of same total dimensions as the stack of three pairs is 34.7 N/mm. This example emphazises the advantage, for a given volume and a sufficient axial height, of splitting the ring into several rings of smaller heights and opposite polarizations: making three pairs increases the stiffness fourfold. The splitting is interesting as long as the height of each ring magnet is large enough (see section 4.1.3).

5. Study and characteristics of axial bearings with axially polarized ring magnets and a plane air gap.

This section considers devices with two axially polarized ring magnets of exactly the same dimensions. They are positioned so as to have the same rotation axis and thus are separated by a plane air gap. In this configuration, if the rings have the same polarization direction, the device works as a radial bearing, if the polarizations are opposite, it works as an axial bearing. It is noticeable that for axial polarizations, parallel polarizations yield

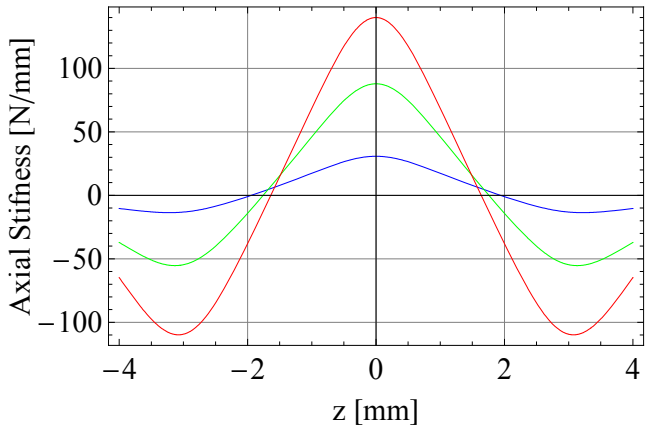

Fig. 13. Axial stiffness for one elementary device (blue), for a stack of two elementary devices (green) and three elementary devices (red).

radial bearings whereas antiparallel polarizations yield axial ones, whatever the air gap shape.

For these structures, the axial displacement of one ring corresponds to an air gap variation. Of course, the maximal axial force between the rings occurs when they are axially in contact with each other. When the air gap, z, increases, the axial force decreases, as show on Fig.15. As the variation is monotonous, the axial stiffness has always the same sign (Fig. 16) and the force the same nature (restoring, here).

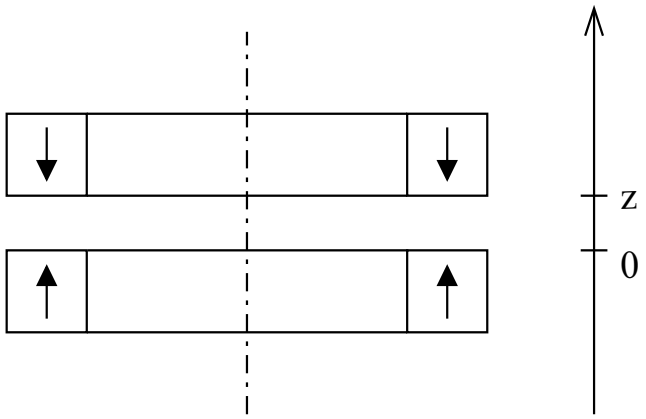

Fig. 14. Cross-section of a bearing with a plane air gap

Moreover, the axial force depends on the size of surfaces which are facing each other. Therefore, it is obvious that when the ring radial thickness increases, the force increases in the same way. The only other interesting parameter is the ring axial height. Figure 17 and 18 show how the axial force and stiffness vary when the air gap changes for different ring axial height. The force doesn't seem to vary greatly when the magnet height changes, and the stiffness even less. But the attention should be drawn to the scale of the force amplitude. Indeed, Fig.19 and 20 show the force and the stiffness for a fixed air gap when the magnet height varies.

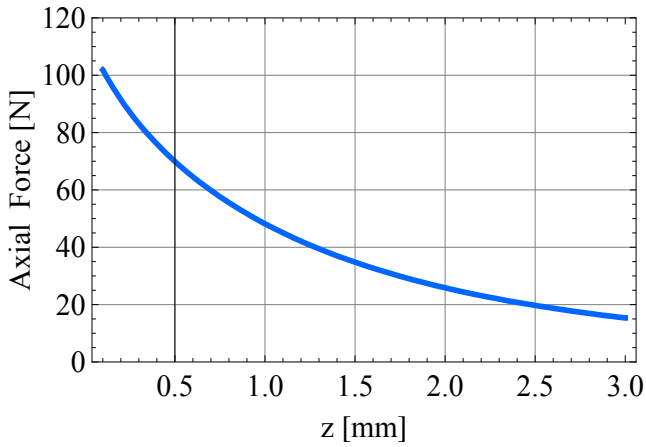

Fig. 15. Axial force when the plane air gap length, z, varies. $r_1 = r_3 = 25mm, r_2 = r_4 = 28mm, h = 3mm$.

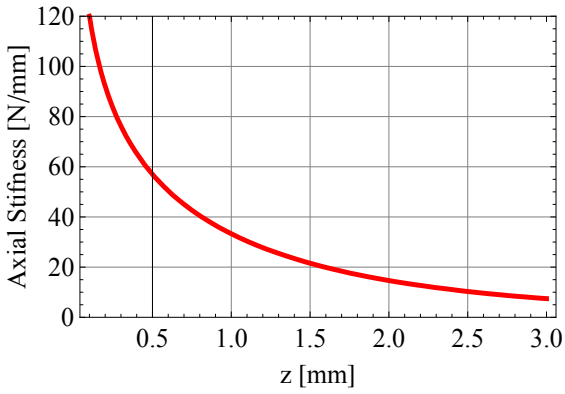

Fig. 16. Axial stiffness when the plane air gap length, z, varies. $r_1 = r_3 = 25mm, r_2 = r_4 = 28mm, h = 3mm$.

They emphazise the fact that increasing the magnet height is interesting for small heights, but becomes rapidly inefficient, especially with regard to the stiffness.

6. Determination of the force transmitted between two radially polarized ring permanent magnets.

The structure considered now is shown in Fig 21. The device is constituted by two concentric ring magnets which are separated by a cylindrical air gap and are radially polarized, their polarizations being in the same direction.

6.1 Notations

The parameters which describe the geometry of Fig.21 and its properties are listed below:
J_1: outer ring polarization [T].
J_2: inner ring polarization [T].

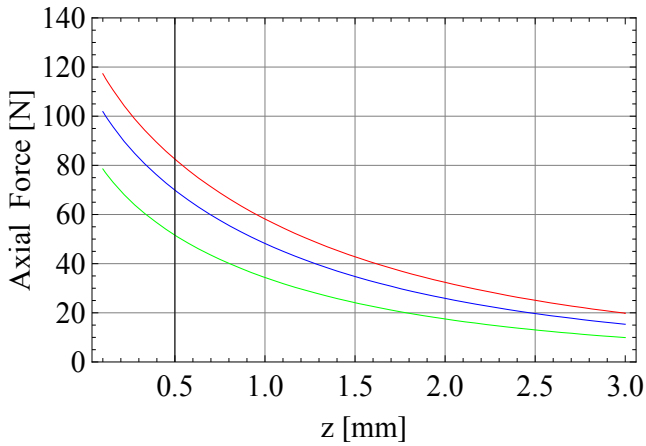

Fig. 17. Axial force when the plane air gap length, z, varies. $r_1 = r_3 = 25mm$, $r_2 = r_4 = 28mm$. Blue: $h = 3mm$, Green: $h = 2mm$, Red: $h = 4mm$.

r_{in}, r_{out}: radial coordinates of the outer ring [m].
r_{in2}, r_{out2}: radial coordinates of the inner ring [m].
h: outer ring height [m].
$z_b - z_a$: inner ring height [m].
The rings are radially centered and their polarizations are supposed to be uniformly radial.

6.2 Magnet modelling

For this kind of configuration, the coulombian model of magnets is the one that gives interesting analytical and semi analytical expressions. Consequently, each ring permanent magnet is represented by two curved planes which correspond to the inner and outer faces of the rings. These faces are charged with a surface magnetic pole density σ^* and the charge balance is reached thanks to a magnetic pole volume density σ_v^*. For each ring, the inner face is charged with the surface magnetic pole density $+\sigma^*$ and the outer one is charged with the surface magnetic pole density $-\sigma^*$. Moreover, all the calculations are carried out with $\sigma^* = \vec{J}.\vec{n} = 1T$ where $\vec{J}$ is the magnetic polarization vector and $\vec{n}$ is the unit normal vector which is directed towards the rotation axis.

6.3 Expression of the force

The axial force exerted between the magnets results of the interaction of all the charge densities. The axial component of the magnetic field produced by the outer ring permanent magnet is H_z. Thus, the axial force F_z can be written as follows:

$$F_z = \int\int_{(S_{in})} H_z \sigma_2^* d\tilde{S} - \int\int_{(S_{out})} H_z \sigma_2^* d\tilde{S} + \int\int\int_{(V)} H_z \frac{\sigma_2^*}{r_2} d\tilde{V} \tag{17}$$

where σ_2^* is the magnetic pole surface density of the inner ring magnet, (S_{in}) is the surface of the inner face of the inner ring permanent magnet, (S_{out}) is the surface of the outer face of the inner ring permanent magnet and (V) is the volume of the inner ring permanent magnet. So,

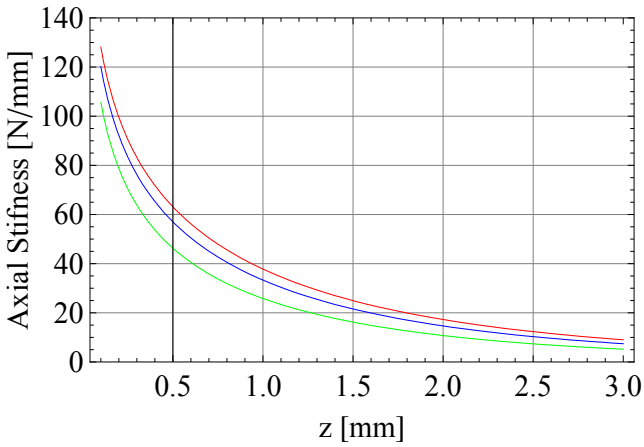

Fig. 18. Axial stiffness when the plane air gap length, z, varies. $r_1 = r_3 = 25mm$,$r_2 = r_4 = 28mm$. Blue: $h = 3mm$, Green: $h = 2mm$, Red: $h = 4mm$.

the axial force F_z can be expressed by:

$$
\begin{aligned}
F_z \quad = \quad & -\int_{\theta_1=0}^{2\pi}\int_{z_1=0}^{h}\int_{\theta_2=0}^{2\pi}\int_{z_2=z_a}^{z_b} a(r_{in}, r_{out2})dz_1 d\theta_1 dz_2 d\theta_2 \\
& +\int_{\theta_1=0}^{2\pi}\int_{z_1=0}^{h}\int_{\theta_2=0}^{2\pi}\int_{z_2=z_a}^{z_b} a(r_{out}, r_{out2})dz_1 d\theta_1 dz_2 d\theta_2 \\
& +\int_{\theta_1=0}^{2\pi}\int_{z_1=0}^{h}\int_{\theta_2=0}^{2\pi}\int_{z_2=z_a}^{z_b} a(r_{in}, r_{in2})dz_1 d\theta_1 dz_2 d\theta_2 \\
& -\int_{\theta_1=0}^{2\pi}\int_{z_1=0}^{h}\int_{\theta_2=0}^{2\pi}\int_{z_2=z_a}^{z_b} a(r_{out}, r_{in2})dz_1 d\theta_1 dz_2 d\theta_2 \\
& -\int_{r_1=r_{in}}^{r_{out}}\int_{\theta_1=0}^{2\pi}\int_{z_1=0}^{h}\int_{\theta_2=0}^{2\pi}\int_{z_2=z_a}^{z_b} b(r_{out2}, r_1)dr_1 dz_1 d\theta_1 dz_2 d\theta_2 \\
& +\int_{r_1=r_{in}}^{r_{out}}\int_{\theta_1=0}^{2\pi}\int_{z_1=0}^{h}\int_{\theta_2=0}^{2\pi}\int_{z_2=z_a}^{z_b} b(r_{in2}, r_1)dr_1 dz_1 d\theta_1 dz_2 d\theta_2 \\
& +\int_{r_2=r_{in2}}^{r_{out2}}\int_{\theta_1=0}^{2\pi}\int_{z_1=0}^{h}\int_{\theta_2=0}^{2\pi}\int_{z_2=z_a}^{z_b} b(r_{in}, r_2)dz_1 d\theta_1 dr_2 dz_2 d\theta_2 \\
& -\int_{r_2=r_{in2}}^{r_{out2}}\int_{\theta_1=0}^{2\pi}\int_{z_1=0}^{h}\int_{\theta_2=0}^{2\pi}\int_{z_2=z_a}^{z_b} b(r_{out}, r_2)dz_1 d\theta_1 dr_2 dz_2 d\theta_2 \\
& +\int_{r_1=r_{in}}^{r_{out}}\int_{r_2=r_{in2}}^{r_{out2}}\int_{\theta_1=0}^{2\pi}\int_{z_1=0}^{h}\int_{\theta_2=0}^{2\pi}\int_{z_2=z_a}^{z_b} c(r_1, r_2)dr_1 dz_1 d\theta_1 dr_2 dz_2 d\theta_2
\end{aligned}
\tag{18}
$$

with

$$
a(\alpha, \beta) = \frac{\sigma_1^* \sigma_2^*}{4\pi\mu_0} \frac{(z_2 - z_1)\alpha\beta}{(\alpha^2 + \beta^2 - 2\alpha\beta + (z_2 - z_1)^2)^{\frac{3}{2}}} \tag{19}
$$

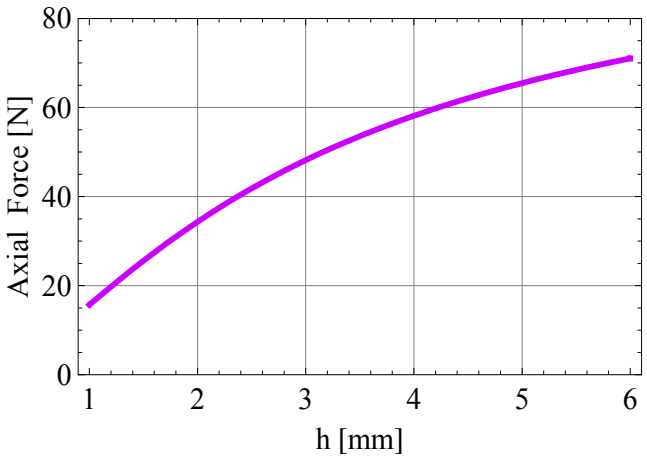

Fig. 19. Axial force when the ring axial height, h, varies. Plane air gap $z = 1mm$, $r_1 = r_3 = 25mm$, $r_2 = r_4 = 28mm$.

where σ_1^* is the magnetic pole surface density of the outer ring magnet. and

$$b(\alpha,\beta) = \frac{a(\alpha,\beta)}{\beta} \tag{20}$$

$$c(\alpha,\beta) = \frac{a(\alpha,\beta)}{\alpha\beta} \tag{21}$$

The next step is to evaluate Eq. (18). Therefore, the number of integrals is first reduced by integrating analytically $a(\alpha,\beta)$, $b(\alpha,\beta)$ and $c(\alpha,\beta)$ according to the integral variables. Unfortunately, a fully analytical expression of the force can't be found but the following semi-analytical expression is quite useful:

$$\begin{aligned} F_z &= \frac{\sigma_1^*\sigma_2^*}{2\mu_0}\int_{\theta_1=0}^{2\pi} S d\theta_1 \\ &+ \frac{\sigma_1^*\sigma_2^*}{2\mu_0}\int_{\theta_1=0}^{2\pi} M d\theta_1 \\ &+ \frac{\sigma_1^*\sigma_2^*}{2\mu_0}\int_{\theta_1=0}^{2\pi}\int_{r_2=r_{in2}}^{r_{out2}} V d\theta_1 dr_2 \end{aligned} \tag{22}$$

where S represents the interaction between the magnetic pole surface densities of each ring magnet, M corresponds to the magnetic interaction between the magnetic pole surface densities of one ring permanent magnet and the magnetic pole volume density of the other one, and V denotes the interaction between the magnetic pole volume densities of each ring permanent magnet.

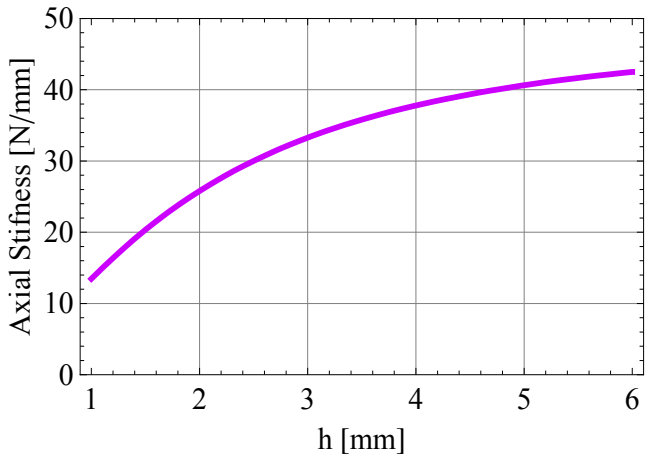

Fig. 20. Axial stiffness when the ring axial height, h, varies. Plane air gap $z = 1mm$, $r_1 = r_3 = 25mm$,$r_2 = r_4 = 28mm$.

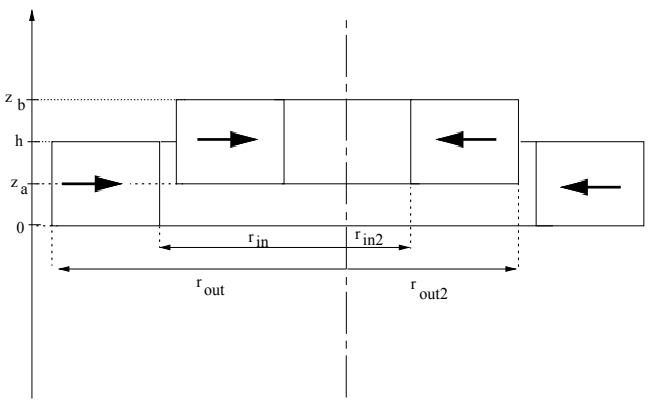

Fig. 21. Radial bearing with radially polarized ring magnets and a cylindrical air gap

The first contribution S is given by (23).

$$\begin{aligned} S \quad = \quad & -f(z_a, z_b, h, \theta_1, r_{in}, r_{out2}) \\ & +f(z_a, z_b, h, \theta_1, r_{out}, r_{out2}) \\ & +f(z_a, z_b, h, \theta_1, r_{in}, r_{in2}) \\ & -f(z_a, z_b, h, \theta_1, r_{out}, r_{in2}) \end{aligned} \tag{23}$$

with

$$\begin{aligned} f(\alpha_1,\alpha_2,\alpha_3,\theta_1,\alpha_5,\alpha_6) &= \alpha_5\alpha_6 \log\left[\alpha_3-\alpha_1+\sqrt{\alpha_5^2+\alpha_6^2+(\alpha_3-\alpha_1)^2-2\alpha_5\alpha_6\cos(\theta_1)}\right] \\ &+\alpha_5\alpha_6 \log\left[\alpha_1+\sqrt{\alpha_5^2+\alpha_6^2+\alpha_1^2-2\alpha_5\alpha_6\cos(\theta_1)}\right] \\ &-\alpha_5\alpha_6 \log\left[\alpha_3-\alpha_2+\sqrt{\alpha_5^2+\alpha_6^2+(\alpha_3-\alpha_2)^2-2\alpha_5\alpha_6\cos(\theta_1)}\right] \\ &-\alpha_5\alpha_6 \log\left[\alpha_2+\sqrt{\alpha_5^2+\alpha_6^2+\alpha_2^2-2\alpha_5\alpha_6\cos(\theta_1)}\right] \end{aligned} \tag{24}$$

The second contribution M is given by (25).

$$\begin{aligned} M &= -t(r_{in},r_{out},r_{out2},h,z_a,z_b,\theta_1) \\ &+t(r_{in},r_{out},r_{in2},h,z_a,z_b,\theta_1) \\ &+t(r_{in},r_{out},r_{in},h,z_a,z_b,\theta_1) \\ &-t(r_{in},r_{out},r_{out},h,z_a,z_b,\theta_1) \end{aligned} \tag{25}$$

with

$$\begin{aligned} t(\beta_1,\beta_2,\beta_3,\beta_4,\beta_5,\beta_6,\theta_1) &= t^{(2)}\left(\beta_1,\beta_2,\beta_4-\beta_5,\beta_3^2+(\beta_4-\beta_5)^2,2\beta_3\cos(\theta_1)\right) \\ &+t^{(2)}\left(\beta_1,\beta_2,\beta_5,\beta_3^2+\beta_5^2,2\beta_3\cos(\theta_1)\right) \\ &-t^{(2)}\left(\beta_1,\beta_2,\beta_4-\beta_6,\beta_3^2+(\beta_4-\beta_6)^2,2\beta_3\cos(\theta_1)\right) \\ &-t^{(2)}\left(\beta_1,\beta_2,\beta_6,\beta_3^2+\beta_6^2,2\beta_3\cos(\theta_1)\right) \end{aligned} \tag{26}$$

and

$$t^{(2)}(\beta_1,\beta_2,q,d,f) = t^{(3)}(\beta_2,q,d,f) - t^{(3)}(\beta_1,q,d,f) \tag{27}$$

and

$$\begin{aligned} t^{(3)}(s,q,d,f) &= -s+\frac{\sqrt{4d-f^2-4q^2}}{2}\arctan\left[\frac{-f+2s}{\sqrt{4d-f^2-4q^2}}\right]-\frac{f}{4}\log\left[d-q^2-fs+s^2\right] \\ &+s\log\left[q+\sqrt{d-fs+s^2}\right]+q\log\left[-f+2(s+\sqrt{d-fs+s^2})\right] \\ &-\frac{\left(4d-f^2-4q^2+f\eta\right)\log[u_1]}{4\eta} \\ &-\frac{\left(-4d+f^2+4q^2+f\eta\right)\log[u_2]}{4\eta} \end{aligned} \tag{28}$$

$$\begin{aligned} u_1 &= -\frac{2\left(f^2+4fq^2-f^2(\eta+2s)+4d(-f+\eta+2s)\right)}{q^2(-4d+f^2+4q^2-f\eta)(-f+\eta+2s)} \\ &\quad -\frac{8q(-2qs+\eta\sqrt{d-fs+s^2})}{q^2(-4d+f^2+4q^2-f\eta)(-f+\eta+2s)} \end{aligned} \tag{29}$$

$$\begin{aligned} u_2 &= -\frac{2\left(f^2+4fq^2-f^2(\eta-2s)-4d(f+\eta-2s)\right)}{q^2(-4d+f^2+4q^2+f\eta)(f+\eta-2s)} \\ &\quad -\frac{-8q(2qs+\eta\sqrt{d-fs+s^2})}{q^2(-4d+f^2+4q^2+f\eta)(f+\eta-2s)} \end{aligned} \tag{30}$$

with

$$\eta = \sqrt{-4d+f^2+4q^2} \tag{31}$$

The third contribution V is given by (32).

$$V = th^{(1)}(r_{out}, r_2, z_a, z_b, h, \theta_1) - th^{(1)}(r_{in}, r_2, z_a, z_b, h, \theta_1) \tag{32}$$

with

$$\begin{aligned} th^{(1)} &= t^{(3)}(r_1, h-z_a, r_2^2+(h-z_a)^2, 2r_2\cos(\theta_1)) \\ &\quad +t^{(3)}(r_1, z_a, r_2^2+z_a^2, 2r_2\cos(\theta_1)) \\ &\quad -t^{(3)}(r_1, h-z_b, r_2^2+(h-z_b)^2, 2r_2\cos(\theta_1)) \\ &\quad -t^{(3)}(r_1, z_b, r_2^2+z_b^2, 2r_2\cos(\theta_1)) \end{aligned} \tag{33}$$

6.4 Expression of the axial stiffness between two radially polarized ring magnets

As previously done, the stiffness K exerted between two ring permanent magnets is determined by calculating the derivative of the axial force with respect to z_a. We set $z_b = z_a + b$ where b is the height of the inner ring permanent magnet. Thus, the axial stiffness K can be calculated with (34).

$$K = -\frac{\partial}{\partial z_a} F_z \tag{34}$$

where F_z is given by (18). We obtain :

$$K = K_S + K_M + K_V \tag{35}$$

where K_S represents the stiffness determined by considering only the magnetic pole surface densities of each ring permanent magnet, K_M corresponds to the stiffness determined with the interaction between the magnetic pole surface densities of one ring permanent magnet and the magnetic pole volume density of the other one, and K_V corresponds to the stiffness determined with the interaction between the magnetic pole volume densities of each ring permanent magnet. Thus, K_S is given by:

$$
\begin{aligned}
K_S = \\
&\eta_{31}\left(\frac{1}{\sqrt{\alpha_{31}}}\mathbf{K}^*\left[-\frac{4r_3r_1}{\alpha_{31}}\right]-\frac{1}{\sqrt{\beta_{31}}}\mathbf{K}^*\left[-\frac{4r_3r_1}{\beta_{31}}\right]+\frac{1}{\sqrt{\delta_{31}}}\mathbf{K}^*\left[-\frac{4r_3r_1}{\delta_{31}}\right]-\frac{1}{\sqrt{\gamma_{31}}}\mathbf{K}^*\left[-\frac{4r_3r_1}{\gamma_{31}}\right]\right)\\
&+\eta_{41}\left(\frac{1}{\sqrt{\alpha_{41}}}\mathbf{K}^*\left[-\frac{4r_4r_1}{\alpha_{41}}\right]-\frac{1}{\sqrt{\beta_{41}}}\mathbf{K}^*\left[-\frac{4r_4r_1}{\beta_{41}}\right]+\frac{1}{\sqrt{\delta_{41}}}\mathbf{K}^*\left[-\frac{4r_4r_1}{\delta_{41}}\right]-\frac{1}{\sqrt{\gamma_{41}}}\mathbf{K}^*\left[-\frac{4r_4r_1}{\gamma_{41}}\right]\right)\\
&+\eta_{32}\left(\frac{1}{\sqrt{\alpha_{32}}}\mathbf{K}^*\left[-\frac{4r_3r_2}{\alpha_{32}}\right]-\frac{1}{\sqrt{\beta_{32}}}\mathbf{K}^*\left[-\frac{4r_3r_2}{\beta_{32}}\right]+\frac{1}{\sqrt{\delta_{32}}}\mathbf{K}^*\left[-\frac{4r_3r_2}{\delta_{32}}\right]-\frac{1}{\sqrt{\gamma_{32}}}\mathbf{K}^*\left[-\frac{4r_3r_2}{\gamma_{32}}\right]\right)\\
&+\eta_{42}\left(\frac{1}{\sqrt{\alpha_{42}}}\mathbf{K}^*\left[-\frac{4r_4r_2}{\alpha_{42}}\right]-\frac{1}{\sqrt{\beta_{42}}}\mathbf{K}^*\left[-\frac{4r_4r_2}{\beta_{42}}\right]+\frac{1}{\sqrt{\delta_{42}}}\mathbf{K}^*\left[-\frac{4r_4r_2}{\delta_{42}}\right]-\frac{1}{\sqrt{\gamma_{42}}}\mathbf{K}^*\left[-\frac{4r_4r_2}{\gamma_{42}}\right]\right)
\end{aligned}
\tag{36}
$$

with

$$\eta_{ij} = \frac{2r_ir_j\sigma^*}{\mu_0} \tag{37}$$

$$\alpha_{ij} = (r_i - r_j)^2 + z_a^2 \tag{38}$$

$$\beta_{ij} = (r_i - r_j)^2 + (z_a + h)^2 \tag{39}$$

$$\gamma_{ij} = (r_i - r_j)^2 + (z_a - h) \tag{40}$$

$$\delta_{ij} = (r_i - r_j)^2 + (b - h)^2 + z_a(2b - 2h + z_a) \tag{41}$$

$$\mathbf{K}^*[m] = \int_0^{\frac{\pi}{2}} \frac{1}{\sqrt{1 - m\sin(\theta)^2}} d\theta \tag{42}$$

The second contribution K_M is given by:

$$K_M = \frac{\sigma_1^*\sigma_2^*}{2\mu_0}\int_{\theta=0}^{2\pi} u d\theta \tag{43}$$

with

$$
\begin{aligned}
u \quad = \quad & f\left(r_{in}, r_{out}, r_{in2}, h, z_a, b, \theta\right)\\
& -f\left(r_{in}, r_{out}, r_{out2}, h, z_a, b, \theta\right)\\
& +f\left(r_{in2}, r_{out2}, r_{in}, h, z_a, b, \theta\right)\\
& -f\left(r_{in2}, r_{out2}, r_{out}, h, z_a, b, \theta\right)
\end{aligned}
\tag{44}
$$

and

$$
\begin{aligned}
f(\alpha,\beta,\gamma,h,z_a,b,\theta) = \\
&-\gamma\log\left[\alpha-\gamma\cos(\theta)+\sqrt{\alpha^2+\gamma^2+z_a^2-2\alpha\gamma\cos(\theta)}\right] \\
&+\gamma\log\left[\alpha-\gamma\cos(\theta)+\sqrt{\alpha^2+\gamma^2+(z_a+b)^2-2\alpha\gamma\cos(\theta)}\right] \\
&+\gamma\log\left[\alpha-\gamma\cos(\theta)+\sqrt{\alpha^2+\gamma^2+(z_a-h)^2-2\alpha\gamma\cos(\theta)}\right] \\
&-\gamma\log\left[\alpha-\gamma\cos(\theta)+\sqrt{\alpha^2+\gamma^2+(b-h)^2+2z_a(b-h)+z_a^2-2\alpha\gamma\cos(\theta)}\right] \\
&+\gamma\log\left[\beta-\gamma\cos(\theta)+\sqrt{\beta^2+\gamma^2+z_a^2-2\alpha\gamma\cos(\theta)}\right] \\
&-\gamma\log\left[\beta-\gamma\cos(\theta)+\sqrt{\beta^2+\gamma^2+(z_a+b)^2-2\alpha\gamma\cos(\theta)}\right] \\
&+\gamma\log\left[\beta-\gamma\cos(\theta)+\sqrt{\beta^2+\gamma^2+(z_a-h)^2-2\alpha\gamma\cos(\theta)}\right] \\
&-\gamma\log\left[\beta-\gamma\cos(\theta)+\sqrt{\beta^2+\gamma^2+(b-h)^2+2z_a(b-h)+z_a^2-2\alpha\gamma\cos(\theta)}\right]
\end{aligned}
\tag{45}
$$

The third contribution K_V is given by:

$$
K_V = \frac{\sigma_1^*\sigma_2^*}{2\mu_0}\int_{\theta=0}^{2\pi}\int_{r_1=r_{in}}^{r_{out}}\delta\, d\theta \tag{46}
$$

with

$$
\begin{aligned}
\delta \quad = \quad & -\log\left[r_{in2}-r_1\cos(\theta)+\sqrt{r_1^2+r_{in2}^2+z_a^2-2r_1r_{in2}\cos(\theta)}\right] \\
&+\log\left[r_{in2}-r_1\cos(\theta)+\sqrt{r_1^2+r_{in2}^2+(z_a+b)^2-2r_1r_{in2}\cos(\theta)}\right] \\
&-\log\left[r_{in2}-r_1\cos(\theta)+\sqrt{r_1^2+r_{in2}^2+(b-h)^2+2bz_a-2hz_a+z_a^2-2r_1r_{in2}\cos(\theta)}\right] \\
&+\log\left[r_{in2}-r_1\cos(\theta)+\sqrt{r_1^2+r_{in2}^2+(z_a-h)^2-2r_1r_{in2}\cos(\theta)}\right] \\
&+\log\left[r_{out2}-r_1\cos(\theta)+\sqrt{r_1^2+r_{out2}^2+z_a^2-2r_1r_{out2}\cos(\theta)}\right] \\
&-\log\left[r_{out2}-r_1\cos(\theta)+\sqrt{r_1^2+r_{out2}^2+(z_a+b)^2-2r_1r_{out2}\cos(\theta)}\right] \\
&-\log\left[r_{out2}-r_1\cos(\theta)+\sqrt{r_1^2+r_{out2}^2+(z_a-h)^2-2r_1r_{out2}\cos(\theta)}\right] \\
&+\log\left[r_{out2}-r_1\cos(\theta)+\sqrt{r_1^2+r_{out2}^2+(b-h)^2+2bz_a-2hz_a+z_a^2-2r_1r_{out2}\cos(\theta)}\right]
\end{aligned}
\tag{47}
$$

As a remark, the expression of the axial stiffness can be determined analytically if the magnetic pole surface densities of each ring only are taken into account, so, if the magnetic pole volume

densities can be neglected. This is possible when the radii of the ring permanent magnets are large enough (Ravaud, Lemarquand, Lemarquand & Depollier, 2009).

7. Study and characteristics of bearings with radially polarized ring magnets.

Radially polarized ring magnets can be used to realize passive bearings, either with a cylindrical air gap or with a plane one. A device with a cylindrical air gap works as an axial bearing when the ring magnets have the same radial polarization direction, whereas it works as a radial one for opposite radial polarizations.
For rings with a square cross-section and radii large enough to neglect the magnetic pole volume densities, the authors shew that the axial force exerted between the magnets as well as the corresponding siffness was the same whatever the polarization direction, axial or radial. For instance, this is illustrated for a radial bearing of following dimensions: $r_{in2} = 0.01$ m, $r_{out2} = 0.02$ m, $r_{in} = 0.03$ m, $r_{out} = 0.04$ m, $z_b - z_a = h = 0.1$ m, $J = 1$ T.
Fig. 22 gives the results obtained for a bearing with radial polarization. These results are to be compared with the ones of Fig. 23 corresponding to axial polarizations.

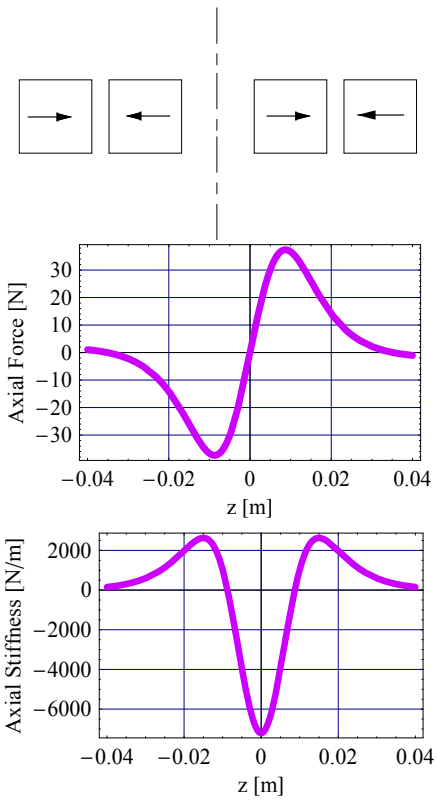

Fig. 22. Axial force and stiffness versus axial displacement for two ring permanent magnets with radial polarizations; $r_1 = 0.01$ m, $r_2 = 0.02$ m, $r_3 = 0.03$ m, $r_4 = 0.04$ m, $z_2 - z_1 = z_4 - z_3 = 0.1$ m, $J = 1$ T

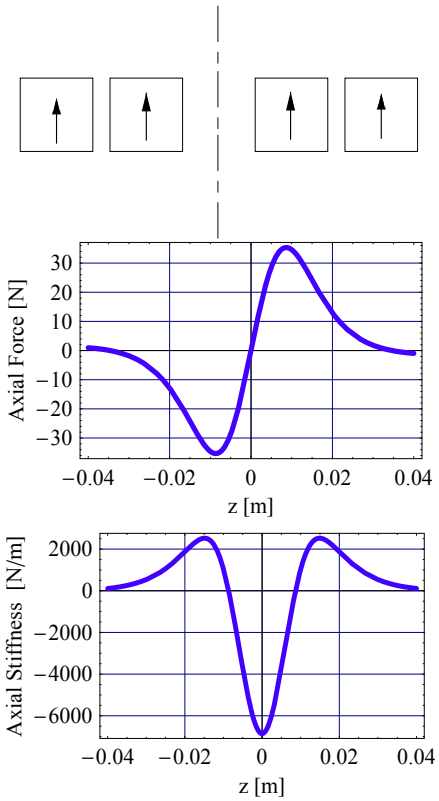

Fig. 23. Axial force and stiffness versus axial displacement for two ring permanent magnets with axial polarizations; $r_1 = 0.01$ m, $r_2 = 0.02$ m, $r_3 = 0.03$ m, $r_4 = 0.04$ m, $z_2 - z_1 = z_4 - z_3 = 0.1$ m, $J = 1$ T

These figures show clearly that the performances are the same. Indeed, for the radial polarizations the maximal axial force exerted by the outer ring on the inner one is 37.4 N and the maximal axial stiffness is $|K_z| = 7205$ N/m and for the axial polarizations the maximal axial force exerted by the outer ring on the inner one is 35.3 N and the maximal axial stiffness is $|K_z| = 6854$ N/m.
Moreover, the same kind of results is obtained when radially polarized ring magnets with alternate polarizations are stacked: the performances are the same as for axially polarized stacked rings.
So, as the radial polarization is far more difficult to realize than the axial one, these calculations show that it isn't interesting from a practical point of view to use radially polarized ring magnets to build bearings.
Nevertheless, this conclusion will be moderated by the next section. Indeed, the use of "mixed" polarization directions in a device leads to very interesting results.

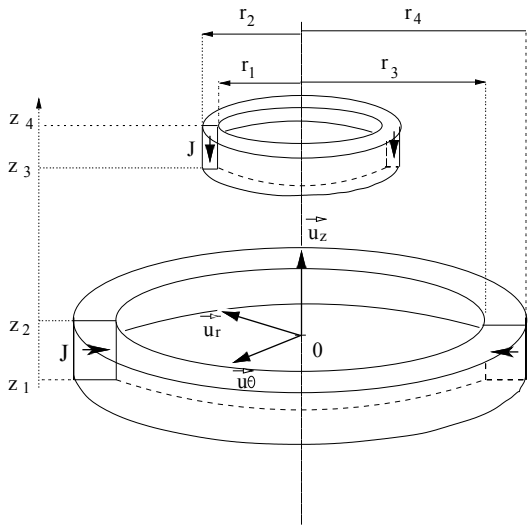

Fig. 24. Ring permanent magnets with perpendicular polarizations.

8. Determination of the force exerted between two ring permanent magnets with perpendicular polarizations

The geometry considered is shown in Fig. 24: two concentric ring magnets separated by a cylindrical air gap. The outer ring is radially polarized and the inner one is axially polarized, hence the reference to "perpendicular" polarization.

8.1 Notations

The following parameters are used:
r_1, r_2: inner and outer radius of the inner ring permanent magnet [m]
r_3, r_4: inner and outer radius of the outer ring permanent magnet [m]
z_1, z_2: lower and upper axial abscissa of the inner ring permanent magnet [m]
z_3, z_4: inner and outer axial abscissa of the outer ring permanent magnet [m]
The two ring permanent magnets are radially centered and their polarization are supposed uniformly radial.

8.2 Magnet modelling

The coulombian model is chosen for the magnets. So, each ring permanent magnet is represented by faces charged with fictitious magnetic pole surface densities. The outer ring permanent magnet which is radially polarized is modelled as in the previous section. The outer face is charged with the fictitious magnetic pole surface density $-\sigma^*$ and the inner one is charged with the fictitious magnetic pole surface density $+\sigma^*$. Both faces are cylindrical. Moreover, the contribution of the magnetic pole volume density will be neglected for simplifying the calculations.
The faces of the inner ring permanent magnet which is axially polarized are plane ones: the upper face is charged with the fictitious magnetic pole surface density $-\sigma^*$ and the lower one

is charged with the fictitious magnetic pole surface density $+\sigma^*$. All the illustrative calculations are done with $\sigma^* = \vec{J}.\vec{n} = 1$ T, where $\vec{J}$ is the magnetic polarization vector and $\vec{n}$ is the unit normal vector.

8.3 Force calculation

The axial force exerted between the two magnets with perpendicular polarizations can be determined by:

$$\begin{aligned} F_z &= \frac{J^2}{4\pi\mu_0}\int_{r_1}^{r_2}\int_0^{2\pi} H_z(r,z_3)rdrd\theta \\ &\quad -\frac{J^2}{4\pi\mu_0}\int_{r_1}^{r_2}\int_0^{2\pi} H_z(r,z_4)rdrd\theta \end{aligned} \tag{46}$$

where $H_z(r,z)$ is the axial magnetic field produced by the outer ring permanent magnet. This axial field can be expressed as follows:

$$\begin{aligned} H_z(r,z) &= \frac{J}{4\pi\mu_0}\int\int_S \frac{(z-\tilde{z})}{R(r_3,\tilde{\theta},\tilde{z})}r_3 d\tilde{\theta}d\tilde{z} \\ &\quad -\frac{J}{4\pi\mu_0}\int\int_S \frac{(z-\tilde{z})}{R(r_4,\tilde{\theta},\tilde{z})}r_4 d\tilde{\theta}d\tilde{z} \end{aligned} \tag{45}$$

with

$$R(r_i,\tilde{\theta},\tilde{z}) = \left(r^2 + r_i^2 - 2rr_i\cos(\tilde{\theta}) + (z-\tilde{z})^2\right)^{\frac{3}{2}} \tag{45}$$

The expression of the force can be reduced to:

$$\begin{aligned} F_z &= \frac{J^2}{4\pi\mu_0}\sum_{i,k=1}^{2}\sum_{j,l=3}^{4}(-1)^{i+j+k+l}\left(A_{i,j,k,l}\right) \\ &\quad +\frac{J^2}{4\pi\mu_0}\sum_{i,k=1}^{2}\sum_{j,l=3}^{4}(-1)^{i+j+k+l}\left(S_{i,j,k,l}\right) \end{aligned} \tag{44}$$

with

$$\begin{aligned} A_{i,j,k,l} &= -8\pi r_i \epsilon \mathbf{E}\left[-\frac{4r_i r_j}{\epsilon}\right] \\ S_{i,j,k,l} &= -2\pi r_j^2\int_0^{2\pi}\cos(\theta)\ln\left[\beta+\alpha\right]d\theta \end{aligned} \tag{43}$$

where $\mathbf{E}\left[m\right]$ gives the complete elliptic integral which is expressed as follows:

$$\mathbf{E}\left[m\right] = \int_0^{\frac{\pi}{2}}\sqrt{1-m\sin(\theta)^2}d\theta \tag{43}$$

The parameters ϵ, α and β depend on the ring permanent magnet dimensions and are defined by:

$$\begin{aligned} \epsilon &= (r_i - r_j)^2 + (z_k - z_l)^2 \\ \alpha &= \sqrt{r_i^2 + r_j^2 - 2 r_i r_j \cos(\theta) + (z_k - z_l)^2} \\ \beta &= r_i - r_j \cos(\theta) \end{aligned} \tag{41}$$

8.4 Stiffness exerted between two ring permanent magnets with perpendicular polarizations

The axial stiffness derives from the axial force:

$$K_z = -\frac{d}{dz} F_z \tag{41}$$

where F_z is determined with $R(r_i, \tilde{\theta}, \tilde{z})$ and Eq. (46). After mathematical manipulations, the previous expression can be reduced in the following form:

$$K_z = \frac{J^2}{4\pi\mu_0} \sum_{i,k=1}^{2} \sum_{j,l=3}^{4} (-1)^{i+j+k+l} \left(k_{i,j,k,l} \right) \tag{41}$$

with

$$k_{i,j,k,l} = -\int_0^{2\pi} \frac{r_j (z_k - z_l)(\alpha + r_i)}{\alpha\,(\alpha + \beta)} d\theta \tag{41}$$

9. Study and characteristics of bearings using ring magnets with perpendicular polarizations.

9.1 Structures with two ring magnets

The axial force and stiffness are calculated for the bearing constituted by an outer radially polarized ring magnet and an inner axially polarized one. The device dimensions are the same as in section 7. Thus, the results obtained for this bearing and shown in Fig. 25 are easily compared to the previous ones: the maximal axial force is 39.7 N and the maximal axial stiffness is $|K_z| = 4925$ N/m.

So, the previous calculations show that the greatest axial force is obtained in the bearing using ring permanent magnets with perpendicular polarizations whereas the greatest axial stiffness is obtained in the one using ring permanent magnets with radial polarizations.

9.2 Multiple ring structures: stacks forming Halbach patterns

The conclusion of the preceding section naturally leads to mixed structures which would have both advantages of a great force and a great stiffness. This is achieved with bearings constituted of stacked ring magnets forming a Halbach pattern (Halbach, 1980).

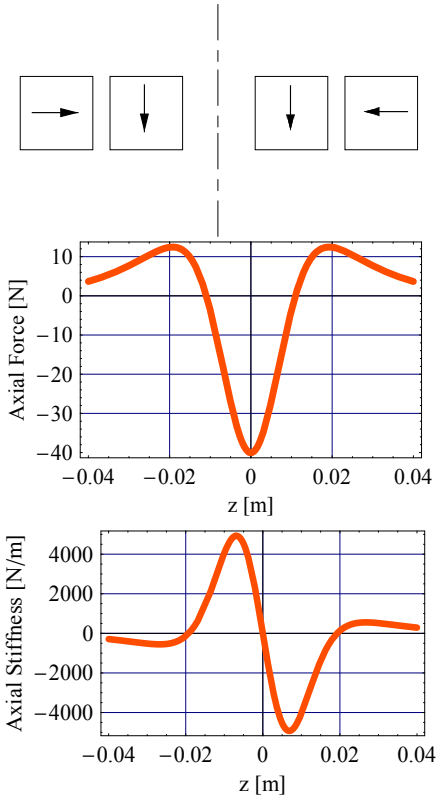

Fig. 25. Axial force axial stiffness versus axial displacement for two ring permanent magnets with perpendicular polarizations; $r_1 = 0.01$ m, $r_2 = 0.02$ m, $r_3 = 0.03$ m, $r_4 = 0.04$ m, $z_2 - z_1 = z_4 - z_3 = 0.1$ m, $J = 1$ T

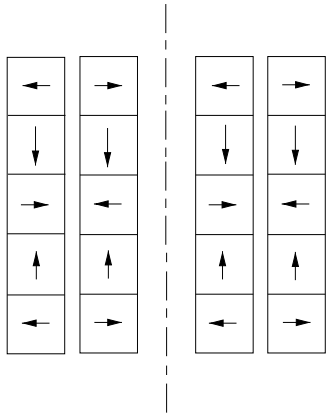

Fig. 26. Cross-section of a stack of five ring permanent magnets with perpendicular polarizations; $r_1 = 0.01$ m, $r_2 = 0.02$ m, $r_3 = 0.03$ m, $r_4 = 0.04$ m, $J = 1$ T, height of each ring permanent magnet = 0.01 m

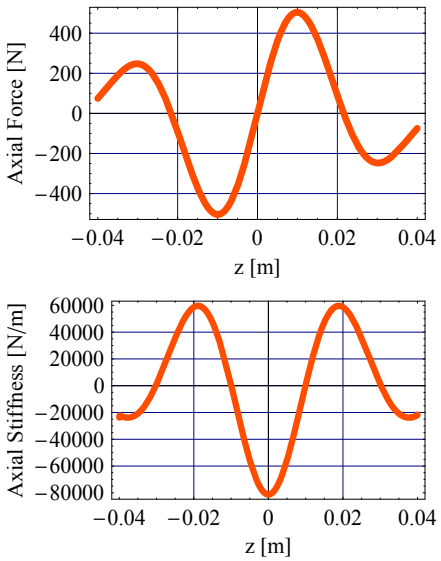

Fig. 27. Axial force and stiffness versus axial displacement for a stack of five ring permanent magnets with perpendicular polarizations; $r_1 = 0.01$ m, $r_2 = 0.02$ m, $r_3 = 0.03$ m, $r_4 = 0.04$ m, $J = 1$ T, height of each ring permanent magnet = 0.01 m

Section 4.2 shew that stacking ring magnets with alternate polarization led to structures with higher performances than the ones with two magnets for a given magnet volume. So, the performances will be compared for stacked structures, either with alternate radial polarizations or with perpendicular ones.
Thus, the bearing considered is constituted of five ring magnets with polarizations alternately radial and axial (Fig. 26). The axial force and stiffness are calculated with the previously presented formulations (Fig.27).
The same calculations are carried out for a stack of five rings with radial alternate polarizations having the same dimensions (Fig. 28). It is to be noted that the result would be the same for a stack of five rings with axial alternate polarizations of same dimensions.
As a result, the maximal axial force exerted in the case of alternate magnetizations is 122 N whereas it reaches 503 N with a Halbach configuration. Moreover, the maximal axial stiffness is $|K_z| = 34505$ N/m for alternate polarizations and $|K_z| = 81242$ N/m for the perpendicular ones. Thus, the force is increased fourfold and the stiffness twofold in the Halbah structure when compared to the alternate one. Consequently, bearings constituted of stacked rings with perpendicular polarizations are far more efficient than those with alternate polarizations. This shows that for a given magnet volume these Halbach pattern structures are the ones that give the greatest axial force and stiffness. So, this can be a good reason to use radially polarized ring magnets in passive magnetic bearings.

10. Conclusion

This chapter presents structures of passive permanent magnet bearings. From the simplest bearing with two axially polarized ring magnets to the more complicated one with stacked rings having perpendicular polarizations, the structures are described and studied. Indeed,

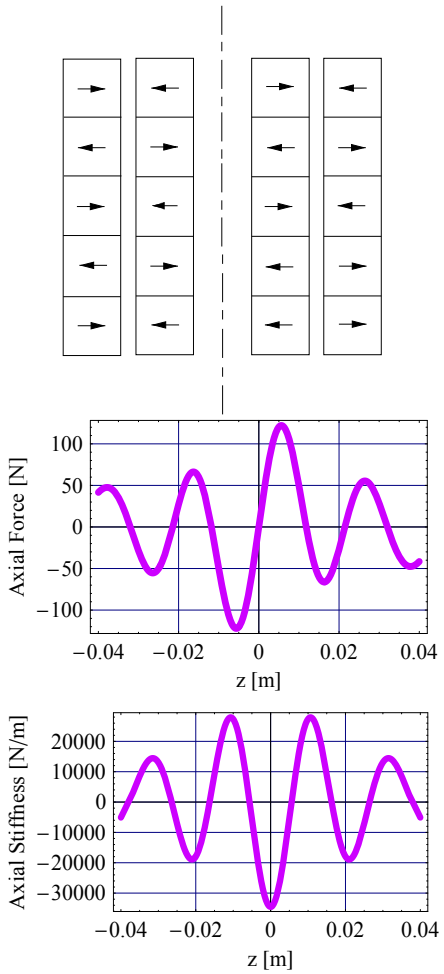

Fig. 28. Axial force and stiffness versus axial displacement for a stack of five ring permanent magnets with radial polarizations; $r_1 = 0.01$ m, $r_2 = 0.02$ m, $r_3 = 0.03$ m, $r_4 = 0.04$ m, $J = 1$ T, height of each ring permanent magnet = 0.01 m

analytical formulations for the axial force and stiffness are given for each case of axial, radial or perpendicular polarization. Moreover, it is to be noted that Mathematica Files containing the expressions presented in this paper are freely available online (*http://www.univ-lemans.fr/∼glemar*, n.d.). These expressions allow the quantitative study and the comparison of the devices, as well as their optimization and have a very low computational cost. So, the calculations show that a stacked structure of "small" magnets is more efficient than a structure with two "large" magnets, for a given magnet volume. Moreover, the use of radially polarized magnets, which are difficult to realize, doesn't lead to real advantages unless it is done in association with axially polarized magnets to build Halbach pattern. In this last case, the bearing obtained has the best performances of all the structures for a given magnet volume.

Eventually, the final choice will depend on the intended performances, dimensions and cost and the expressions of the force and stiffness are useful tools to help the choice.

11. References

Azukizawa, T., Yamamoto, S. & Matsuo, N. (2008). Feasibility study of a passive magnetic bearing using the ring shaped permanent magnets, *IEEE Trans. Magn.* **44**(11): 4277–4280.

Azzerboni, B. & Cardelli, E. (1993). Magnetic field evaluation for disk conductors, *IEEE Trans. Magn.* **29**(6): 2419–2421.

Babic, S. I. & Akyel, C. (2008a). Improvement in the analytical calculation of the magnetic field produced by permanent magnet rings, *Prog. Electromagn. Res. C* **5**: 71–82.

Babic, S. I. & Akyel, C. (2008b). Magnetic force calculation between thin coaxial circular coils in air, *IEEE Trans. Magn.* **44**(4): 445–452.

Barthod, C. & Lemarquand, G. (1995). Degrees of freedom control of a magnetically levitated rotor, *IEEE Trans. Magn.* **31**(6): 4202–4204.

Durand, E. (1968). *Magnetostatique*, Masson Editeur, Paris, France.

Filatov, A. & Maslen, E. (2001). Passive magnetic bearing for flywheel energy storage systems, *IEEE Trans. Magn.* **37**(6): 3913–3924.

Halbach, K. (1980). Design of permanent multiple magnets with oriented rec material, *Nucl. Inst. Meth.* **169**: 1–10.

Hijikata, K., Takemoto, M., Ogasawara, S., Chiba, A. & Fukao, T. (2009). Behavior of a novel thrust magnetic bearing with a cylindrical rotor on high speed rotation, *IEEE Trans. Magn.* **45**(10): 4617–4620.

Holmes, F. T. & Beams, J. W. (1937). Frictionnal torque of an axial magnetic suspension, *Nature* **140**: 30–31.

http://www.univ-lemans.fr/∼glemar (n.d.).

Hussien, A. A., Yamada, S., Iwahara, M., Okada, T. & Ohji, T. (2005). Application of the repulsive-type magnetic bearing for manufacturing micromass measurement balance equipment, *IEEE Trans. Magn.* **41**(10): 3802–3804.

Janssen, J., Paulides, J., Compter, J. & Lomonova, E. (2010). Threee-dimensional analytical calculation of the torque between permanent magnets in magnetic bearings, *IEEE Trans. Mag.* **46**(6): 1748–1751.

Kim, K., Levi, E., Zabar, Z. & Birenbaum, L. (1997). Mutual inductance of noncoaxial circular coils with constant current density, *IEEE Trans. Magn.* **33**(5): 4303–4309.

Lang, M. (2002). Fast calculation method for the forces and stiffnesses of permanent-magnet bearings, *8th International Symposium on Magnetic Bearing* pp. 533–537.

Lemarquand, G. & Yonnet, J. (1998). A partially passive magnetic suspension for a discoidal wheel., *J. Appl. Phys.* **64**(10): 5997–5999.

Meeks, C. (1974). Magnetic bearings, optimum design and applications, *First workshop on RE-Co permanent magnets, Dayton*.

Mukhopadhyay, S. C., Donaldson, J., Sengupta, G., Yamada, S., Chakraborty, C. & Kacprzak, D. (2003). Fabrication of a repulsive-type magnetic bearing using a novel arrangement of permanent magnets for vertical-rotor suspension, *IEEE Trans. Magn.* **39**(5): 3220–3222.

Ravaud, R., Lemarquand, G. & Lemarquand, V. (2009a). Force and stiffness of passive magnetic bearings using permanent magnets. part 1: axial magnetization, *IEEE Trans. Magn.* **45**(7): 2996–3002.

Ravaud, R., Lemarquand, G. & Lemarquand, V. (2009b). Force and stiffness of passive magnetic bearings using permanent magnets. part 2: radial magnetization, *IEEE Trans. Magn.* **45**(9): 3334–3342.

Ravaud, R., Lemarquand, G., Lemarquand, V. & Depollier, C. (2008). Analytical calculation of the magnetic field created by permanent-magnet rings, *IEEE Trans. Magn.* **44**(8): 1982–1989.

Ravaud, R., Lemarquand, G., Lemarquand, V. & Depollier, C. (2009). Discussion about the analytical calculation of the magnetic field created by permanent magnets., *Prog. Electromagn. Res. B* **11**: 281–297.

Samanta, P. & Hirani, H. (2008). Magnetic bearing configurations: Theoretical and experimental studies, *IEEE Trans. Magn.* **44**(2): 292–300.

Yonnet, J. P. (1978). Passive magnetic bearings with permanent magnets, *IEEE Trans. Magn.* **14**(5): 803–805.

Yonnet, J. P., Lemarquand, G., Hemmerlin, S. & Rulliere, E. (1991). Stacked structures of passive magnetic bearings, *J. Appl. Phys.* **70**(10): 6633–6635.

6

A rotor model with two gradient static field shafts and a bulk twined heads system

Hitoshi Ozaku
Railway Technical Research Institute
Japan

1. Introduction

The noncontact high speed rotor is one of dream for many engineers. There are many investigations. At example, one is the bearing less motor, another is flywheel using the bulk high temperature superconducting (HTS). The bearing less motor is needed the high technical knowledge and the accurate system. HTS materials are effectively utilized to the flywheel which needs the grater levitation force, to the motor of the ship which needs the grater torque, and to the motor for the airplane which needs the grater torque and smaller weight. It is very difficult that the rotor of the micro size type generator generates a high power which rotating in a high speed.

Fig. 1. View of the original rotor model in 2007

As my first try in 2006, a small generator in which only one HTS bulk (47mm in diameter) was arranged was tested for the levitation force, but it was useless as the synchronous generator because of being unstable. And an axial gap type rotor improved to a new rotor with two gradient static field shafts which is lifted between a set of the magnets and a trapped static magnetic field of a HTS bulk. Furthermore, the improved rotor was so

rearranged as to form a twin type combination of two bulks and two set of magnets components (Figure 1). The concept of magnetic shafts which plays a role of the twined the magnetic bearing was presented, and acts as magnetic spring.
For achieve the system which achieve the more convenient and continuously examinations without use of liquid nitrogen, we fabricated bulk twined heads type pulse tube cryocooler based on the above experimental.
And, I reported [1] that this system recorded at 2,000 rpm. Later, the improved system and rotor recorded at 15,000 rpm.

2. System

2.1 Rotor model with two gradient static field shafts

The rotor is 70mm in diameter, 70mm in height, and consists of many size acrylic pipes of various sizes. A set of the combined magnets consist of both a cylindrical magnet, 20mm in diameter, 10mm in thickness, and 0.45T, and the two ring magnets, 30mm in inside diameter, 50mm in outside diameter, 5mm in thickness, and 0.33T. The cylindrical magnet was arranged to be the opposite pole in the centre of a ring magnet. The dissembled drawing of the rotor is shown in figure 2. The detail of the structure of the rotor is shown in figure 3. The centre ring part of the rotor is rotary mechanism part, and it can change easily another differ type ring.
The magnetic distribution of a set of the magnets of the rotor measured by the Hall generator with gap 0.5mm is shown in figure 4. In advance the trapped field distribution of the supplied HTS bulk was measured with Hall generator at 0.5mm above the surface of the bulk at over 1.5T field cooling. The peak value was at 0.9T. The relationship of the distributions between the magnetic distribution of the rotor and the magnetic distribution of a HTS bulk trapped in field cooling using liquid nitrogen by the permanent magnets of the rotor is shown in figure 5. The shown values of the magnetic flux density of a HTS bulk in figure 5 were reverse pole. The magnetic distributions of the both poles of the magnets of the rotary mechanism part (8 poles, acrylic ring, in figure 3 and 9) of the rotor were shown in figure 6. The x-axis is shown at vertical direction, and 0 point in x-axis is shown the hole position the acrylic ring of the rotary mechanism part of the rotor.

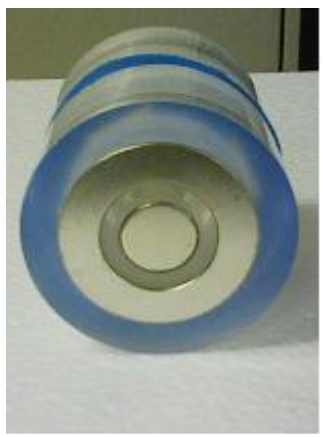

Fig. 2. View of the rotor model

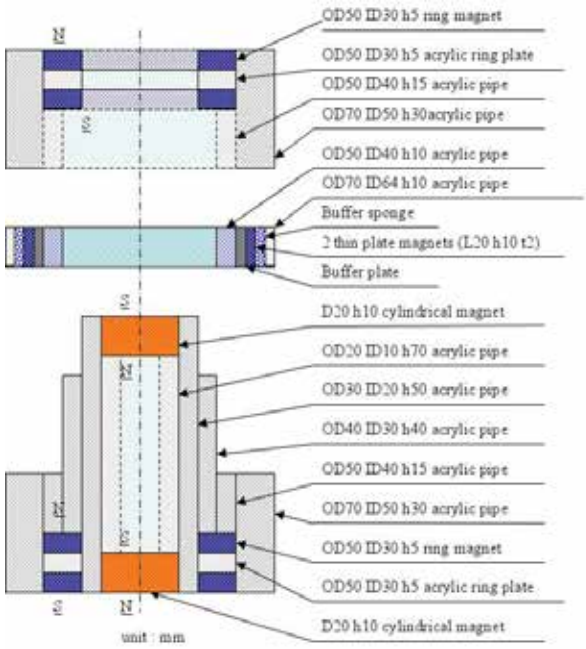

Fig. 3. Detail of component of the rotor model

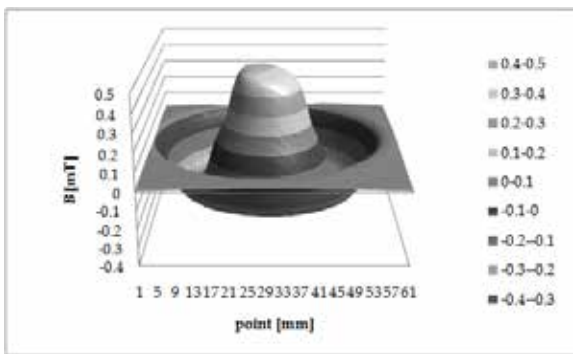

Fig. 4. Magnetic distribution of a set the component of the permanent magnets of the rotor

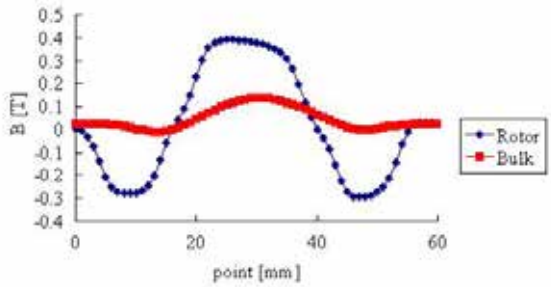

Fig. 5. Magnetic flux density of a set the component of the permanent magnets of the rotor and a trapped HTS bulk

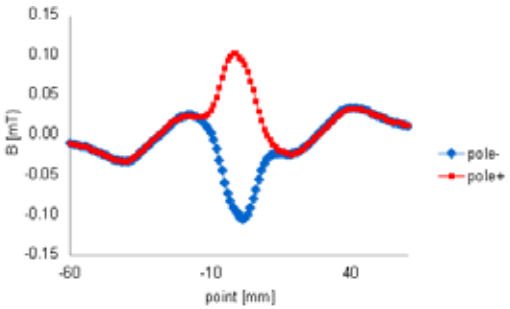

Fig. 6. Magnetic flux density of a rotary mechanism part of the rotor model

2.2 Bulk twined heads pulse tube cryocooler

We improved a pulse tube cryocooler (SPR-05, AISIN SEIKI CO., LTD.). Namely, the two bulks were installed on the boxes of a head part (Thermal Block CO., LTD.) of a pulse tube cryocooler. Figure 7 shows the schematic design of the bulk twined heads pulse tube cryocooler. The rotor explained above was set between the bulk twined heads of this cryocooler. The frost did not occur at the surface of this head in the air because the insulated space in the head was in vacuum condition, and the cold HTS bulk insulated the head. This condition was able to rotate the rotor in the air. Two sensors monitored the temperature condition. One sensor (sensor1) monitored the temperature of the cold head of the pulse tube cryocooler, and the second sensor (sensor2) monitored the temperature of the copper holder which inserted the HTS bulk in the upper head of two heads of the bulk twined heads device. Figure 8 shows efficiency of the cooler device.

After I reported [1], I tried two improvements to this device. One was that an acrylic board (W300, L300mm) with two square holes were as the sections of the top of the heads of this device, sat the bottom of the head of this device. Other improvement was that the distance between the heads of this device was expanded a few millimetres. These improvements were a key of successful to break through the unstable rotation at about 2,000 rpm. The former was because that the board cut the affect of the turbulence of the promotion gas based on the uneven face of this device. The latter was because that a point of inflexion of the relationship line between the vertical force and the vertical distance at an experiment using a HTS bulk and a permanent magnet [2].

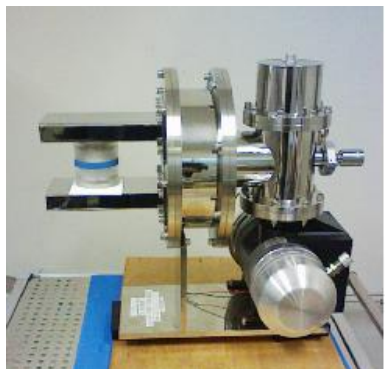

Fig. 7. The bulk twined heads pulse tube cryocooler

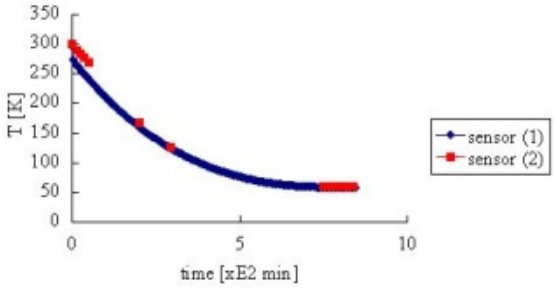

Fig. 8. The relationship between temperature of the cyocooler and time

2.3 Rotation and Measurement system

Rotation of the rotor was occurred that flow of air of the nozzles hit the wall of the holes of the rotary mechanism part of the rotor. The power generation based on action between the permanent magnets in the rotary mechanism part and the coils was used for purpose of to measurement the frequency of the rotor.

In 2007 the nozzles (1/4in, 50-100mm, stainless pipe) were connected to a nitrogen gas cylinder with silicon tubes (OD =6mm, ID =4mm). The branch of the middle from a nitrogen cylinder went in a Y-shaped joint tube (a product made in polypropylene: pp). After a nozzle was consist of a pp tube (L=48mm, ID=3mm), a pp joint (L=43mm, ID=2.5mm), a stainless steel pipe (1/4in, 300mm) (Figure 9). The nozzles were connected to an air compressor (EC1443H, Hitachi KokI Co., Ltd.) with stainless pipes (1/4in, 300mm) and silicon tube (OD =6mm, ID =4mm).and T-shaped

The frequency of the rotation was measure by the two coils connected each to the measuring instruments. There were three type coils, I-shaped coil, U-shaped coil, and T-shaped coil.

The core of the coil was used one or some pieces of the permalloy (a permalloy is alloy between iron and nickel: permability+alloy). The wire of the coil was used to having wound up copper wire OD=0.5mm. The I-shaped coil was used with core which one plate 5mm wide and 10mm long and the wire about 2m long. U-shaped and T-shaped coils were used with core which some plates 10mm wide and 50mm long and the wire about 300mm.

Centre of outer of the U-shaped and T-shaped coil fixed to the end of a stainless steel pipe (1/4in, 300mm) with the polyimide tape.

One coil of the two coils connected to a multi-meter (Type-VOAC7523, IWATSU TEST INSTRUMENTS CORPORATION) connected a PC, other coil connected to a digital oscilloscope (Type-DS-5110, IWATSU TEST INSTRUMENTS CORPORATION), stored the pulse of a coil as USB data by manual operation. The small I-shaped coil of the figure 10 was used without the U-shaped coils for confirmation of that the U-shaped coils were a little related to the rotation of the rotor.

The two nozzles were also placed by the both sides of the rotor, with the direction of the nozzles in perpendicular to the outer surface of the rotor. The U-shaped coils arranged it facing the nozzles and 90 degrees corner (in figure 9 and 10).

The states of rotation tests were taken by a video camera (Type-SR11, Sony Corporation).

The magnetic flux densities were measured by a gauss meter (Type-421, Lakeshore Cryotronics Inc.).

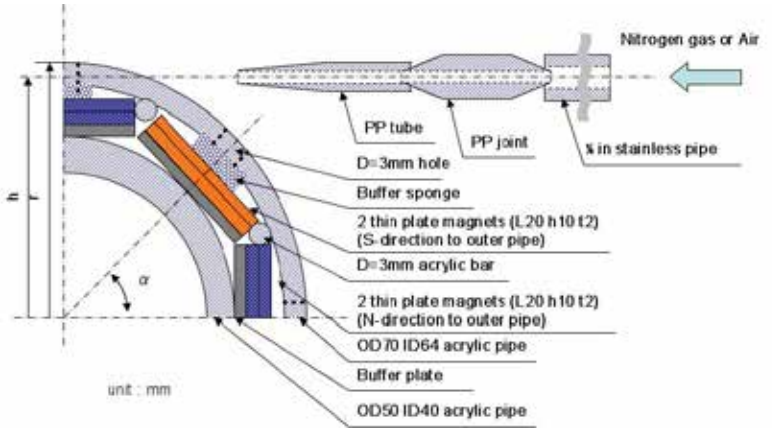

Fig. 9. Schematic drawing of the nozzle and the rotary mechanism part

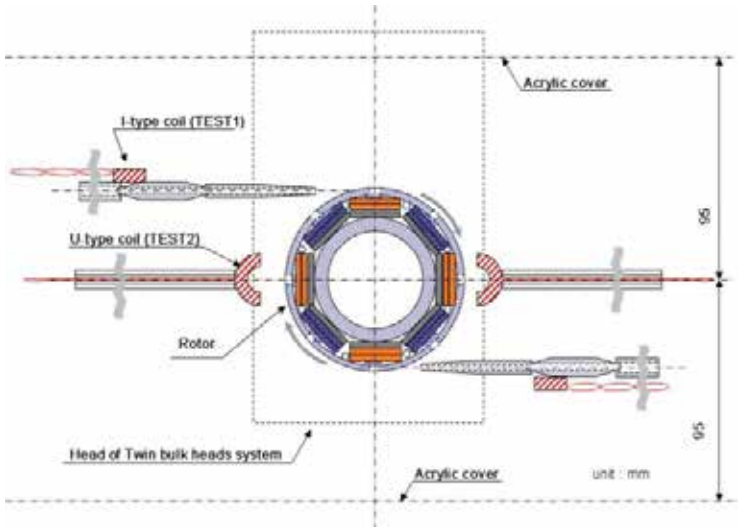

Fig. 10. Schematic drawing of the rotary mechanism part

3. Experiments and results

3.1 Original rotor model

Fig. 11. View of original rotary mechanism part

Figure 11 shows the broken original rotary mechanism part with 4 plate magnets (20mmx10mmxt2, 0.23T) were arranged in a felt disk in the central side of the cylinder to be alternate poles of the magnets for a rotary mechanism part of the rotor. This rotary mechanism part were broken at 7,770 rpm using nitrogen gas cylinder at 0.49MPa in the meter of the nitrogen gas cylinder. After acrylic boards (W300mm, L300mm) were prepared to protect or for above reason.

3.2 Improved rotor model

The rotary mechanism part was improved by acrylic ring with 8 holes (in figure 12 and 9). The both of the donut-shaped cross sections of the rotary mechanism part were needed the masking with a polyimide tape, because it was absolute terms for this rotor. The holes and sponge rubbers were also absolute terms. If the holes were changed to bucket shapes or the holes without sponge rubbers, the rotor was never rotate at 2,000 beyond. It is guessed that these holes with the sponge rubbers act as sink and source in fluid dynamics.

Fig. 12. View of the acrylic rotary mechanism part

In this examination, the acrylic cover was prepared. The box tunnel model acrylic cover (L300mm, W190mm, H82mm), was sat the between the heads of the bulk twined heads device. Inner surface of the acrylic cover top and bottom plane of the upper head of the bulk twined heads device is top of the cover off the board so that same plane. Also, inner surface of the acrylic cover bottom and top plane of the under head of the bulk twined heads device is top of the cover off the board so that same plane. This cover limited the control volume of the promote gas. The promote gas was nitrogen gas at 0.49MPa in meter of gas cylinder. The I-shaped coils were used. Purpose of this test was two. One was for confirmation of that the U-shaped coils were a little related to the rotation of the rotor. Other was for confirmation of flow around the rotor. The same examination was three times in a row. Figure 13-1 shows views of video records. The dot circle of Figure 13-1 (c) shows the hitting point of turn flow around the rotor to the inside wall (in figure 13-2). Figure 14-1 and 14-2 show the results which rotation speed and the voltage. An early stage of unstable state shown for figure 13-1 (b) suddenly stabilized it after having occurred from a rotation start from observation of a video from the back to 17 seconds for 10 seconds. The rotation fell slowly after having stopped the promote gas 10 minutes later and became an unstable state for 1010 seconds from 992 seconds. These examinations demonstrated that the U-shaped coils were a little related to the rotation of the rotor.

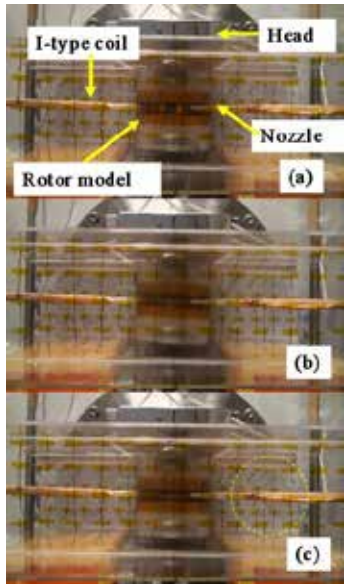

Fig. 13-1. View of test using tunnel cover, I-shaped coils and nitrogen gas

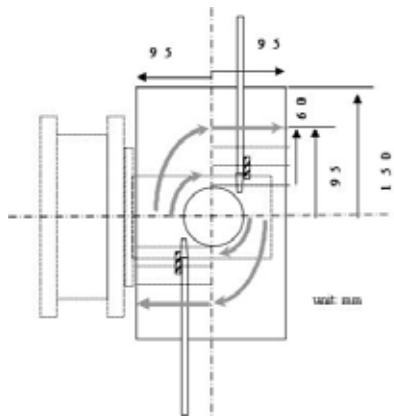

Fig. 13-2. Schematic drawing of the rotation of the test using tunnel cover, I-shaped coils and nitrogen

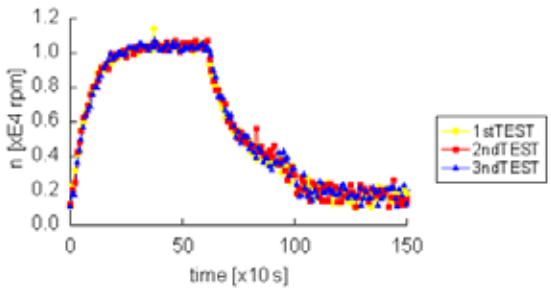

Fig. 14-1. Result of the rotation of the test using tunnel cover, I-shaped coils and nitrogen

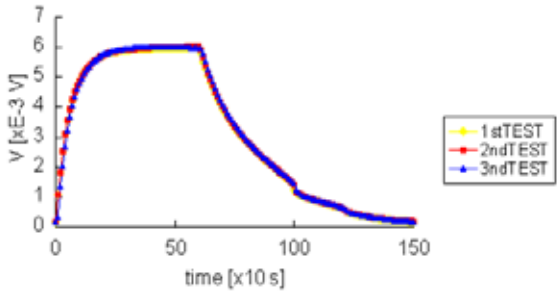

Fig. 14-2. Result of the volt of the test using tunnel cover, I-shaped coils and nitrogen

Though above the examinations show 10,000 rpm, the ability of the system as nitrogen gas cylinder was limited. At next step, an air compressor and acrylic boards of the walls without a box tunnel model acrylic cover were preparation. During the examinations the rotary mechanism part was destroyed it in 11,809 [rpm]. This result was show an ability of an increase in rotation speed under this condition.

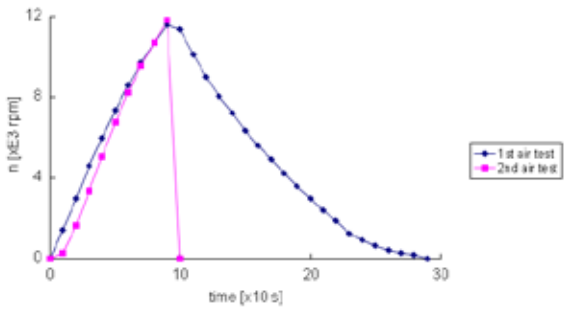

Fig. 15. Result of test of the acrylic rotary mechanism part

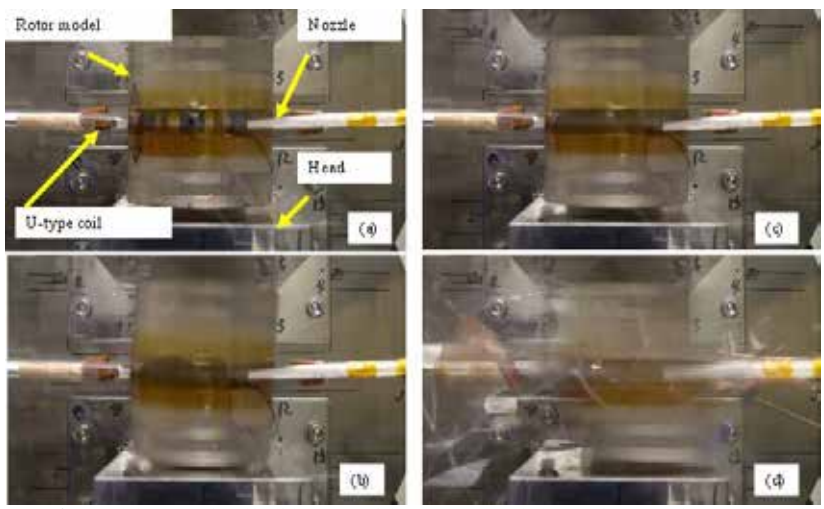

Fig. 16. View of test (a) Standstill, (b) Unstable rotation, (c) High speed rotation, (d) Broken

After the acrylic ring of the rotary mechanism part of the rotor, an aluminium ring with 8 holes was used (in figure 17). The both of the donut-shaped cross sections of the rotary mechanism part were needed the masking with a polyimide tape, because it was absolute terms. This improved rotor was used safety. In 2009, a gauss meter was join the measurement system and Hall generator was fixed to the top of the upper head of the bulk twined heads system with polyimide tape so that the centre position on the HTS bulk placed in the upper head. The promote gas was air using an air compressor at 0.2 MPa (free) in a meter of this device. The T-shaped coils were used.

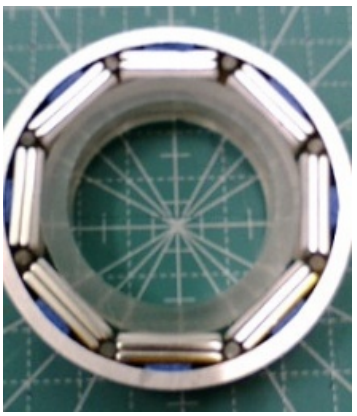

Fig. 17. View of the rotary mechanism part with an aluminium ring

The result of the examinations was show that the flux flows were increase along the increase of the rotation. The results in figure 18-1 through 18-4 were show that the same examinations were ten times continuously. The vertical lines, 80x10 seconds in x-axis in figure 18-1, are shown trigger marks of the rotor completely stopped.
The results in figure 19-1 through 19-4 were show the same result using timeline. Figure 19-5 was show the result of temperature of each thermocouples, p1 was room temperature, p4 was placed at upper face of the upper head, p7 was point above the upper face of the upper head, p3 and p5 were point of the centre between the head and the end of the stainless of the nozzle, p2 and p6 were point of the end of the stainless of the nozzle. All points were along a line of centre between the nozzles.
There were shown the good repeatability except the temperature data of the HTS bulk. The gradient of a data line of the magnetic flux density was raised slowly than a data line of the rotation. The data line of the temperature was different other graphs. In figure 19-3. The temperature peaks were shown at from 3rd to 6th examinations. Though the falling of a based line of the temperature of the HTS bulk was shown along the room temperature in figure 19-5, the characteristic of the up-and-down of a base line of the temperature of the HTS bulk was also related to the rotation because another result of the test was shown in figure 20.
It is assumed to risen the magnetic flux density so that following;
Based on a point of charge (point particle) be not able to stay on a gradient of the magnetic field by Earnshaw's theory, it is assumed that a moved magnetic flux was not able to stay on a gradient of the magnetic field, and the magnetic flux pinning were moved to centre of the HTS bulk by the centripetal force, and the magnetic flux were diffused according over time, and while the temperature of the HTS bulk was down.

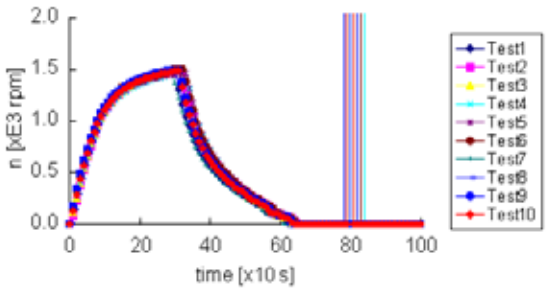

Fig. 18-1. Result of the rotation of the same tests

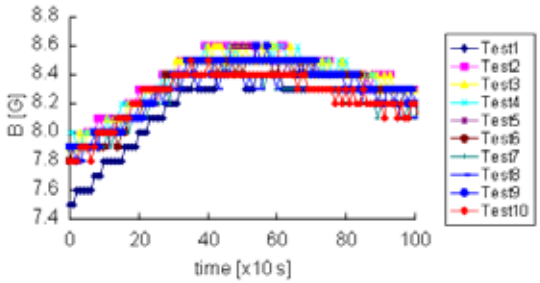

Fig. 18-2. Result of magnetic flux density of the same tests

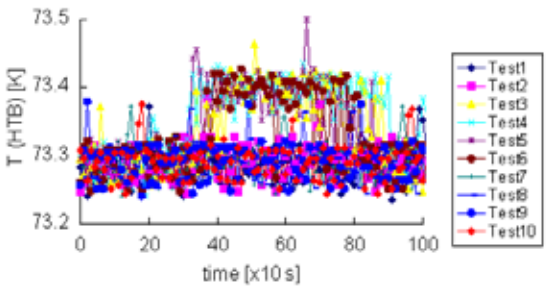

Fig. 18-3. Result of the temperature of the HTS bulk the same tests

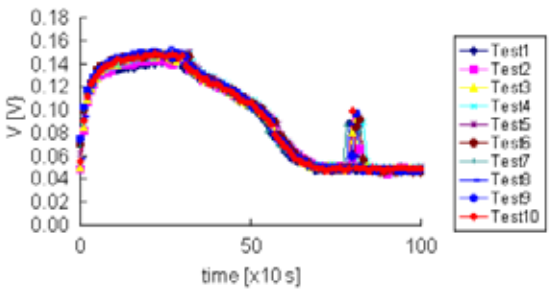

Fig. 18-4. Result of the voltage of the same tests

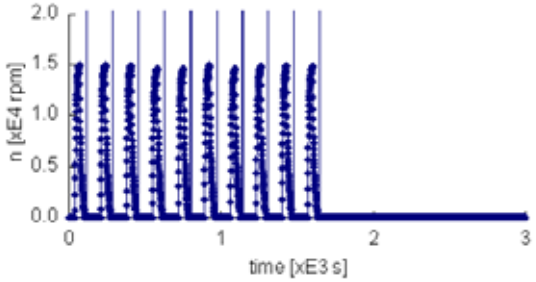

Fig. 19-1. Result using timeline of the rotation of the same tests

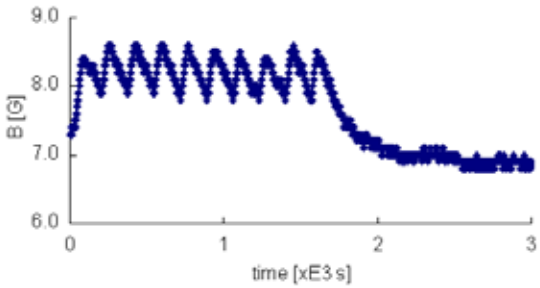

Fig. 19-2. Result using timeline of the magnetic flux density of the same tests

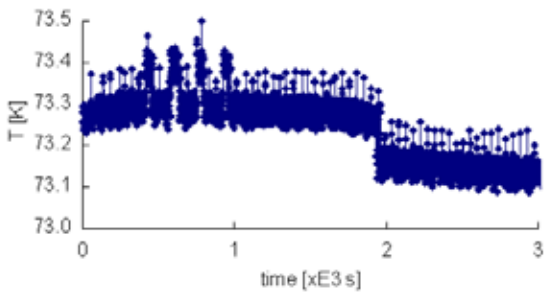

Fig. 19-3. Result using timeline of the temperature of the HTS bulk of the same tests

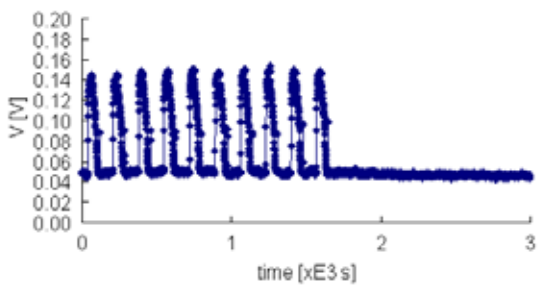

Fig. 19-4. Result using timeline of the voltage of the same tests

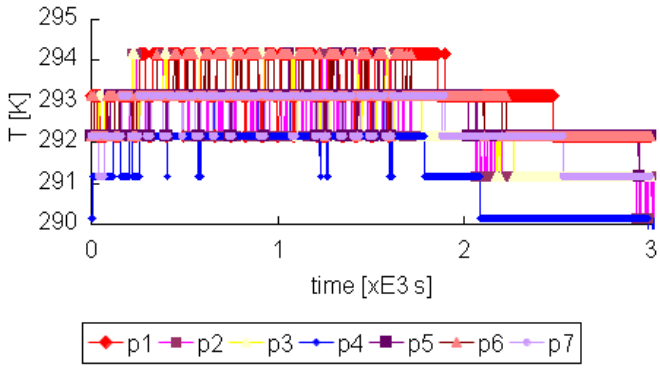

Fig. 19-5. Result using timeline of the temperature of each point around space of the system during the same tests

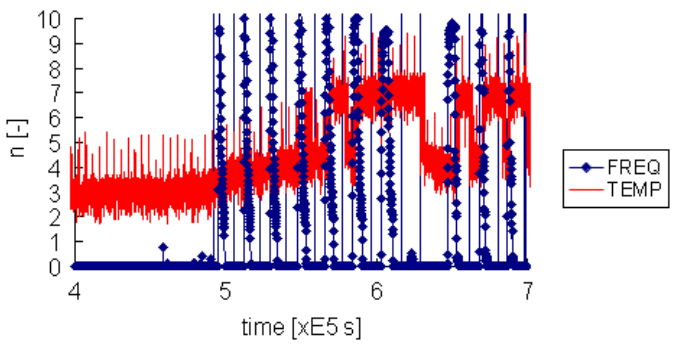

Fig. 20. Relationship between the magnetic flux density and the rotation at using timeline

In the experiment to proceed, the problem of the drag (coefficient) of the coils and nozzles was remained. There was tried the condition that differ distances between the rotor and T-shaped coils and/or the nozzles. The promote gas was air using the air compressor. The distances between the T-shaped coil and the rotor were three that near (no sign), 10mm (C10), and 15mm (C15) in figure 21. The distances between the nozzle and the rotor (see figure 9 and 10) were three that near (no sign), 15mm (N15), and 20mm (N20). The result of the test was shown in figure 21. The position of the nozzle was influenced by unstable rotation. The condition of this test was that the distance between the coil and the rotor was 10mm and the distance between the nozzle and the rotor was 15mm. In this condition, the differ pressures of the air compressor was tested (in figure 22). The condition that high pressure and long time, was not shown because the ability of the air compressor was small. The point of falling along the down slope in figure 22 was shown clearly unstable rotation. Table 1 was shown the rotation values at the point of its falling.

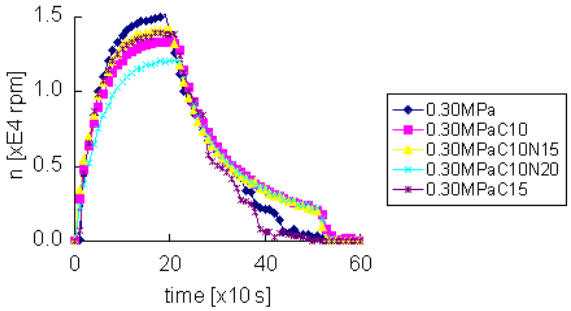

Fig. 21. Result of the rotation using the differ conditions

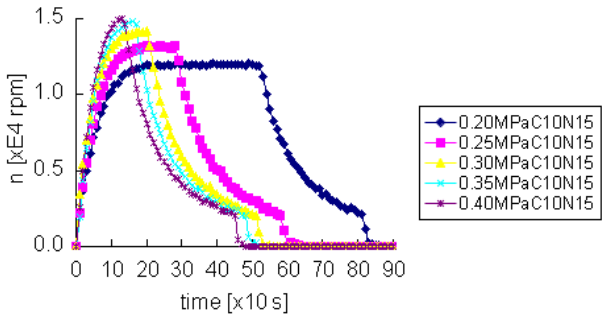

Fig. 22. Result of the rotation using the differ pressures

	0.20MPa C10N15	0.25MPa C10N15	0.30MPa C10N15	0.35MPa C10N15	0.40MPa C10N15
n [xE4 rpm]	0.2160	0.2056	0.2012	0.2027	0.2011

Table 1. The rotation values at each falling point under the differ pressures

Figure 23 was shown the data at 0.2MPa and 0.4MPa in figure 22.
The slope of the function curve line upside were legend symbol 'rev' as shown at figure 23.
In this my report, I assumed the following that;
1) The distance is the short distance in infinity in the x-axis direction as the rotation direction at around the rotor and the time is infinite.
2) The velocity of the rotor is constant while X as the external force is maxima at infinite time.
3) Though X is proportional to angular velocity, the value of X is constant.
4) The resistance of air is proportionate to the square of v.
5) Function of hyperbolic arctangent is 1 at finite time.
6) It is only problem as a contradiction between the infinite time and the finite time.
7) In this paper, it is may be no problem to formed the equation no using fluid dynamics, N-S equation, a complex velocity potential, and etc.
The equation of motion was shown to equation 1 through 3. The equation 5 is the result of that is introduced the idea of the equation (6) into the equation (4). The results of the equation were legend symbol 'cal' as shown at figure 23.

It is assumed that the true function curve line must be existed the surrounded area with a function curve line of the experiment data and a curve line of a slope of the same function curve line upside.
Therefore, it is guessed that the surrounded area with a true function curve line and a function curve line of the experiment data line shows the energy of the external force, and the surround area with a true function curve line and a curve line of the slope of the function curve line upside of the experiment data line shows the energy of the resistance of air for the rotor in this examination.

$$\frac{dv_x}{dt} = k'\mathrm{r}\omega^2 - kv_x^2 \tag{1}$$

$$\frac{dv_x}{dt} = \mathrm{X} - kv_x^2 \tag{2}$$

$$\frac{1}{v_x^2 - \frac{\mathrm{X}}{k}} dv_x = -kdt \tag{3}$$

$$\int_0^v \frac{1}{v_x^2 - \frac{\mathrm{X}}{k}} dv_x = \int_0^{\frac{1}{\mathrm{L}}} -kdt \tag{4}$$

$$v = \sqrt{\frac{\mathrm{X}}{k}} \tanh \sqrt{k\mathrm{X}} \frac{t}{\mathrm{L}} \tag{5}$$

$$\begin{pmatrix} 1 & 0 & 0 & 0 \\ 0 & 0 & 0 & 0 \\ 0 & 0 & 0 & 0 \\ 0 & 0 & 0 & \frac{1}{\mathrm{L}} \end{pmatrix} \begin{pmatrix} x \\ y \\ z \\ t \end{pmatrix} = \begin{pmatrix} x & 0 & 0 & \frac{t}{\mathrm{L}} \end{pmatrix} \tag{6}$$

	0.2[MPa]	0.4[MPa]
X [xE4 rpm]	1.2	2.2
k [-]	0.8	0.8
L [-]	100	100

Table 1. Each value in simulation

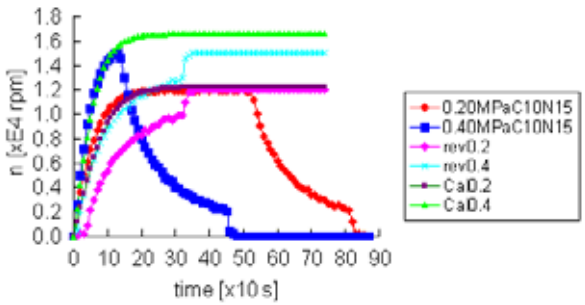

Fig. 21. Relationship between the results of the simulation and the real data

4. Conclusion

The above results of the examinations were shown the following;

1) These experimental results were demonstrated the high speed rotation.
2) It was clearly indicated the unstable rotation at 2,000 rpm.
3) The magnetic flux density was risen along that the rotation was raised. It was assumed that the magnetic fluxes were moved in direction to the centre of the HTS bulk.

5. References

H.Ozaku. (2008). A rotor model with two gradient static field shafts, *Physica C*, Vol.468, pp2125-2127

John R Hull. (2000). Superconducting bearings, *Supercond. Sci. Technol*, Vol.13, pp.1-5

Edited by Bostjan Polajzer

The term magnetic bearings refers to devices that provide stable suspension of a rotor. Because of the contact-less motion of the rotor, magnetic bearings offer many advantages for various applications. Commercial applications include compressors, centrifuges, high-speed turbines, energy-storage flywheels, high-precision machine tools, etc.

ISBN 978-953-51-5925-4

Photo by ishmeriev / iStock

IntechOpen